

Spatially-Resolved Proteomics of the Human Lens:  
Mapping Age- and Development-Related Lens Protein Modifications

By

Jamie Lyn Wenke

Dissertation

Submitted to the Faculty of the  
Graduate School of Vanderbilt University  
in partial fulfillment of the requirements

for the degree of

DOCTOR OF PHILOSOPHY

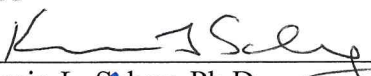
in

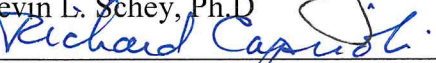
Biochemistry

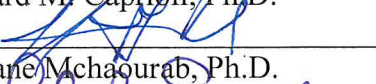
May, 2016

Nashville, Tennessee

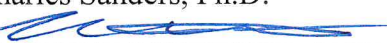
Approved:

  
\_\_\_\_\_  
Kevin L. Schey, Ph.D.

  
\_\_\_\_\_  
Richard M. Caprioli, Ph.D.

  
\_\_\_\_\_  
Hassane McHaourab, Ph.D.

  
\_\_\_\_\_  
Charles Sanders, Ph.D.

  
\_\_\_\_\_  
Rebecca Sappington, Ph.D.

Date:

1-7-16

1/7/16

~~1/7/16~~ 1-7-16

1/7/16

1/7/16

## DEDICATION

To my Grandpa John:  
thank you for inspiring me and believing in me

## ACKNOWLEDGMENTS

I am thankful for the support and guidance from a number of individuals throughout my graduate career. I am especially grateful for my mentor, Kevin Schey. As a calm and patient teacher, he encouraged curiosity and perseverance, allowing me to grow as a scientist. I am also thankful for helpful discussions and feedback from Hassane Mchaourab, Richard Caprioli, Rebecca Sappington, and Chuck Sanders.

I am forever grateful for the opportunity and support to travel to Auckland, NZ. While studying at the University of Auckland Molecular Vision Laboratory, I met incredible lens scientists and friends including Paul Donaldson, Angus Grey, Julie Lim, Ivy Li, Irene Vorontsova, and Mitch Nye-Wood.

I am grateful for the discussions, advice, and experimental help from everyone in the Vanderbilt MSRC. Zhen Wang and David Anderson helped me get started in the lab, providing instrumental training and scientific guidance. I am also thankful for help from Peggy Angel, Erin Seeley, Josh Nicklay, Kristie Rose, Salisha Hill, Hayes McDonald, Ying Qi, Jeff Spraggins, Boone Prentice, and Jeremy Norris.

This work would not have been possible without financial support from a variety of sources, including the Vanderbilt Vision Research Center, Vanderbilt Graduate School, Vanderbilt University Graduate Fellowship Award, Dissertation Enhancement Grant, National Eye Institute Training Grant, National Institute of Health, and the Vanderbilt University Department of Biochemistry.

I have met so many incredible friends who have positively shaped my experience at Vanderbilt. Thanks to Chad Chumbley, Romell Gletten, Amanda Hachey, Jessica Moore, Allison Prewitt, and David Rizzo for helpful discussions, chats, and coffee breaks.

I am thankful for support from my parents, my brother Pat and sister-in-law Sara, Grandpa John, and Grandma Mina. Thanks to my best friend, Elise Higgins, for always showing interest in my career, celebrating my accomplishments, and encouraging me along the way.

I would also like to thank my husband, Tim Bartlett, for his constant support and patience. He has enabled me to grow as a person and has loved me every step of the way. Thank you for reminding me to laugh, to remain in the present, to make lists when I am overwhelmed, and not to take myself too seriously.

## TABLE OF CONTENTS

	Page
DEDICATION .....	ii
ACKNOWLEDGMENTS .....	iii
LIST OF FIGURES .....	vi
TECHNICAL ABBREVIATIONS.....	ix
BIOLOGICAL ABBREVIATIONS .....	xi
Chapter	
<b>I. Introduction</b>	
Overview .....	1
Ocular Lens	
The Eye .....	2
Lens Development .....	4
Lens Structure and Organization .....	6
Lens Clarity and Function.....	10
Lens Circulation System .....	11
Lens Aging and Disease.....	13
Aquaporins in the Lens	
Aquaporin Family .....	14
History of AQP0 .....	15
Aquaporin Expression in the Lens .....	16
Aquaporin Function in the Lens .....	19
AQP0 Sequence and Modifications .....	21
AQP0 and Disease .....	25
Future Research .....	25
Spatially-Resolved Proteomics	
The Necessity for Spatial Information .....	26
Challenges to Membrane Protein Analysis.....	26
Proteomics.....	27
Cell or Tissue Homogenization .....	28
Laser Capture Microdissection .....	29
Microextraction and Hydrogels .....	30
MALDI Mass Spectrometry: Profiling and Imaging .....	32

Advantages of Mass Spectrometry-based Proteomics .....	36
Summary and Research Objectives .....	37
References .....	38
<b>II. MALDI Imaging Mass Spectrometry Spatially Maps Age-Related Deamidation and Truncation of Human Lens Aquaporin-0</b>	
Summary .....	48
Overview .....	49
Experimental Methods .....	51
Results .....	58
Discussion .....	83
Conclusions .....	87
References .....	88
<b>III. Spatially-Resolved Proteomics of the Human Lens Remodeling Zone</b>	
Summary .....	93
Overview .....	94
Experimental Methods .....	97
Results .....	104
Discussion .....	128
Conclusions .....	132
References .....	133
<b>IV. Conclusions and Perspectives</b>	
Contributions and Conclusions .....	136
Future Research .....	140
Perspectives .....	147
References .....	149
<b>Appendix A, ANOVA and Tukey Test Results .....</b>	<b>152</b>

## LIST OF FIGURES

### **Chapter I**

1.1. Diagram of a Human Eye .....	3
1.2. Lens Induction and Development .....	5
1.3. Diagram of the Lens Depicting an Axial Cross-Section.....	7
1.4. SEM of Ball-and-Sockets in Different Cortical Regions of Monkey Lens (20 year old) .....	9
1.5. The Lens Circulation System.....	12
1.6. Diagram of Aquaporin Expression in the Lens (Axial Cross-Section).....	18
1.7. Amino Acid Sequence and Post-Translational Modifications of Human AQP0.....	24
1.8. Tissue Microextraction Strategy for Identifying Localized Signals from MALDI IMS Experiments.....	31
1.9. Schematic of the MALDI IMS Process .....	35

### **Chapter II**

2.1. Representative MALDI-TOF Spectra from 2-Month and 21-Year Human Lens.....	60
2.2. AQP0 Protein Imaging Demonstrates Age-Related Truncation (Overlays).....	61
2.3. AQP0 Protein Umaging Demonstrates Age-Related Truncation .....	62
2.4. Fatty Acid Acylated AQP0 Protein Overlays .....	64
2.5. Fatty Acid Acylated AQP0 Protein.....	65
2.6. Tandem Mass Spectrum Confirming Lipid Modification of AQP0 in 4-Month Lens .....	66
2.7. Deamidation of C-terminal AQP0 Peptide 239-263 .....	68

2.8. Age-related Accumulation of Deamidation and Truncation (Overlay) .....	69
2.9. Age-related Accumulation of Deamidation and Truncation.....	70
2.10. Tandem Mass Spectrum Identifying AQP0 Deamidation Site at N246 .....	72
2.11. Chromatographic Traces for Original Elution Gradient (0.75 %B/min) for Triply-Charged AQP0 C-terminal Peptide 239-263 with 0, 1, and 2 Deamidation Events .....	75
2.12. Extended Gradient (0.3 %B/min) in AQP0 Peptide Elution Range Enables Baseline Separation of Differentially-Deamidated Species .....	76
2.13. Deamidation of AQP0 C-terminal Peptide Accumulates with Age.....	77
2.14. Reactions of the Labile Asn/Asp residues in Proteins from Aged Lenses .....	78
2.15. Multiply-Charged Intact AQP0 is Detected by MALDI FTICR MS Profiling using 2-NPG Matrix .....	80
2.16. <i>In situ</i> Digestion and MALDI IMS of Insoluble Lens Proteins from a 69-Year Human Lens .....	82

### **Chapter III**

3.1. Confocal Microscopy Image of 22-Year Human Lens.....	96
3.2. The Selected Reaction Monitoring Technique .....	102
3.3. Summary of Laser Capture Microdissection (LCM) and LC-MS/MS Analysis .....	107
3.4. List of Protein IDs from Shotgun Proteomics, by Region .....	108
3.5. Shotgun Proteomics Results from a 22-Year Human Lens .....	112
3.6. Precursor and Transition Masses Monitored for Endogenous and Heavy-Labeled Isotopes in MRM Runs.....	114

3.7. Transitions, or Peptide Fragmentation Patterns, Selected for Multiple Reaction Monitoring of a Filensin Tryptic Peptide ( <sub>77</sub> LGELAGPEDALAR <sub>89</sub> ) .....	115
3.8. Quantitative Proteomics of Selected Lens Proteins .....	117
3.9. Absolute Quantitation of Cytoskeletal Peptides .....	118
3.10. Lipid Imaging of 18-Year Human Lens at 15µm Spatial Resolution in Positive Ion Mode .....	122
3.11. Lipid Imaging of 18-Year Human Lens at 15µm Spatial Resolution in Negative Ion Mode .....	123
3.12. Confocal Microscopy of a Macaque Monkey Lens Labeled with WGA-TRITC (red) and DAPI (blue) .....	125
3.13. Brightfield Microscopy of a Tree Shrew Lens .....	126
3.14. Transmission Electron Microscopy (TEM) of a Macaque Monkey Lens .....	127

## TECHNICAL ABBREVIATIONS

2-MBT	2-mercaptobenzothiazole
ACN	acetonitrile
ACN	acetonitrile
ANOVA	analysis of variance
ar/R	(aromatic/arginine)
CHCA	$\alpha$ -Cyano-4-hydroxycinnamic acid
CID	collision-induced dissociation
ClAA	chloroacetamide
DAN	diaminonaphthalene
DTT	dithiothreitol
ESI	electrospray ionization
FDR	false discovery rate
FTICR	Fourier transform ion cyclotron resonance
GSH	glutathione
HPLC	high performance liquid chromatography
i.d.	inner diameter
ID	identification
IMS	imaging mass spectrometry
LC	liquid chromatography
LCM	laser capture microdissection
LC-MS/MS	liquid chromatography-tandem mass spectrometry
<i>m/z</i>	mass-to-charge value
MALDI	matrix-assisted laser desorption ionization

MIP	lens major intrinsic protein (aquaporin-0)
MRM	multiple reaction monitoring
MS	mass spectrometry
NaOH	sodium hydroxide
o.d.	outer diameter
OCT	optimum cutting temperature medium
PCO	posterior capsular opacification
Q	quadrupole
SA	sinapinic acid
SRM	selected reaction monitoring
TEM	transmission electron microscopy
TOF	time of flight
TRITC	tetramethylrhodamine
Uniprot AC	Uniprot accession number
WGA	wheat germ agglutinin

## BIOLOGICAL ABBREVIATIONS

AQP0	aquaporin-0
AQP	aquaporin
BASP1	brain acid soluble protein 1
DF	differentiating fiber cells
F	female
GRIN	gradient refractive index
IC	inner cortex
IFAPs	intermediate filament interacting proteins
M	male
MF	mature fiber cells
PTM	post-translational modification
RZ	remodeling zone
TRITC	tetramethylrhodamine
TZ	transition zone
WGA	wheat germ agglutinin

## **Chapter I – Introduction**

**Adapted with permission from** Schey KL, Wang Z, Wenke JL, Qi Y. Aquaporins in the eye: expression, function, and roles in ocular disease. *Biochim Biophys Acta* 2014;1840:1513-1523.<sup>1</sup>

### **Overview**

Part of the eye's window to the outside world, the transparent ocular lens focuses light onto the retina for clear vision. Unique structural and molecular features enable the lens to act as an optical element. Lens fiber cells make up the bulk of the lens, spanning from the anterior to posterior surface.

New lens fiber cells are continuously laid down in concentric rings atop older fiber cells in the lens core. At the cellular level, organized fiber cell packing and lack of light-scattering organelles help establish lens transparency. Within the cell, regulation of water and protein concentration ensures a high refractive index and a fluid lens that can accommodate to different focal lengths. The unique organization of the lens – with older cells in the core and younger cells on the outside – facilitates spatial characterization of both old and new protein molecules within the lens, making it an excellent model for studying protein aging.

Although the lens is quite resilient at maintaining clarity, age-related changes to the lens and the decades-old proteins within can result in presbyopia (loss of near vision due, in part, to hardening of the lens) or cataract. Age-related cataract is the leading cause of blindness worldwide, affecting approximately 50% of individuals over the age of 70.<sup>2</sup> Although surgery can reverse cataract, it remains a substantial burden to the US healthcare system, accounting for 60% of vision-related Medicare costs.<sup>3</sup> Cataract surgery is expensive and can result in post-operative posterior capsule opacification (PCO), a secondary complication and additional expense.<sup>2</sup> It is estimated that delaying cataract onset by just 10 years would cut the number of

required cataract surgeries in half.<sup>4</sup> Characterizing lens protein changes over time contributes to our understanding of normal lens physiology and provides a context in which to study lens disease. The implementation of analytical tools like microscopy and mass spectrometry is critical for spatial characterization of important lens molecules that become modified with age. The lab's overall goal is to elucidate the temporal and spatial occurrence, as well as functional consequences, of lens membrane protein modifications during lens fiber cell differentiation and aging.

## The Ocular Lens

### *The Eye*

The eye facilitates vision by transmitting light from the outside world to the retina, which converts electromagnetic waves to signals that can be interpreted by our brains. Humans and other vertebrates have a camera-type eye, as depicted in Figure 1.1.<sup>5</sup> For proper vision, the pathway for light must be transparent and light must be focused onto the retina. Light passes through the visual axis, first encountering the cornea, followed by the lens and gel-like vitreous humor. Both the cornea and lens focus light before it reaches the retina at the back of the eye. Here, photosensitive pigments participate in a signal transduction pathway. In humans, 11-*cis* retinaldehyde is isomerized to the all-*trans* form upon photon absorption.<sup>6</sup> This conversion activates opsin, starting a cascade that allows signals to be transmitted through the optic nerve to the brain. The result is a picture of the world around us: objects with distinguishable shape, color, location, and motion.

**Figure 1.1**

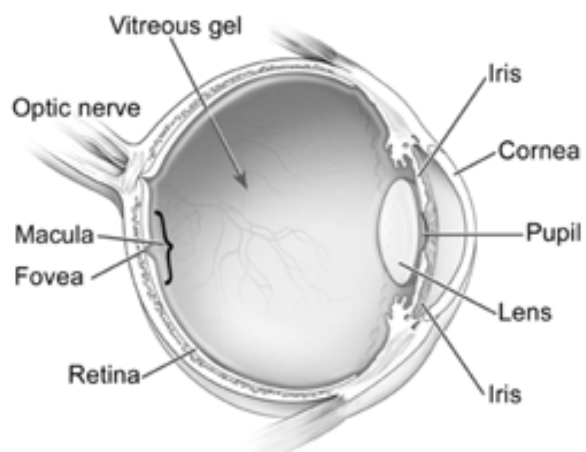


**Figure 1.1.** Diagram of a Human Eye.

Light passes through the cornea, pupil, and lens before focusing onto the retina.

*Diagram from* National Eye institute website, [www.nei.nih.gov/health/cataract/cataract\\_facts](http://www.nei.nih.gov/health/cataract/cataract_facts).<sup>2</sup>

## *Lens Development*

A critical part of the eye is the lens, which acts as an optical element to correct for spherical aberrations of the cornea and changes shape to focus on objects near and far. In vertebrates, the crystalline lens develops from the surface ectoderm during embryogenesis.<sup>7</sup> Like many other organs, the lens begins as a nonspecific layer of epithelial cells and develops into a specialized tissue composed almost entirely of lens fiber cells. During embryogenesis, the optic vesicle signals to the nearby surface ectoderm. The surface ectoderm thickens and changes shape to form the lens placode (Figure 1.2). The placode then invaginates into a pit, which pinches off to become the lens vesicle. At this point, the hollow lens vesicle is composed entirely of epithelial cells. Fibrogenesis, the process of epithelial cell differentiation into lens fiber cells, begins in the embryo and continues throughout life. Primary fibrogenesis occurs in the embryo when posterior epithelial cells elongate and lose their organelles to form the primary lens fiber cells. These primary fibers are compacted into the center of the lens as secondary fiber cells form. Secondary fibrogenesis occurs when anterior epithelial cells migrate to the lens equator and differentiate into fiber cells. Secondary differentiation happens continually throughout life, although the rate of differentiation slows with age. Thus, the oldest fiber cells are localized in the lens center, and newer fiber cells are localized throughout the lens cortex.

**Figure 1.2.**

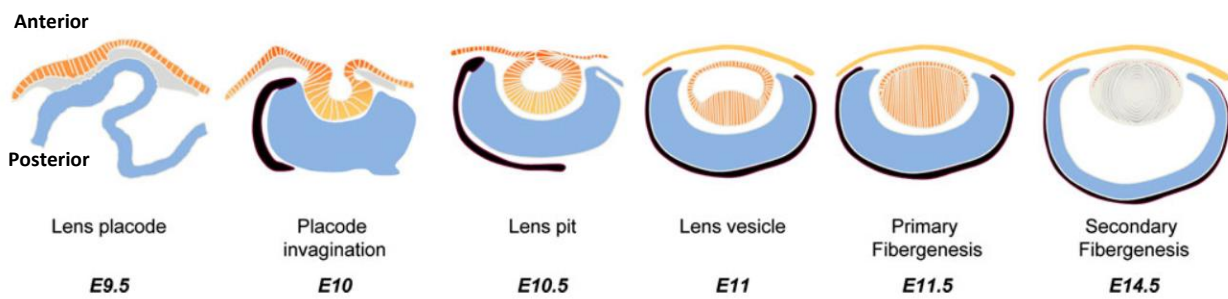


**Figure 1.2.** Lens Induction and Development.

The surface ectoderm thickens to become the lens placode, followed by invagination and pinching off to form the lens vesicle. Contact with the optic vesicle, which signals lens induction, is critical for this process. Primary fibrogenesis occurs during embryogenesis; these fibers are compacted in the center of the lens as secondary fiber cells are produced in the embryo and throughout the lifetime. Embryonic days shown correspond to mouse development; developmental timepoints vary for different vertebrate species.

*Adapted with permission from* Charlton-Perkins M, Brown NL, Cook TA. The lens in focus: a comparison of lens development in Drosophila and vertebrates. *Mol Genet Genomics* 2011;286:189-213.<sup>8</sup>

### *Lens Structure and Organization*

The mature lens contains two distinct cell types – a monolayer of epithelial cells on the anterior surface, and elongated, organelle-free fiber cells that comprise the bulk of the lens (Figure 1.3).<sup>9, 10</sup> Lens growth continues throughout the lifetime of an organism, with new fiber cells being continually added to the cortex of the lens atop existing cells in the lens core. Fiber cells elongate extensively as they differentiate, spanning from the anterior to the posterior of the lens. The tips of fiber cells join together at the anterior and posterior poles, forming Y-shaped and eventually more complex suture patterns where they interlock.<sup>11</sup> These long, hexagonal fiber cells are tightly packed in the lens outer cortex to minimize extracellular space that would cause light scattering. In human lens, ordered packing is interrupted by the remodeling zone, a region of extreme morphological changes characterized by immunofluorescence microscopy and transmission electron microscopy (TEM).<sup>12, 13</sup> Here, approximately 100µm beneath the lens capsule, smooth plasma membranes give way to blebbing membrane protrusions. TEM studies indicate ball-and-socket joints, connections between neighboring fiber cells, originate in the remodeling zone.<sup>13</sup> Beyond this region, cells maintain interdigitations and re-establish radial columns as they become compressed. Hexagonal fiber cells in the inner cortex gradually become more circular in the adult and fetal nucleus. Molecular events that cause morphological remodeling are unknown and are the focus of the work described in Chapter 3.

**Figure 1.3.**

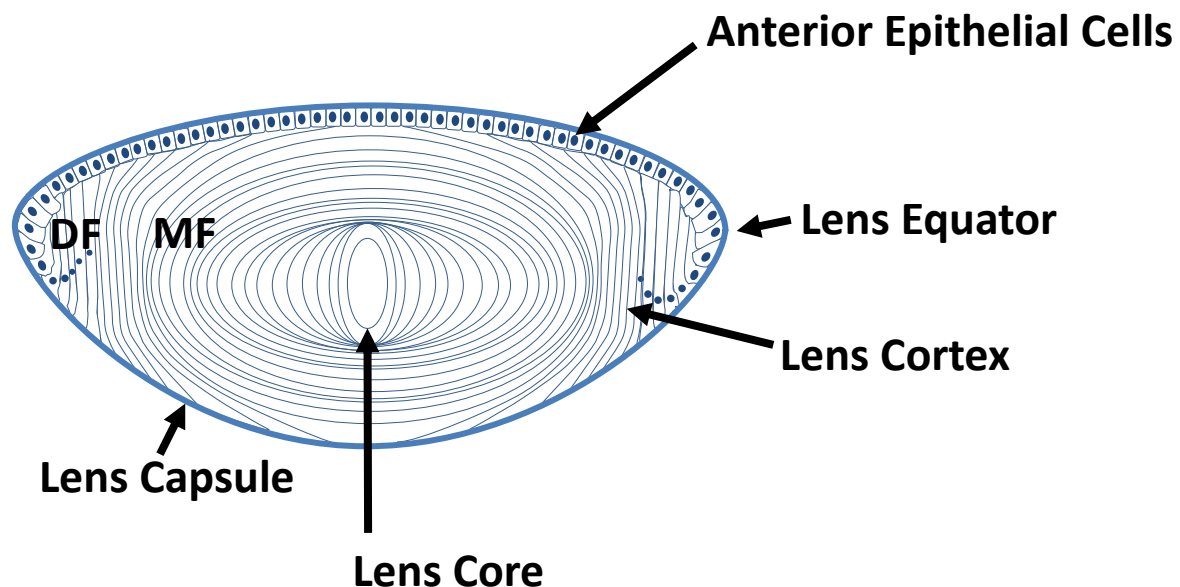


**Figure 1.3.** Diagram of the Lens Depicting an Axial Cross-Section.

Anterior epithelial cells migrate to the lens equator and begin differentiation. This process involves extensive elongation, cellular packing, and removal of light-scattering organelles including nuclei. Differentiating fiber cells (DF) in the outer cortex complete differentiation and become mature fiber cells (MF), adding to existing fiber cells in the inner cortex and nucleus. Cells in the lens core were formed during embryonic development and are as old as the individual.

Lens fiber cell organization and packing are critical for lens transparency and function. Maintaining extracellular space smaller than the wavelength of light reduces light scattering, which would hamper the ability of the lens to focus light onto the retina. Interdigitations including ball-and-socket joints and longer protrusions between neighboring cells (Figure 1.4)<sup>14</sup> enable communication and likely help the lens fiber cells maintain connections despite extreme deformations that occur during accommodation.<sup>11</sup> Furthermore, these connections ensure a uniform refractive index between cells to minimize light scattering.<sup>11</sup> Mutations in a wide variety of membrane and cytoskeletal proteins, including AQP0, filensin, phakinin, disrupt fiber cell packing which can lead to spherical aberrations, light scattering, and cataract.<sup>15-17</sup> In an AQP0 knockout animal, cellular protrusions formed normally but eventually underwent uncontrolled elongation, leading to fiber cell instability and cataract.<sup>18</sup> In another study, AQP0 knockout resulted in a lack of protrusions.<sup>19</sup> Despite this discrepancy in these results, the importance of AQP0 for controlled regulation of interdigitations cannot be disputed. Knockouts of filensin and phakinin, proteins that heterodimerize to form the lens-specific intermediate filament (beaded filament), also exhibit light scattering and structural abnormalities.<sup>20-23</sup> These data suggest beaded filaments are critical for long-term maintenance of cellular order after interdigitations are formed. These studies highlight the importance of lens structure and organization at both the tissue and cellular level.

**Figure 1.4**

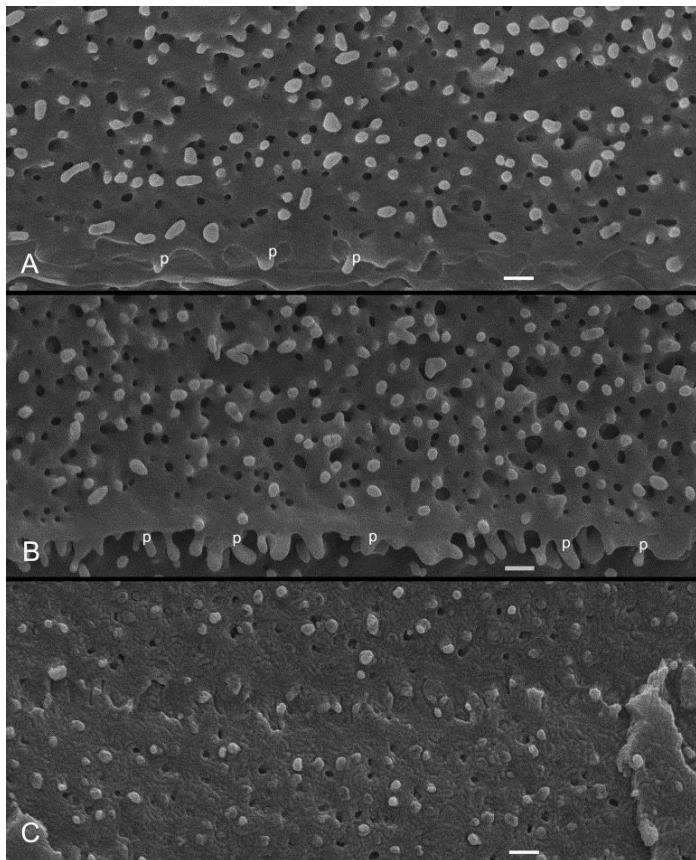


**Figure 1.4.** SEM of Ball-and-Sockets in Different Cortical Regions of Monkey Lens (20 year old).

**A:** Superficial cortical fibers (approximately 100  $\mu\text{m}$  from the surface), numerous ball-and-sockets are distributed on the long side of fiber cells. **B:** Intermediate cortical fibers (approximately 300  $\mu\text{m}$  from the surface), a large number of ball-and-sockets are found on the long side of fiber cells. In this region, many protrusions (p) are also distributed along the corners of cortical fiber cells. **C:** However, in the deeper cortex (approximately 500  $\mu\text{m}$  from the surface), ball-and-sockets display smaller number and size with degenerating appearance. The scale bars indicate 1  $\mu\text{m}$ .

**Reprinted with permission from** Biswas SK, Lee JE, Brako L, Jiang JX, Lo WK. Gap junctions are selectively associated with interlocking ball-and-sockets but not protrusions in the lens. 2010;16:2328-2341.<sup>14</sup>

### *Lens Clarity and Function*

A number of unique structural and molecular features enable lens clarity. Lens fibers are packed tightly to minimize extracellular space and therefore light scattering. Furthermore, a consistent refractive index is critical for lens clarity and focusing power.<sup>11</sup> Refractive index is a measure of how light is bent when traveling from one particular medium to another. The high refractive index of the lens, established in part by high concentrations of crystallin proteins, enables this biological focusing element to correct for spherical aberrations. Despite the high concentration of crystallin proteins (~450 mg/ml), which would typically cause tissue opacity, short-range-order arrangement of these proteins enables a high refractive index and therefore lens transparency.

A mismatch of refractive index can cause light scattering and loss of transparency.<sup>11</sup> Within the cell, organelles can become an issue because they typically have a higher refractive index than cellular cytoplasm.<sup>10</sup> Therefore, boundaries within cells (i.e. interfaces between the cytoplasm and plasma membranes or organelles) have the potential for disparate refractive indices. To overcome this problem, nuclei and other organelles are degraded during lens fiber cell differentiation to minimize light scattering. Mature fiber cells in the lens core are devoid of organelles, containing high concentrations of proteins enclosed by the plasma membrane.

The lens also contains a gradient of refractive index (GRIN). The lens refractive index increases from approximately 1.380 in the cortex to 1.409 in the core,<sup>24</sup> correcting for spherical aberrations. This also enables consistent refractive index between membranes and cytoplasm in the lens core. GRIN is established by a higher protein-to-water ratio in the core, which requires careful regulation of water flow through the lens. Binding of crystallin proteins to the plasma membranes may also minimize refractive index differences.<sup>25</sup>

### *Lens Circulation System*

The ocular lens is avascular and must rely on an alternative system for molecular transport and waste removal. Based on the volume of the lens, delivery of molecules to the center of the lens is diffusion-limited. Therefore, it has been hypothesized that the lens contains a microcirculation system to deliver nutrients and remove waste from the tissue. This has been reviewed extensively by Mathias *et al.*<sup>26</sup> who proposed an ion-driven current that drives fluid intake at the anterior and posterior pole and fluid exit at either lens equator. Increasing evidence using Ussing chambers support this model, confirming the directionality of water flow and even the connection to  $\text{Na}^+$  pumps, as inhibition of these pumps reduces fluid flux.<sup>27</sup> The generally accepted model shows  $\text{Na}^+$  ions entering at the lens anterior and posterior pole, traveling to the lens core through extracellular space, and exiting the lens at the equator intracellularly via gap junctions (Figure 1.5).<sup>28</sup> These circulating ionic currents also drive fluid flow through the lens in the same pattern. Water flow necessitates aquaporin water channels (AQP1 in epithelial cells and AQP0 in lens fiber cells) due to low water permeability of the plasma membrane. Recent studies using connexin knockout mice also indicate gap junctions, and specifically connexin-46, are important for the antioxidant glutathione (GSH) transport from the lens cortex to core.<sup>29</sup> The lens circulation system is undoubtedly important for maintaining lens volume and refractive index gradient during accommodation, as well as overall lens health by delivery of nutrients and removal of waste products from the long-lived lens. A potential issue is the reported barrier to water movement that occurs in human lens around age 50.<sup>30, 31</sup> This middle-age phenomenon restricts entry of water and glutathione to the lens core, which could also affect cataract development. The barrier could also be affected by increased crystallin protein association with the plasma membrane in aged lens.<sup>32</sup>

**Figure 1.5.**

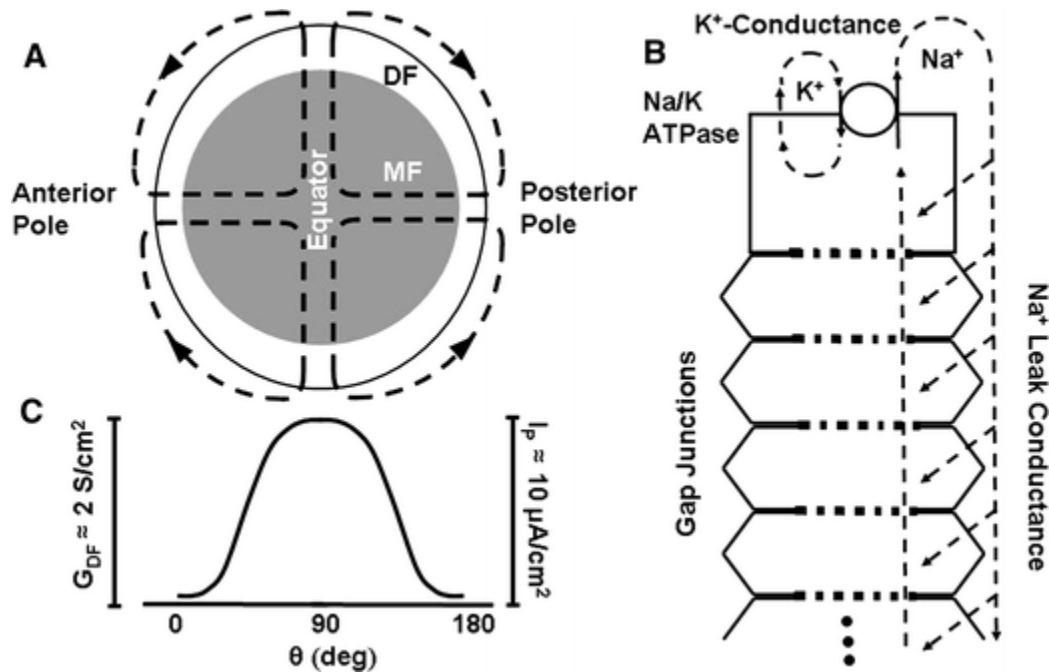


**Figure 1.5.** The Lens Circulation System.

(a) Pattern of current flow. Current enters the lens at both poles and exits at the equator. (b) Factors responsible for generating current flow. The transmembrane sodium gradient, which is generated by the Na/K pumps, pulls sodium across fiber cell membranes from the extracellular to the intracellular space. Thus, inward radial current is extracellular, whereas outward radial current is intracellular. (c) Factors responsible for directing the pattern of current flow. DF gap junctional coupling conductance,  $G_{DF}$  ( $S/cm^2$ ), is highest at the equator and directs the outward radial intracellular current to the equatorial surface. Na/K pump current density,  $I_p$  ( $\mu A/cm^2$ ), is highest at the equatorial surface, where the pumps are concentrated to transport the circulating flux of sodium out of the lens

**Reprinted with permission from** Mathias RT, Kistler J, Donaldson P. The lens circulation. *J Membr Biol* 2007;216:1-16.<sup>28</sup>

### *Lens Aging and Disease*

By design, mature fiber cells do not contain the machinery for cellular turnover or protein synthesis.<sup>9</sup> Consequently, these long-lived cells and their contents survive for decades in the lens. With time, molecular changes can contribute to age-related nuclear cataract, the single largest cause of blindness worldwide.<sup>2</sup> Cataract begins with some lens opacification and discoloration, typically yellowing, that reduces vision and eventually leads to blindness if untreated. The extent of discoloration is used to assess cataract severity using the Pirie classification system, and a dark brown lens core represents the most severe type of age-related cataract.<sup>33</sup> Cataract can be treated by surgical removal of the opaque lens and replacement with an artificial lens; however, this is an expensive procedure and can result in secondary complications like posterior lens opacification. Furthermore, cataract removal is difficult in developing countries and areas with inadequate healthcare access. The burden to the US Medicare system is staggering at over \$3 billion per year.<sup>34</sup>

As the name implies, aging is a major risk factor for age-related nuclear cataract. It is generally accepted that smoking, diabetes, and UV damage can hasten cataract development, likely due to oxidative damage. Importantly, time-dependent changes in protein and antioxidant composition have been identified in cataract but not control lenses. Both  $\gamma$ S- and  $\alpha$ A-crystallin post-translational modifications (PTMs) (deamidation, racemization, and isomerization) were increased in cataract lenses.<sup>35, 36</sup> These modifications could affect  $\alpha$ A-crystallin chaperone activity or induce aggregation. Glutathione (GSH) concentration in age-related nuclear cataract lens cores is also reduced,<sup>30, 33</sup> highlighting the importance of nutrient and antioxidant delivery for proper lens health. These data highlight the importance of understanding molecular changes, including protein PTMs, in the aging lens.

Several other types of cataract can also affect vision. Inherited congenital cataracts are typically caused by mutations to critical lens proteins including crystallins, AQP0, and beaded filaments filensin and phakinin.<sup>15, 17, 37</sup> These typically affect younger individuals and require early intervention to reverse blindness. Cataracts caused by eye trauma have also been noted. Posterior capsular opacification (PCO) is a common complication of cataract surgery and requires additional laser treatment to be reversed.<sup>2</sup>

Other physical changes to lens can also affect vision. Presbyopia, the hardening of the lens around age 50, affects lens elasticity and negatively impacts lens accommodation. This causes farsightedness (blurry vision when viewing close objects), requiring individuals to wear reading glasses. Furthermore, a barrier to diffusion has been noted around age 50.<sup>30, 31</sup>

Despite decades of research, there remain unanswered questions about the major causes, risk factors, and molecular changes associated with age-related nuclear cataract.

## Aquaporins in the Lens

### *Aquaporin Family*

The aquaporin family consists of water- and some water/glycerol-specific transporters. The first member, initially called CHIP28, was found in red blood cells and renal tubules.<sup>38, 39</sup> This channel-forming membrane protein was found to increase water transport when reconstituted in proteoliposomes or when injected into oocytes.<sup>40, 41</sup> The discovery of CHIP28, later named AQP1, earned Dr. Peter Agre the Nobel Prize in Chemistry in 2003.

Members 0-12 of the aquaporin family share structural and sequence similarities in addition to their function as water pores. Structurally, aquaporins contain 6 transmembrane domains consisting of two tandem repeats.<sup>42</sup> The two conserved NPA motifs are critical for

preventing proton movement through the water channel, while the ar/R (aromatic/arginine) motif facilitates water transport and restricts the pore size.<sup>43</sup> Structural studies indicate water molecules fit inside the channel in a single-file line. Variation in amino acid sequence leads to differences in water permeability and mercury sensitivity between the AQP family members.

### *History of AQP0*

Lens major intrinsic protein (MIP), so-called because of its high abundance in the ocular lens plasma membrane, was initially characterized as an intense ~26-27.5 kDa band by SDS-PAGE.<sup>44, 45</sup> Plasma membranes were isolated by urea treatment or density gradient centrifugation. Water-insoluble and urea-insoluble fractions contained an abundant protein comprising approximately 50% of the bovine and rabbit lens membrane fraction.<sup>44, 45</sup> MIP, now called AQP0, was initially hypothesized to be a constituent of gap junctions because of its junctional localization.<sup>46, 47</sup> However, additional studies suggested a widespread distribution throughout the plasma membrane.<sup>48</sup> Efforts to isolate and characterize AQP0 revealed its function as a pore to shuttle water across the plasma membrane.<sup>49, 50</sup> Initial predictions of AQP0 structure were based on the amino acid sequence deduced from cDNA cloning.<sup>51</sup> These studies suggested AQP0 contains six transmembrane domains with both the N- and C-terminus localized on the cytoplasmic side of the cell.<sup>51</sup> The structure of AQP0 has since been determined, now down to a resolution of 2.2 Å.<sup>52, 53</sup> Individual AQP0 monomers, each consisting of six transmembrane helices and a central water pore, form tetramers in the plasma membrane.<sup>52</sup>

### *Aquaporin Expression in the Lens*

As epithelial cells migrate to the lens equator and differentiate to fiber cells, there are significant changes in aquaporin expression (Figure 1.6). Lens epithelial cells contain AQP1.<sup>54</sup> Recent immunohistochemistry studies also demonstrated AQP5 and AQP7 labeling in the lens epithelium; however, their relative abundance has not been measured.<sup>55-57</sup> In lens fiber cells, AQP0 is highly abundant comprising over 50% of lens membrane protein concentration. AQP5 is also found at lower levels in fiber cells, estimated to be ~5% of lens AQP0 levels.<sup>10, 55, 56, 58, 59</sup> AQP1 is present in apical and basolateral membranes of lens epithelial cells.<sup>60</sup> As epithelial cells migrate toward the lens equator and begin to differentiate, AQP1 expression decreases and is gradually replaced by AQP0. In rat lenses, immunofluorescence indicates that AQP0 localization changes with distance from the lens capsule.<sup>61</sup> In the outer cortex, AQP0 is distributed between broad and narrow sides of the hexagonally-shaped lens fiber cells. Deeper into the cortex, AQP0 predominantly forms plaque-like structures on the broad sides of fiber cells, which is consistent with ribbon-like and tongue-and-groove type structures found in freeze-fracture studies.<sup>62, 63</sup> In the inner cortex, AQP0 is again redistributed throughout the plasma membrane.<sup>61</sup> AQP0 in the lens core is present in 11–13 nm thin junctions, supporting its role as a structural molecule.<sup>64</sup> Evidence for microdomains, including mixed junctions composed of AQP0 and connexins, indicates AQP0 localization within the plasma membrane may affect its function.<sup>62</sup> These changes in AQP0 localization may be critical for modulating protein function in mature lens fiber cells from a water pore to a junctional protein. Proteomics, immunofluorescence, and transcriptomics studies suggest that AQP5 is present in much lower abundance than AQP0<sup>55, 56, 59</sup> and that it traffics from the cytosol to the membrane during fiber cell differentiation.<sup>56</sup> More recent evidence indicates age-related and differentiation-dependent localization based on mouse

lens age.<sup>65</sup> AQP0 is membranous throughout the lens, whereas AQP5 appears to be in cytoplasmic vesicles until around the time of AQP0 cleavage.<sup>65</sup> Currently, the role of AQP5 trafficking to the membrane is not well understood, although it is hypothesized to assist in water transport in the lens core.<sup>56</sup>

**Figure 1.6.**

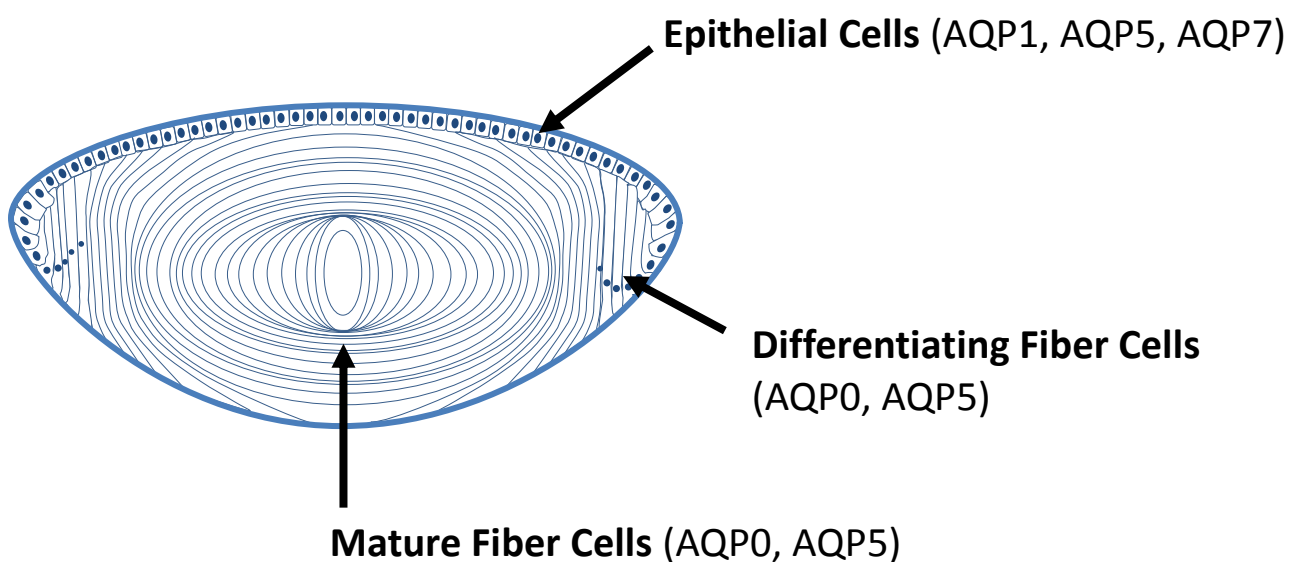


**Figure 1.6.** Diagram of Aquaporin Expression in the Lens (Axial Cross-Section).

**Reprinted with permission from** Schey KL, Wang Z, Wenke JL, Qi Y. Aquaporins in the eye: expression, function, and roles in ocular disease. *Biochim Biophys Acta* 2014;1840:1513-1523.

### *Aquaporin Function in the Lens*

The lens, as its name implies, functions as a key focusing element in the ocular optical system. In order to function as a focusing element, the lens has developed a mechanism to reduce spherical aberrations and to remain transparent. Spherical aberrations are reduced by establishing a gradient of refractive index (GRIN). This gradient is formed by differential protein expression and concentrations across fiber cells; a concentration gradient that must be exquisitely maintained via fluid balance.<sup>66</sup> Furthermore, lens volume changes during accommodation are accompanied by rapid water movements presumably through AQP channels.<sup>67</sup> Lastly, a microcirculation system has been proposed to explain how transparency of this avascular tissue is maintained over decades of life.<sup>26</sup> Localization of ion channels, gap junctions, and aquaporins is important in establishing the water flux necessary for the circulation system.<sup>26</sup> Clearly, any disturbance in water transport properties could have significant deleterious effects on transparency and optical properties of the lens.

Studies in AQP1 null mice demonstrated the importance of AQP1 for water transport in lens epithelial cells.<sup>60</sup> These AQP1-deficient lenses had normal morphology but lower epithelial permeability to water, as demonstrated by higher basal water content, less response after incubation in hypotonic solutions, and slower equilibration in cell swelling assays. To date, no functional studies have characterized the role of AQP7 in the lens epithelium, although it could allow for transport of small molecules.<sup>57</sup>

The shift from AQP1 expression in lens epithelial cells to expression of AQP0 in lens fiber cells may seem odd due to low mammalian AQP0 permeability<sup>68</sup> (note that killifish AQP0 has high permeability, similar to AQP1<sup>69, 70</sup>); however, there are several reasons AQP0 may uniquely serve lens biology. First, its extremely high density in lens fiber cells could compensate

for its relatively low permeability. It is noteworthy that the estimated sum of the AQP0 permeability in lens fiber cells is equivalent to that of AQP1 permeability in epithelial cells.<sup>49, 71</sup> This may be required to maintain water balance between the bulk of the lens and the highly permeable epithelial layer. Furthermore, AQP0 also functions as an adhesional protein. AQP0 knockout mice develop cataracts, and transgenic expression of AQP1 in AQP0 knockout mice does not restore lens transparency.<sup>72</sup> *In vitro* studies showed increased cell-to-cell adhesion in cells expressing AQP0 but not AQP1. These studies highlight the unique properties of AQP0 and emphasize the critical role of AQP0 for lens transparency.

AQP0 permeability can be regulated under certain conditions, potentially modulating water flow when necessary. Two studies demonstrated that AQP0, but not AQP1, permeability is sensitive to pH and Ca<sup>2+</sup> levels.<sup>73, 74</sup> AQP0 can also be modulated by protein–protein interactions. Calcium affects calmodulin binding to the AQP0 C-terminus resulting in decreased water permeability.<sup>75, 76</sup> Phosphorylation of serine-235 in AQP0 reduces calmodulin binding and consequently increases the permeability of the channel.<sup>77, 78</sup> Phosphorylation at serine-235 has also been shown to be important for trafficking of AQP0 to the plasma membrane.<sup>79</sup>

AQP0 may also serve as a structural molecule. The interaction of AQP0 with ezrin/radixin/moesin actin binding proteins,<sup>80</sup> with lens specific cytoskeletal proteins filensin and phakinin,<sup>77, 81, 82</sup> and with gap junction proteins<sup>83, 84</sup> may be important for its structural properties. AQP0 has been implicated in junction formation, tongue-and-groove formation, and cell-to-cell adhesion in a number of studies.<sup>63, 85-87</sup>

AQP0 is extensively truncated in older fiber cells, which was hypothesized to shift the protein from water pore to junctional form.<sup>53, 64</sup> However, recent studies indicate both full-length and truncated forms of AQP0 are open water channels and capable of facilitating cell-to-cell

adhesion.<sup>87, 88</sup> Animal models of cataract have identified numerous residues important for AQP0 trafficking and function, and have helped to characterize the unique role of AQP0 in the lens.<sup>72, 89, 90</sup> For example, AQP0 null mice have cataracts, disorganized cellular packing and altered optical properties.<sup>19, 91</sup> Expressing AQP1 in AQP0 null mice does not fully restore lens transparency or cellular architecture, providing further evidence that AQP0 has unique functions in fiber cells that are imperative for lens transparency.<sup>72</sup> The role of AQP5 in lens fiber cells is unknown; however, it has been suggested that AQP5 trafficking to the membrane could enhance water permeability in the lens to compensate for the shift of AQP0 to its junctional form.<sup>58</sup>

### *AQP0 Sequence and Modifications*

As a long-lived protein, AQP0 accumulates numerous modifications during its lifetime (Figure 1.7).<sup>58, 92, 93</sup> Early studies from Takemoto *et al* used amino acid analysis to determine the partial sequence of N-terminal and C-terminal fragments of bovine MIP generated by cyanogen bromide (CNBr) and trypsin.<sup>94</sup> Based on these results, the full amino acid sequence was later deduced from cDNA copies of AQP0 mRNA.<sup>51</sup> Using a radiolabeling approach, AQP0 was identified as a phosphoprotein in 1986. Since then, mass spectrometry has proven an important tool for identifying site-specific modifications to AQP0. Initial studies bovine AQP0 used CNBr to generate peptide fragments and mass spectrometry to yield complete sequence coverage and major phosphorylation sites of AQP0.<sup>95</sup> As sample preparation techniques and mass spectrometry instrumentation have improved, more modifications have been characterized. Recent studies have identified novel modifications, protein-protein crosslinks, and spatial changes to AQP0 based on fiber cell age.<sup>58, 96-98</sup>

AQP0 truncation is apparent in rat lens, detected by MALDI mass spectrometry and loss of antibody reactivity.<sup>61</sup> In mouse lens, AQP0 truncation occurs at L234 and K238 at day 6.<sup>65</sup> Presumably, AQP0 truncation in mouse and rat lens is due to enzymatic cleavage by calpain, which is known to exist at high levels in rodent lens. In humans, AQP0 cleavage has also been shown to increase over time.<sup>93</sup> However, several pieces of evidence indicate human AQP0 truncation is a nonenzymatic process. First, different truncation sites are detected in rodent and human lens.<sup>61, 65, 93</sup> Furthermore, although calpain has been found in human lens, it is present at low levels and there is little enzymatic activity in mature fiber cells. The major truncation sites in human lens AQP0 are on the C-terminal side of asparagine residues Asn-246 and Asn-259, as well as aspartic acid Asp-243.<sup>93</sup> There is extensive evidence that labile asparagine residues form a cyclic intermediate prone to spontaneous backbone cleavage.<sup>99</sup> Deamidation-related cleavage has also been documented in lens crystallins,<sup>100</sup> and spontaneous backbone cleavage of an AQP0 peptide at Asn-246 and Asn-259 was observed *in vitro* after heated incubation.<sup>101</sup> Therefore, it is likely that major human AQP0 truncation events proceed through deamidation events. The functional consequences of AQP0 truncation remain to be determined, as recent studies have shown both full-length and truncated AQP0 can act as adhesional molecules.<sup>88</sup> Removal of the AQP0 C-terminus prevents several protein-protein interactions but may open the protein to new binding interactions, which could affect AQP0 function as a water channel and structural molecule.

Numerous phosphorylation sites have been identified in lens. Initial studies determined Ser-235 was the major phosphorylation site in bovine lens.<sup>95</sup> Additional phosphorylation sites have also been reported and quantified (see Figure 1.7).<sup>96, 102</sup> Ser-235 phosphorylation is required for AQP0 translocation to the membrane in RK13 cells<sup>79</sup> and is important for regulating AQP0

permeability. Phosphorylation at Ser-235 reduces AQP0 binding affinity to calmodulin,<sup>77</sup> increasing water permeability of the channel.

Recently, fatty acid acylation was reported on Met-1 and Lys-238 of AQP0.<sup>97</sup> These residues were found to be modified by palmitic and oleic acid. Although the functional consequences of AQP0 acylation are not well understood, initial studies showed the lipidated form of AQP0 purifies with detergent-resistant lipid raft fractions of the plasma membrane. This raises the hypothesis that fatty acid acylation could affect AQP0 trafficking to specific plasma membrane domains. AQP0 is present in several distinct plasma membrane microdomains<sup>62</sup> and its permeability is affected by the lipid composition of the surrounding membrane.<sup>103</sup> Thus, lipidation could modulate AQP0 permeability by altering plasma membrane localization.

Age-related PTMs in the lens include deamidation, racemization, isomerization, oxidation, truncation, and protein-protein crosslinks; many of these have been reported on AQP0.<sup>93, 98, 101</sup> It is not surprising that extremely old lens proteins are posttranslationally modified over time. The lens is often considered a long-lived reaction flask, where proteins incubate at elevated temperatures for decades. While some protein modifications may be programmed to occur in a specific region of the lens, where metabolic activity enables enzymatic reactions, many PTMs accumulate in a time-dependent manner with age. In a tissue where no new protein can be synthesized, modifications may serve as a way to modulate protein function over time or may deleteriously affect protein function. Additional studies are required to fully understand the functional implications of lens protein PTMs, including which modifications promote lens transparency or contribute to cataract.

**Figure 1.7**

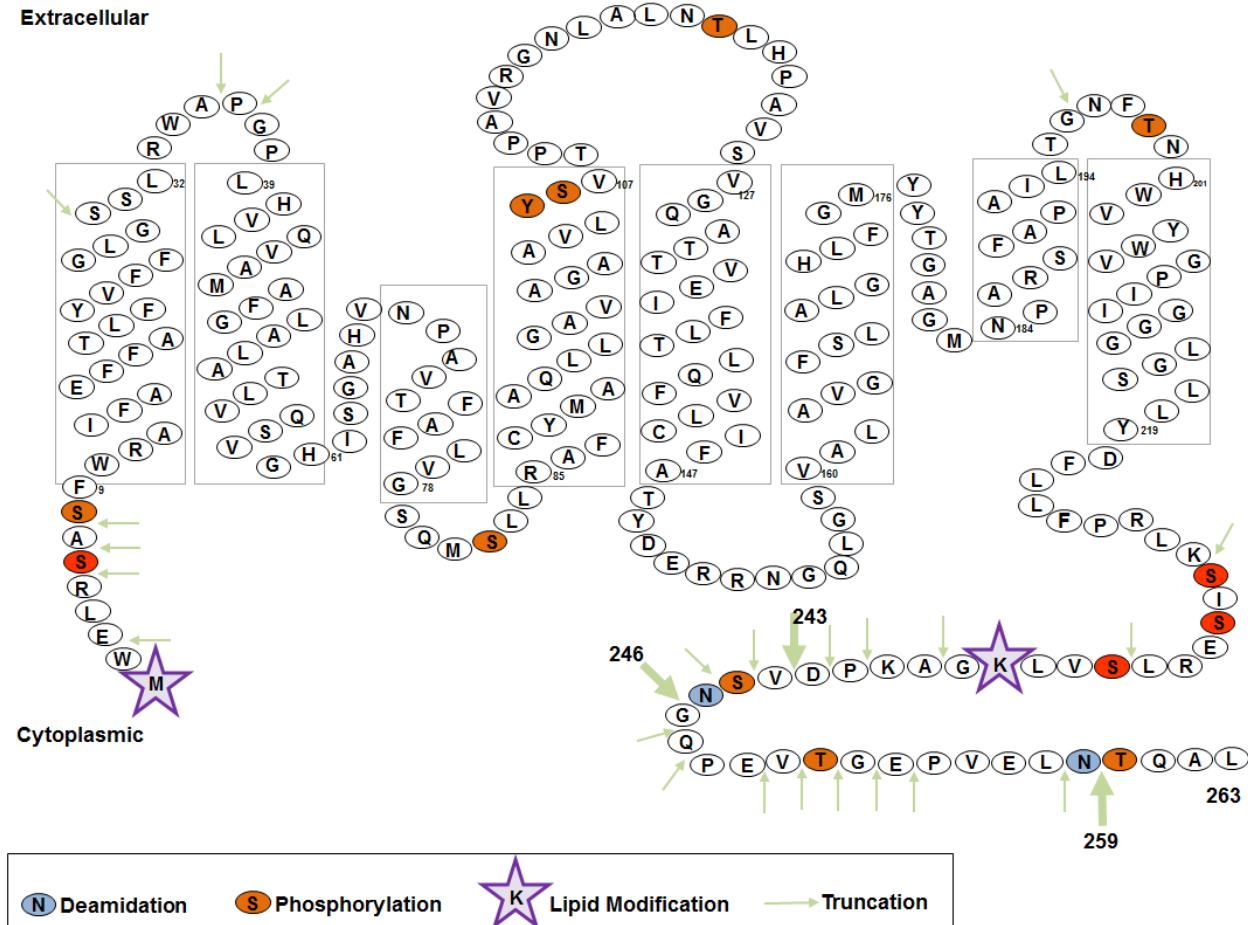


**Figure 1.7.** Amino Acid Sequence and Post-Translational Modifications of Human AQP0. The 263-amino acid protein undergoes both N- and C-terminal truncation at multiple sites. Larger arrows indicate the major sites of truncation on the protein C-terminus. Note that two major cleavage sites follow asparagine residues known to be deamidated. Phosphorylation has been reported on Ser, Thr, and Tyr residues; recently-identified phosphorylation sites are marked in orange. Fatty acid acylation of the N-terminal Met and Lys-238 have been reported; these residues can be modified by palmitic and/or oleic acid. Gray boxes indicate residues are embedded within the plasma membrane.

### *AQP0 and Disease*

Although a total of 20 autosomal dominant mutations in AQP0 are reported to cause cataract in humans, mutations in other lens aquaporins have not been associated with lens phenotypes in humans. AQP1 null mice show accelerated cataract development upon stress,<sup>60</sup> although humans with AQP1 mutations do not show signs of cataract.<sup>104</sup> There are no indications of natural lens opacities in AQP5 null mice, although these animals are more susceptible to hypoglycemic cataract.<sup>55, 105, 106</sup> The critical importance of AQP0 in the lens is highlighted by the fact that mutations in the AQP0 gene lead to congenital cataracts. AQP0 mutations can cause improper trafficking (AQP0 sequestration in the endoplasmic reticulum), disruption of protein interactions, and altered permeability. Varadaraj et al. found that Δ213, a single base deletion that leads to shortened AQP0 sequence in humans, results in protein sequestration in the ER.<sup>107</sup> Families with G165D mutation also have impaired AQP0 trafficking.<sup>108</sup> Another mutation, R233K, does not affect AQP0 localization to the plasma membrane but reduces binding to calmodulin, a regulatory calcium-binding protein.<sup>109</sup> Several other familial AQP0 mutations have also been reported.<sup>110-118</sup> All of these AQP0 mutations cause congenital cataract.

### *Future Research*

Although lens aquaporins have been studied for decades, a number of questions remain about AQP0 modifications and function in lens. Modified forms of AQP0 have been characterized by LC-MS/MS and MALDI IMS, but little is known about age-related changes to each modified form of the protein. Deamidation remains difficult to characterize, due to the extremely small mass shift caused by asparagine conversion to aspartic acid. It remains unclear whether AQP0 truncation affects function and/or protein-protein interactions in the aging lens, or

whether it is simply a consequence of long-lived proteins surviving for decades in the lens. Furthermore, understanding these modifications in the context of the lens as a whole, i.e. how they affect AQP0/protein interactions, will be critical for characterizing the function of each modified form of AQP0.

## **Spatially-Resolved Proteomics**

### *The Necessity for Spatial Information*

The lens grows throughout the lifetime of the individual. New fiber cells are added to the lens outer cortex, surrounding older fiber cells in the lens core. Due to the unique structure of the lens, an age gradient radiates from the oldest cells in the lens core to younger cells in the outer cortex. Fiber cell localization in the lens reflects the age of fiber cells and the proteins within. Therefore, retaining protein spatial information is critical for understanding differentiation- and age-related modifications in lens, as the biochemical mechanisms for these processes have not been completely elucidated. In this section, I will describe common techniques used to characterize molecules based on their spatial localization within the lens. Newer technologies enable the detection of thousands of analytes from one sample while maintaining spatial information, driving the discovery of new post-translational modifications associated with specific time points in lens fiber cell development, differentiation, and aging.

### *Challenges to Membrane Protein Analysis*

Integral membrane protein analysis brings unique challenges. Membrane proteins are extremely hydrophobic, often requiring solubilization with specific reagents like urea and detergents. Although helpful, these reagents must be used carefully as they can interfere with

downstream analysis by mass spectrometry. Additionally, integral membrane proteins contain transmembrane domains that are buried within the lipid bilayer of the plasma membrane. As a result, a significant portion of these proteins is inaccessible to enzymatic digestion and achieving full sequence coverage of membrane proteins can be a difficult task. Furthermore, because of the aforementioned challenges, membrane proteins are not typically detected in samples that have not been enriched for insoluble proteins. Sample preparation techniques are often tailored for membrane protein analysis and include washing and centrifugation steps to pellet the plasma membrane, followed by stringent washes to remove associated soluble proteins. Still, advances in sample preparation and technology have enabled full sequence coverage and identification of site-specific modifications of AQP0 in lens. Although AQP0 is fairly well characterized, remaining questions require additional studies.

### *Proteomics*

Proteomics is the study of protein molecules and populations within biological samples. Mass spectrometry is a widespread proteomics tool used to characterize the multitude of proteins within a sample, providing data on relative protein abundance, amino acid sequence, and post-translational modifications. The instrumental workflow, which involves extensive sample preparation (discussed in following sections), usually involves a separation step prior to analysis in the mass spectrometer.

A common strategy used today is bottom-up proteomics, named because the approach generates smaller peptide fragment sequences that are used to gain information about larger proteins from which they originated.<sup>119</sup> Bottom-up proteomics employs enzymes, typically trypsin, to digest proteins into smaller proteolytic peptide fragments. These peptides can be

efficiently separated using liquid chromatography (LC) before introduction into the mass spectrometer. This fractionation step reduces sample complexity, which is helpful for identifying more peptides in a single sample. After the sample has been introduced to the instrument using electrospray ionization, full mass or  $\text{MS}^1$  spectra are collected for these peptide fragments, reflecting the mass-to-charge ( $m/z$ ) value and intensity of peptides within a single time point in the chromatogram. Based on user-designed instrumental parameters in a data dependent acquisition mode, the most intense peaks in the  $\text{MS}^1$  spectrum are then selected for fragmentation via collision-induced dissociation (CID), generating a tandem or  $\text{MS}/\text{MS}$  ( $\text{MS}^2$ ) spectrum that shows the fragments for the peptide. Fragmentation along the peptide backbone is fairly predictable. CID fragmentation generates b- and y-ions that collectively describe the amino acid sequence of the peptide. Bioinformatics tools can be used to search  $\text{MS}^2$  data against a database of predicted fragmentation spectra based on known peptide sequences. The output from this search is a list of peptide identifications, which are assumed to represent the presence of the larger protein in the sample. Protein abundance can be relatively quantified based on spectral counts, the number of times representative peptides from that protein are identified within a sample. Peak area, the area under the extracted ion chromatogram for a given peptide  $m/z$ , is also used to measure protein abundance. Absolute quantitation requires specific instrumentation, isotopic labeling, and/or internal standards and will be discussed in Chapter 3.

### *Cell or Tissue Homogenization*

Sample preparation is critical for generating a homogeneous mixture of peptides or proteins for LC-MS/MS analysis. Different methods provide varying spatial resolution and confer unique advantages. Traditionally, bulk tissue or cells are homogenized using manual or

electric tools to break apart cells into a homogeneous mixture prior to downstream analysis. Although informative, homogenization provides analysis of bulk tissue, meaning all spatial information about analyte localization within the tissue is lost. Therefore, standard homogenization is not as informative for studying the lens aging process over time. Furthermore, homogenizing several populations of cells makes it challenging to detect highly-localized but lower-abundance species in a sample.

Instead of homogenizing an entire piece of tissue, manual dissection with trephines or tweezers is commonly used to separate tissue into several regions of interest. Manual dissection yields gross information about organ substructure with a spatial resolution of several millimeters, dependent on the technique used. In lens, manual dissection has been used to isolate concentric rings,<sup>120</sup> successfully separating cortical and nuclear regions to study age-related changes.<sup>32, 93, 101</sup> However, dissection reproducibility can be challenging, given the technique is usually based on ‘eyeball’ measurements.

### *Laser Capture Microdissection*

Laser capture microdissection (LCM) is a higher spatial resolution technique used to isolate narrow tissue regions from thin tissue sections. Tissue is prepared (fixed or frozen), sectioned onto a glass slide, and stained or labeled to highlight regions of interest. Using a microscope as a guide, the researcher selects regions to isolate (usually tens of microns or larger in diameter). A laser cuts around the tissue region, which is then catapulted into an Eppendorf cap using another laser pulse. This procedure is repeated until enough tissue is pooled to lyse cells for downstream analysis. LCM is compatible with LC-MS/MS analysis, enabling the identification of peptides within the sample.<sup>58</sup> LCM is precise but rather time-consuming, as the

procedure must be continued until sufficient tissue is collected for LC-MS/MS. The amount of tissue or cells required for analysis is often determined empirically for each experiment. It is also important to consider whether the stain is compatible with downstream mass spectrometry analysis.

### *Microextraction and Hydrogels*

Recently, microextraction approaches have been used to extract peptides or proteins from discrete areas of tissue sections.<sup>121</sup> Gel-loading pipet tips are useful for pipeting and extracting small amounts of solvent from millimeter-sized regions. Solvent (e.g. 20% ACN) is placed onto the tissue section and aspirated repeatedly to solubilize and extract proteins and peptides from the tissue (Figure 1.8).<sup>121</sup> The extract can then be analyzed by LC-MS/MS. Hydrogels containing solvent or digestive enzymes have also been used to extract peptides directly from tissue.<sup>122, 123</sup> The hydrogel is placed on a region of interest, incubated overnight, and removed to an eppendorf tube where it undergoes a series of hydration and dehydration washes to extract proteins from the gel. Results indicate this hands-off method is quite effective at identifying numerous proteins within a sample, although the spatial resolution is limited by the diameter of the solvent droplet or hydrogel (typically millimeters in diameter).<sup>121-123</sup> These techniques can be useful for isolating analytes from populations of cells or specific regions of tissue that have been targeted for further study based on molecular or pathological analysis. This approach is particularly useful in combination with MALDI IMS to identify imaged signals.

**Figure 1.8**

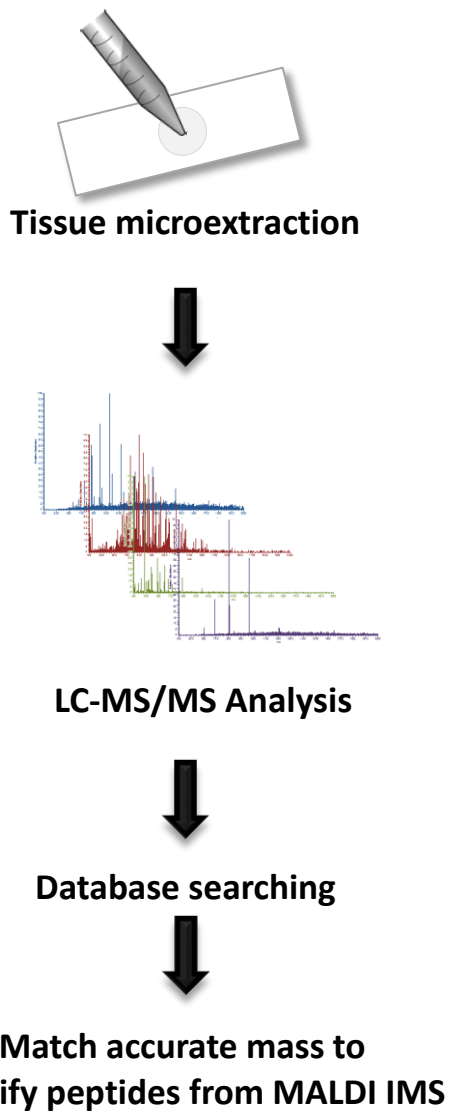


**Figure 1.8.** Tissue Microextraction Strategy for Identifying Localized Signals from MALDI IMS Experiments.

### *MALDI Mass Spectrometry: Profiling and Imaging*

MALDI, or matrix-assisted laser desorption ionization, mass spectrometry can be used to directly analyze proteins from a thin tissue section. This type of mass spectrometry employs a laser to ablate analyte and matrix molecules from a sample plate, followed by time of flight (TOF) mass analysis.<sup>124</sup> MALDI was developed simultaneously by the Tanaka<sup>125</sup> and Karas and Hillenkamp<sup>126</sup> labs in the late 1980s. Subsequently, Tanaka was recognized with a share of the 2002 Nobel Prize in Chemistry. Half of the Nobel prize recognizes the innovative mass spectrometry work of Tanaka and John Fenn, who discovered MALDI and electrospray ionization (ESI), respectively. Both soft ionization techniques were revolutionary for the analysis of large biomolecules. Although we used both MALDI and ESI for protein analysis, the focus of the current work is MALDI MS.

In MALDI, small conjugated organic molecules (matrix) are mixed with the analyte of interest. The matrix absorbs UV energy from a laser pulse, generating analyte ions as the mixture is desorbed from the sample surface. Ions are accelerated and allowed to drift through a field-free flight region before they reach the detector. Molecules are detected by their time of flight, the time it takes to reach the detector after traveling a fixed distance. Time of flight is proportional to the mass-to-charge ( $m/z$ ) of the molecule; all ions begin with the same kinetic energy, but smaller  $m/z$  species have greater velocity and thus arrive at the detector first. Each laser pulse generates a mass spectrum, with  $m/z$  values plotted along the x-axis and peak height representing intensity.

Direct analysis from tissue sections was demonstrated by Caprioli *et al.*<sup>127</sup> In profiling mode, matrix is spotted onto discrete regions of the tissue where mass spectra are collected. The spatial resolution of MALDI profiling is limited by the diameter of hand-pipetted or robotically-spotted matrix spots, usually millimeters in diameter. MALDI imaging mass spectrometry (IMS)

enables molecular mapping across thin tissue sections.<sup>127</sup> Matrix is applied to the entire sample surface and a defined region is selected for imaging. The laser samples from a discrete spot on the tissue, generating a mass spectrum. The sample stage is moved according to the raster step size, and in this fashion spectra are acquired across an entire tissue section (Figure 1.9).<sup>128</sup>

Spectra are averaged and signals can be plotted to generate ion images, with intensity encoded as a heat map. Hundreds to thousands of *m/z* signals are detected in a single experiment. MALDI MS does not require staining or antibodies for tissue imaging. Lipid, metabolite, and protein signals can be generated from tissue sections, depending on sample preparation steps and matrix type. Therefore, this technology is especially useful for detecting post-translational modifications (PTMs) in lens, which can be distinguished from the unmodified protein by a specific shift in *m/z* value. Currently, routine MALDI IMS experiments are performed at 10-15 $\mu\text{m}$  raster step size. Effective spatial resolution is limited by sample preparation (washing steps) which can cause analyte delocalization, laser spot size and stage stepping motor limits, as well as matrix application techniques that can result in different matrix crystal size. Improvements to the technology, including smaller laser footprint and higher laser frequency, allow rapid collection of high spatial resolution imaging data.

Although useful, MALDI IMS has some limitations. A major challenge in the field is to identify the *m/z* signals detected in the imaging experiment. Usually, complementary techniques like microextraction or tissue homogenization, followed by LC-MS/MS, are used in tandem with MALDI IMS to accurately identify peptides or proteins.<sup>121</sup> MALDI IMS also has limited dynamic range due to instrumentation and may detect less species than a typical LC-MS/MS run because there is no formal analyte separation step. High molecular weight proteins can be difficult to analyze on most commercial MALDI TOF instrumentation. Furthermore, analyte

solubility is a critical component of analysis and membrane proteins often require careful sample preparation to enable their detection. Tissue- or analyte-specific washing and enrichment steps can be used to tailor analysis for specific analytes to overcome this issue.<sup>129-131</sup>

**Figure 1.9**

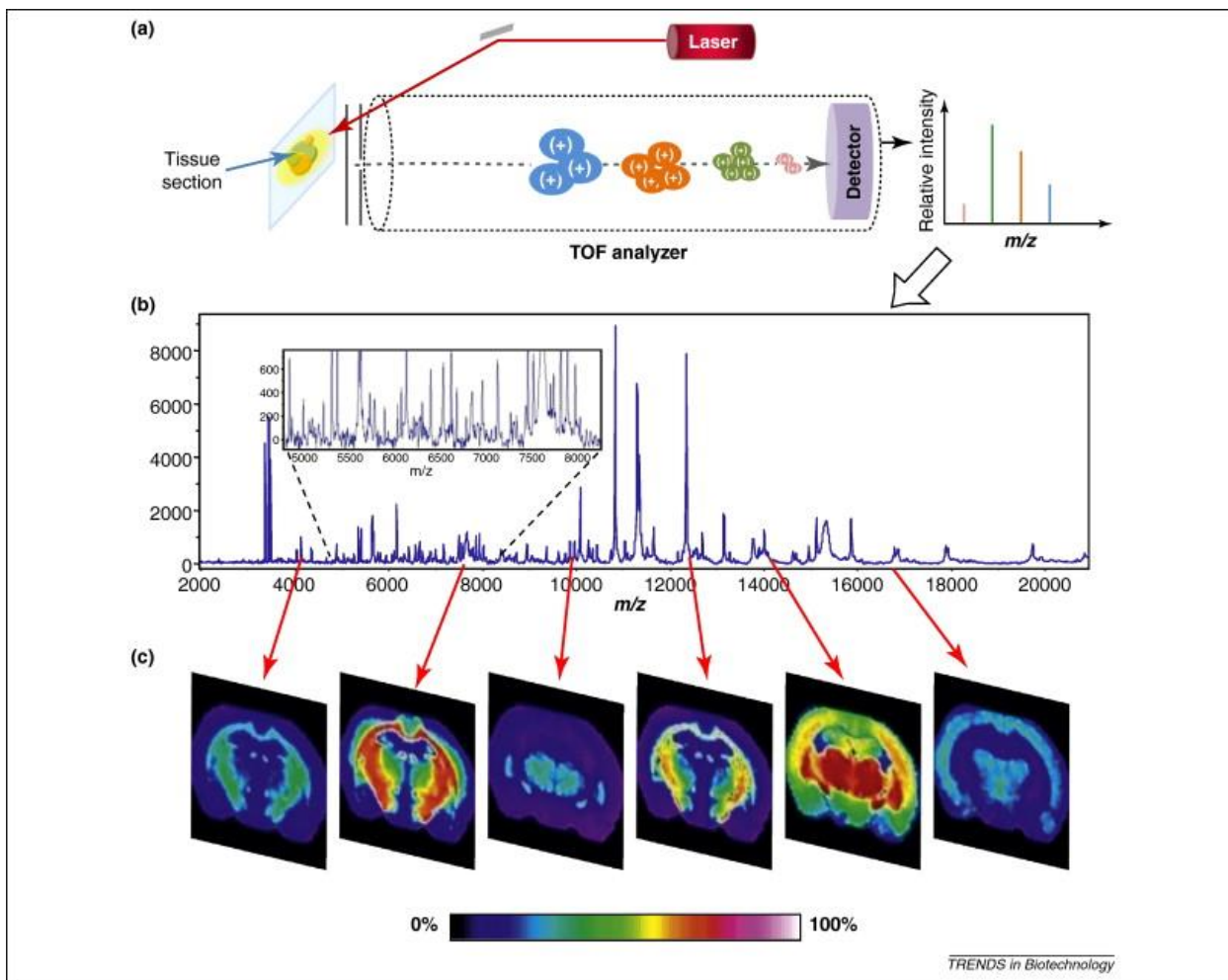


**Figure 1.9.** Schematic of the MALDI IMS Process.

(a) A tissue section on a conductive slide is placed in the source of the instrument and a laser is fired at the surface to desorb and ionize molecules. Analytes from each spot are separated in the time of flight (TOF) analyzer, their flight times converted to a mass-to-charge ratio ( $m/z$ ), and a spectrum recorded. (b) A representative mass spectrum collected from a tissue section. Inset shows detail and complexity of the spectrum collected. A tissue imaging experiment might result in thousands of such spectra. (c) Using an average spectrum from the entire section, ion images can be generated from each peak. Each  $m/z$  value of interest can be displayed as a function of position in the tissue section and relative intensity. Hundreds of such images can be created from a single tissue section.

**Reprinted with permission from** Seeley EH, Caprioli RM. MALDI imaging mass spectrometry of human tissue: method challenges and clinical perspectives. Trends Biotechnol 2011;29:136-143.<sup>127</sup>

### *Advantages of Mass Spectrometry-based Proteomics*

Historically, immunohistochemistry and confocal immunofluorescence microscopy have been used to visualize protein localization within tissue sections. However, the use of antibodies for imaging requires *a priori* knowledge of the analyte of interest and specific antibodies for each protein or isomer. The spatially-resolved analytical techniques presented above are often more informative, providing information on hundreds to thousands of proteins or peptides in a given experiment and requiring no advanced knowledge of the sample composition.<sup>128</sup> The number of analytes detected in a single experiment depends on each molecule having a unique *m/z* value, as well as the mass resolution and sensitivity of the instrument. Furthermore, mass spectrometry can provide site-specific information on numerous protein PTMs, which cause a shift in detected *m/z*. Immunohistochemistry cannot distinguish between modified forms of a protein unless a specific antibody directed against that modification is used. For our experimental purposes, a combination of the spatially-resolved proteomic techniques described above were employed to analyze human lens protein changes correlated with fiber cell development, differentiation, and aging.

## **Summary and Research Objectives**

The experiments detailed herein were designed to distinguish where certain AQP0 and other protein modifications occur spatially within the lens, and whether their distribution changes based on the level of fiber cell differentiation or age. Our quantitative, high spatial resolution data is essential for understanding the spatial and temporal programming of these modifications in the aging lens and how they may modulate AQP0 function over time.

### *Specific Aims*

#### **Aim I. Image Modified Forms of AQP0 in the Human Lens using MALDI IMS**

The goal of Aim 1 is to use MALDI imaging mass spectrometry (IMS) to characterize the spatial distribution of modified forms of Aquaporin-0 (AQP0) in human lens. Mapping protein localization can provide clues about age-related posttranslational modifications because the lens contains both young cells in the cortex and old cells in the core. By analyzing a wide age range of human lenses, it is possible to visualize age-related changes to AQP0 that could modulate its function over time.

#### **Aim II. Quantify Site-Specific Protein Modifications in Distinct Lens Regions using LCM and Targeted LC-MS/MS**

Aim 2 is focused on the remodeling zone of the human lens, a region of membrane ruffling and disorganization approximately 100 $\mu$ m beneath the human lens capsule.<sup>12, 13</sup> The function of this zone has not been determined. I hypothesize that membrane or membrane-associated proteins could be responsible for this dramatic change in membrane organization.

## References

1. Schey KL, Wang Z, Wenke JL, Qi Y. Aquaporins in the eye: expression, function, and roles in ocular disease. *Biochim Biophys Acta* 2014;1840:1513-1523.
2. NEI. Cataracts.Eye Data: Cataracts.
3. Ellwein LB, Urato CJ. Use of eye care and associated charges among the Medicare population: 1991-1998. *Arch Ophthalmol* 2002;120:804-811.
4. Kupfer C. Bowman lecture. The conquest of cataract: a global challenge. *Trans Ophthalmol Soc U K* 1985;104 ( Pt 1):1-10.
5. Vadlapudi AD, Patel A, Cholkar K, Mitra AK. Recent Patents on Emerging Therapeutics for the Treatment of Glaucoma, Age Related Macular Degeneration and Uveitis. *Recent Pat Biomed Eng* 2012;5:83-101.
6. McIlwain J. *An Introduction to the Biology of Vision*. Cambridge: Cambridge University Press; 1996.
7. Gilbert SF. *Developmental Biology*. Sunderland, MA: Sinauer; 2006.
8. Charlton-Perkins M, Brown NL, Cook TA. The lens in focus: a comparison of lens development in Drosophila and vertebrates. *Mol Genet Genomics* 2011;286:189-213.
9. Bassnett S. Lens organelle degradation. *Exp Eye Res* 2002;74:1-6.
10. Bassnett S. On the mechanism of organelle degradation in the vertebrate lens. *Experimental Eye Research* 2009.
11. Bassnett S, Shi Y, Vrensen GF. Biological glass: structural determinants of eye lens transparency. *Philos Trans R Soc Lond B Biol Sci* 2011;366:1250-1264.
12. Lim JC, Walker KL, Sherwin T, Schey KL, Donaldson PJ. Confocal microscopy reveals zones of membrane remodeling in the outer cortex of the human lens. *Invest Ophthalmol Vis Sci* 2009;50:4304-4310.
13. Costello MJ, A. M, Gilliland KO, Fowler WC, Johnsen S. Ultrastructural analysis of the human lens fiber cell remodeling zone and the initiation of cellular compaction. *Exp Eye Res* 2013;116:411-418.
14. Biswas SK, Lee JE, Brako L, Jiang JX, Lo WK. Gap junctions are selectively associated with interlocking ball-and-sockets but not protrusions in the lens. 2010;16:2328-2341.
15. Chepelinsky AB. Structural function of MIP/aquaporin 0 in the eye lens; genetic defects lead to congenital inherited cataracts. *Handb Exp Pharmacol* 2009;265-297.

16. Wang H, Zhang T, Wu D, Zhang J. A novel beaded filament structural protein 1 (BFSP1) gene mutation associated with autosomal dominant congenital cataract in a Chinese family. *Mol Vis* 2013;19:2590-2595.
17. Ma X, Li FF, Wang SZ, Gao C, Zhang M, Zhu SQ. A new mutation in BFSP2 (G1091A) causes autosomal dominant congenital lamellar cataracts. *Mol Vis* 2008;14:1906-1911.
18. Lo WK, Biswas SK, Brako L, Shiels A, Gu S, Jiang JX. Aquaporin-0 targets interlocking domains to control the integrity and transparency of the eye lens. *Invest Ophthalmol Vis Sci* 2014;55:1202-1212.
19. Al-Ghoul KJ, Kirk T, Kuszak AJ, Zoltoski RK, Shiels A, Kuszak JR. Lens structure in MIP-deficient mice. *Anat Rec A Discov Mol Cell Evol Biol* 2003;273:714-730.
20. Yoon KH, Blankenship T, Shibata B, Fitzgerald PG. Resisting the effects of aging: a function for the fiber cell beaded filament. *Invest Ophthalmol Vis Sci* 2008;49:1030-1036.
21. Alizadeh A, Clark JI, Seeberger T, et al. Targeted genomic deletion of the lens-specific intermediate filament protein CP49. *Invest Ophthalmol Vis Sci* 2002;43:3722-3727.
22. Alizadeh A, Clark J, Seeberger T, Hess J, Blankenship T, Fitzgerald PG. Targeted deletion of the lens fiber cell-specific intermediate filament protein filensin. *Invest Ophthalmol Vis Sci* 2003;44:5252-5258.
23. Sandilands A, Prescott Ar Fau - Wegener A, Wegener A Fau - Zoltoski RK, et al. Knockout of the intermediate filament protein CP49 destabilises the lens fibre cell cytoskeleton and decreases lens optical quality, but does not induce cataract. 2003.
24. Kasturirangan S, Markwell EL, Atchison DA, Pope JM. In vivo study of changes in refractive index distribution in the human crystalline lens with age and accommodation. *Invest Ophthalmol Vis Sci* 2008;49:2531-2540.
25. Friedrich MG, Truscott RJ. Membrane association of proteins in the aging human lens: profound changes take place in the fifth decade of life. *Invest Ophthalmol Vis Sci* 2009;50:4786-4793.
26. Mathias RT, Rae JL, Baldo GJ. Physiological properties of the normal lens. *Physiol Rev* 1997;77:21-50.
27. Candia OA, Mathias R, Gerometta R. Fluid circulation determined in the isolated bovine lens. *Invest Ophthalmol Vis Sci* 2012;53:7087-7096.
28. Mathias RT, Kistler J, Donaldson P. The lens circulation. *J Membr Biol* 2007;216:1-16.
29. Slavi N, Rubinos C, Li L, et al. Connexin 46 (cx46) gap junctions provide a pathway for the delivery of glutathione to the lens nucleus. *J Biol Chem* 2014;289:32694-32702.

30. Sweeney MH, Truscott RJ. An impediment to glutathione diffusion in older normal human lenses: a possible precondition for nuclear cataract. *Exp Eye Res* 1998;67:587-595.
31. Moffat BA, Landman KA, Truscott RJ, Sweeney MH, Pope JM. Age-related changes in the kinetics of water transport in normal human lenses. *Exp Eye Res* 1999;69:663-669.
32. Heys KR, Friedrich MG, Truscott RJW. Presbyopia and heat: changes associated with aging of the human lens suggest a functional role for the small heat shock protein,  $\alpha$ -crystallin, in maintaining lens flexibility. *Aging Cell* 2007;6:807-815.
33. Truscott RJ. Age-related nuclear cataract-oxidation is the key. *Exp Eye Res* 2005;80:709-725.
34. Congdon NG. Prevention strategies for age related cataract: present limitations and future possibilities. *Br J Ophthalmol* 2001;85:516-520.
35. Hooi MY, Raftery MJ, Truscott RJ. Accelerated aging of Asp 58 in alphaA crystallin and human cataract formation. *Exp Eye Res* 2013;106:34-39.
36. Hooi MY, Raftery MJ, Truscott RJ. Racemization of two proteins over our lifespan: deamidation of asparagine 76 in gammaS crystallin is greater in cataract than in normal lenses across the age range. *Invest Ophthalmol Vis Sci* 2012;53:3554-3561.
37. Yang Z, Su D, Li Q, et al. A R54L mutation of CRYAA associated with autosomal dominant nuclear cataracts in a Chinese family. *Curr Eye Res* 2013;38:1221-1228.
38. Denker BM, Smith BL, Kuhajda FP, Agre P. Identification, purification, and partial characterization of a novel Mr 28,000 integral membrane protein from erythrocytes and renal tubules. *J Biol Chem* 1988;263:15634-15642.
39. Benga G, Popescu O, Pop VI. Water exchange through erythrocyte membranes: p-chloromercuribenzene sulfonate inhibition of water diffusion in ghosts studied by a nuclear magnetic resonance technique. *Biosci Rep* 1985;5:223-228.
40. Zeidel ML, Ambudkar SV, Smith BL, Agre P. Reconstitution of functional water channels in liposomes containing purified red cell CHIP28 protein. *Biochemistry* 1992;31:7436-7440.
41. Preston GM, Carroll TP, Guggino WB, Agre P. Appearance of water channels in Xenopus oocytes expressing red cell CHIP28 protein. *Science* 1992;256:385-387.
42. Preston GM, Agre P. Isolation of the cDNA for erythrocyte integral membrane protein of 28 kilodaltons: member of an ancient channel family. *Proc Natl Acad Sci U S A* 1991;88:11110-11114.

43. Reizer J, Reizer A, Saier MH, Jr. The MIP family of integral membrane channel proteins: sequence comparisons, evolutionary relationships, reconstructed pathway of evolution, and proposed functional differentiation of the two repeated halves of the proteins. *Crit Rev Biochem Mol Biol* 1993;28:235-257.
44. Alcala J, Lieska N, Maisel H. Protein composition of bovine lens cortical fiber cell membranes. *Exp Eye Res* 1975;21:581-595.
45. Bagchi M, Gordon PA, Alcala JR, Maisel H. The plasma membrane of the rabbit lens cortical fiber. I. Isolation, characterization, and biosynthesis of two membrane intrinsic polypeptides. *Invest Ophthalmol Vis Sci* 1979;18:562-569.
46. Broekhuyse RM, Kuhlmann ED, Stols AL. Lens membranes II. Isolation and characterization of the main intrinsic polypeptide (MIP) of bovine lens fiber membranes. 1976;23:365-371.
47. Chepelinsky AB. The ocular lens fiber membrane specific protein MIP/Aquaporin 0. *Journal of experimental zoology Part A, Comparative experimental biology* 2003;300:41-46.
48. Zampighi GA, Hall JE, Ehring GR, Simon SA. The structural organization and protein composition of lens fiber junctions. *J Cell Biol* 1989;108:2255-2275.
49. Chandy G, Zampighi GA, Kreman M, Hall JE. Comparison of the water transporting properties of MIP and AQP1. *J Membr Biol* 1997;159:29-39.
50. Mulders SM, Preston GM, Deen PM, Guggino WB, van Os CH, Agre P. Water channel properties of major intrinsic protein of lens. *J Biol Chem* 1995;270:9010-9016.
51. Gorin MB, Yancey SB, Cline J, Revel JP, Horwitz J. The major intrinsic protein (MIP) of the bovine lens fiber membrane: characterization and structure based on cDNA cloning. *Cell* 1984;39:49-59.
52. Harries WEC, Akhavan D, Miercke LJW, Khademi S, Stroud RM. The channel architecture of aquaporin 0 at a 2.2-Å resolution. *Proceedings of the National Academy of Sciences of the United States of America* 2004;101:14045-14050.
53. Gonen T, Sliz P, Kistler J, Cheng Y, Walz T. Aquaporin-0 membrane junctions reveal the structure of a closed water pore. *Nature* 2004;429:193-197.
54. Hamann S, Zeuthen T, La Cour M, et al. Aquaporins in complex tissues: distribution of aquaporins 1-5 in human and rat eye. *Am J Physiol* 1998;274:C1332-1345.
55. Kumari SS, Varadaraj M, Yerramilli VS, Menon AG, Varadaraj K. Spatial expression of aquaporin 5 in mammalian cornea and lens, and regulation of its localization by phosphokinase A. *Mol Vis* 2012;18:957-967.

56. Grey AC, Walker KL, Petrova RS, et al. Verification and spatial localization of aquaporin-5 in the ocular lens. *Exp Eye Res* 2013;108:94-102.
57. Tran TL, Bek T, Holm L, et al. Aquaporins 6-12 in the human eye. *Acta Ophthalmol* 2013;91:557-563.
58. Wang Z, Han J, Schey KL. Spatial differences in an integral membrane proteome detected in laser capture microdissected samples. *J Proteome Res* 2008;7:2696-2702.
59. Patil RV, Saito I, Yang X, Wax MB. Expression of aquaporins in the rat ocular tissue. *Exp Eye Res* 1997;64:203-209.
60. Ruiz-Ederra J, Verkman AS. Accelerated cataract formation and reduced lens epithelial water permeability in aquaporin-1-deficient mice. *Invest Ophthalmol Vis Sci* 2006;47:3960-3967.
61. Grey AC, Li L, Jacobs MD, Schey KL, Donaldson PJ. Differentiation-dependent modification and subcellular distribution of aquaporin-0 suggests multiple functional roles in the rat lens. *Differentiation* 2009;77:70-83.
62. Zampighi GA, Eskandari S, Hall JE, Zampighi L, Kreman M. Micro-domains of AQP0 in lens equatorial fibers. *Exp Eye Res* 2002;75:505-519.
63. Simon SA, Zampighi G, McIntosh TJ, Costello MJ, Ting-beall HP, Robertson JD. The structure of junctions between lens fiber cells. *Biosci Rep* 1982;2:333-341.
64. Gonen T, Cheng Y, Kistler J, Walz T. Aquaporin-0 membrane junctions form upon proteolytic cleavage. *J Mol Biol* 2004;342:1337-1345.
65. Petrova RS, Schey KL, Donaldson PJ, Grey AC. Spatial distributions of AQP5 and AQP0 in embryonic and postnatal mouse lens development. *Exp Eye Res* 2015;132:124-135.
66. Pierscionek BK, Regini JW. The gradient index lens of the eye: an opto-biological synchrony. *Prog Retin Eye Res* 2012;31:332-349.
67. Gerometta R, Zamudio AC, Escobar DP, Candia OA. Volume change of the ocular lens during accommodation. *Am J Physiol Cell Physiol* 2007;293:C797-804.
68. Yang B, Verkman AS. Water and glycerol permeabilities of aquaporins 1-5 and MIP determined quantitatively by expression of epitope-tagged constructs in *Xenopus* oocytes. *J Biol Chem* 1997;272:16140-16146.
69. Virkki LV, Cooper GJ, Boron WF. Cloning and functional expression of an MIP (AQP0) homolog from killifish (*Fundulus heteroclitus*) lens. *Am J Physiol Regul Integr Comp Physiol* 2001;281:R1994-2003.

70. Calvanese L, Pellegrini-Calace M, Oliva R. Mutations at key pore-lining positions differentiate the water permeability of fish lens aquaporin from other vertebrates. *FEBS Lett* 2010;584:4797-4801.
71. Nemeth-Cahalan KL, Clemens DM, Hall JE. Regulation of AQP0 water permeability is enhanced by cooperativity. *J Gen Physiol* 2013;141:287-295.
72. Varadaraj K, Kumari SS, Mathias RT. Transgenic expression of AQP1 in the fiber cells of AQP0 knockout mouse: effects on lens transparency. *Exp Eye Res* 2010;91:393-404.
73. Nemeth-Cahalan KL, Hall JE. pH and calcium regulate the water permeability of aquaporin 0. *J Biol Chem* 2000;275:6777-6782.
74. Varadaraj K, Kumari S, Shiels A, Mathias RT. Regulation of aquaporin water permeability in the lens. *Invest Ophthalmol Vis Sci* 2005;46:1393-1402.
75. Reichow SL, Clemens DM, Freites JA, et al. Allosteric mechanism of water-channel gating by Ca<sup>2+</sup>-calmodulin. *Nat Struct Mol Biol* 2013;20:1085-1092.
76. Reichow SL, Gonon T. Noncanonical binding of calmodulin to aquaporin-0: implications for channel regulation. *Structure* 2008;16:1389-1398.
77. Rose KM, Wang Z, Magrath GN, Hazard ES, Hildebrandt JD, Schey KL. Aquaporin 0-calmodulin interaction and the effect of aquaporin 0 phosphorylation. *Biochemistry* 2008;47:339-347.
78. Kalman K, Nemeth-Cahalan KL, Froger A, Hall JE. Phosphorylation determines the calmodulin-mediated Ca<sup>2+</sup> response and water permeability of AQP0. *J Biol Chem* 2008;283:21278-21283.
79. Golestaneh N, Fan J, Zelenka P, Chepelinsky AB. PKC putative phosphorylation site Ser235 is required for MIP/AQP0 translocation to the plasma membrane. *Mol Vis* 2008;14:1006-1014.
80. Wang Z, Schey KL. Aquaporin-0 interacts with the FERM domain of ezrin/radixin/moesin proteins in the ocular lens. *Invest Ophthalmol Vis Sci* 2011;52:5079-5087.
81. Nakazawa Y, Oka M, Furuki K, Mitsuishi A, Nakashima E, Takehana M. The effect of the interaction between aquaporin 0 (AQP0) and the filensin tail region on AQP0 water permeability. *Mol Vis* 2011;17:3191-3199.
82. Lindsey Rose KM, Gourdie RG, Prescott AR, Quinlan RA, Crouch RK, Schey KL. The C terminus of lens aquaporin 0 interacts with the cytoskeletal proteins filensin and CP49. *Invest Ophthalmol Vis Sci* 2006;47:1562-1570.

83. Yu XS, Yin X, Lafer EM, Jiang JX. Developmental regulation of the direct interaction between the intracellular loop of connexin 45.6 and the C terminus of major intrinsic protein (aquaporin-0). *J Biol Chem* 2005;280:22081-22090.
84. Liu J, Xu J, Gu S, Nicholson BJ, Jiang JX. Aquaporin 0 enhances gap junction coupling via its cell adhesion function and interaction with connexin 50. *J Cell Sci* 2011;124:198-206.
85. Fotiadis D, Hasler L, Muller DJ, Stahlberg H, Kistler J, Engel A. Surface tongue-and-groove contours on lens MIP facilitate cell-to-cell adherence. *J Mol Biol* 2000;300:779-789.
86. Colom A, Casuso I, Boudier T, Scheuring S. High-speed atomic force microscopy: cooperative adhesion and dynamic equilibrium of junctional microdomain membrane proteins. *J Mol Biol* 2012;423:249-256.
87. Kumari SS, Varadaraj K. Intact AQP0 performs cell-to-cell adhesion. *Biochem Biophys Res Commun* 2009;390:1034-1039.
88. Kumari SS, Varadaraj K. Intact and N- or C-terminal end truncated AQP0 function as open water channels and cell-to-cell adhesion proteins: end truncation could be a prelude for adjusting the refractive index of the lens to prevent spherical aberration. *Biochim Biophys Acta* 2014;1840:2862-2877.
89. Shiels A, Mackay D, Bassnett S, Al-Ghoul K, Kuszak J. Disruption of lens fiber cell architecture in mice expressing a chimeric AQP0-LTR protein. *FASEB J* 2000;14:2207-2212.
90. Watanabe K, Wada K, Ohashi T, et al. A 5-bp insertion in Mip causes recessive congenital cataract in KFRS4/Kyo rats. *PLoS One* 2012;7:e50737.
91. Shiels A, Bassnett S, Varadaraj K, et al. Optical dysfunction of the crystalline lens in aquaporin-0-deficient mice. *Physiol Genomics* 2001;7:179-186.
92. Schey KL, Little M, Fowler JG, Crouch RK. Characterization of human lens major intrinsic protein structure. *Invest Ophthalmol Vis Sci* 2000;41:175-182.
93. Korlimbinis A, Berry Y, Thibault D, Schey KL, Truscott RJ. Protein aging: truncation of aquaporin 0 in human lens regions is a continuous age-dependent process. *Exp Eye Res* 2009;88:966-973.
94. Takemoto LJ, Hansen JS, Nicholson BJ, Hunkapiller M, Revel JP, Horwitz J. Major intrinsic polypeptide of lens membrane. Biochemical and immunological characterization of the major cyanogen bromide fragment. *Biochim Biophys Acta* 1983;731:267-274.
95. Schey KL, Fowler JG, Schwartz JC, Busman M, Dillon J, Crouch RK. Complete map and identification of the phosphorylation site of bovine lens major intrinsic protein. *Investigative ophthalmology & visual science* 1997;38:2508-2515.

96. Wang Z, Han J, David LL, Schey KL. Proteomics and phosphoproteomics analysis of human lens fiber cell membranes. *Invest Ophthalmol Vis Sci* 2013;54:1135-1143.
97. Schey KL, Gutierrez DB, Wang Z, Wei J, Grey AC. Novel Fatty Acid Acylation of Lens Integral Membrane Protein Aquaporin-0. *Biochemistry* 2010;49:9858-9865.
98. Wang Z, Lyons B Fau - Truscott RJW, Truscott Rj Fau - Schey KL, Schey KL. Human protein aging: modification and crosslinking through dehydroalanine and dehydrobutyryne intermediates. 2014.
99. Robinson NE, Robinson AB. *Molecular Clocks*. Cave Junction, OR: Althouse Press; 2004.
100. Voorter CE, A. dH-HW, van den Oetelaar PJ, Bloemendaal H, de Jong WW. Spontaneous peptide bond cleavage in aging alpha-crystallin through a succinimide intermediate. *J Biol Chem* 1988;263:19020-19023.
101. Ball LE, Garland DL, Crouch RK, Schey KL. Post-translational modifications of aquaporin 0 (AQP0) in the normal human lens: spatial and temporal occurrence. *Biochemistry* 2004;43:9856-9865.
102. Gutierrez DB, Garland D, Schey KL. Spatial analysis of human lens aquaporin-0 post-translational modifications by MALDI mass spectrometry tissue profiling. *Exp Eye Res* 2011;93:912-920.
103. Tong J, Carty JT, Briggs MM, McIntosh TJ. The water permeability of lens aquaporin-0 depends on its lipid bilayer environment. *Experimental Eye Research* 2013;113:32-40.
104. Preston GM, Smith BL, Zeidel ML, Moulds JJ, Agre P. Mutations in aquaporin-1 in phenotypically normal humans without functional CHIP water channels. *Science* 1994;265:1585-1587.
105. Ma T, Song Y, Gillespie A, Carlson EJ, Epstein CJ, Verkman AS. Defective secretion of saliva in transgenic mice lacking aquaporin-5 water channels. *J Biol Chem* 1999;274:20071-20074.
106. Kumari SS, Varadaraj K. Aquaporin 5 knockout mouse lens develops hyperglycemic cataract. *Biochem Biophys Res Commun* 2013;441:333-338.
107. Varadaraj K, Kumari SS, Patil R, Wax MB, Mathias RT. Functional characterization of a human aquaporin 0 mutation that leads to a congenital dominant lens cataract. *Exp Eye Res* 2008;87:9-21.
108. Senthil Kumar G, Kyle JW, Minogue PJ, et al. An MIP/AQP0 mutation with impaired trafficking and function underlies an autosomal dominant congenital lamellar cataract. *Exp Eye Res* 2013;Exp Eye Res:136-141.

109. Hu S, Wang B, Qi Y, Lin H. The Arg233Lys AQP0 mutation disturbs aquaporin0-calmodulin interaction causing polymorphic congenital cataract. *PLoS ONE* 2012;7:e37637.
110. Berry V, Francis P, Kaushal S, Moore A, Bhattacharya S. Missense mutations in MIP underlie autosomal dominant 'polymorphic' and lamellar cataracts linked to 12q. *Nat Genet* 2000;25:15-17.
111. Francis P, Berry V, Bhattacharya S, Moore A. Congenital progressive polymorphic cataract caused by a mutation in the major intrinsic protein of the lens, MIP (AQP0). *Br J Ophthalmol* 2000;84:1376-1379.
112. Geyer DD, Spence MA, Johannes M, et al. Novel single-base deletional mutation in major intrinsic protein (MIP) in autosomal dominant cataract. *American journal of ophthalmology* 2006;141:761-763.
113. Gu F, Zhai H, Li D, et al. A novel mutation in major intrinsic protein of the lens gene (MIP) underlies autosomal dominant cataract in a Chinese family. *Mol Vis* 2007;13:1651-1656.
114. Wang W, Jiang J, Zhu Y, et al. A novel mutation in the major intrinsic protein (MIP) associated with autosomal dominant congenital cataracts in a Chinese family. *Mol Vis* 2010;16:534-539.
115. Jiang J, Jin C, Wang W, et al. Identification of a novel splice-site mutation in MIP in a Chinese congenital cataract family. *Mol Vis* 2009;15:38-44.
116. Jin C, Jiang J, Wang W, Yao K. Identification of a MIP mutation that activates a cryptic acceptor splice site in the 3' untranslated region. *Mol Vis* 2010;16:2253-2258.
117. Shentu X, Miao Q, Tang X, Yin H, Zhao Y. Identification and Functional Analysis of a Novel MIP Gene Mutation Associated with Congenital Cataract in a Chinese Family. *PLoS ONE* 2015;10:e0126679.
118. Song Z, Wang L, Liu Y, Xiao W. A novel nonsense mutation in the MIP gene linked to congenital posterior polar cataracts in a Chinese family. *PLoS ONE* 2015;10:e0119296.
119. Wright PC, Noirel J, Ow SY, Fazeli A. A review of current proteomics technologies with a survey on their widespread use in reproductive biology investigations. *Theriogenology* 2012;77:738-765 e752.
120. Garland DL, Duglas-Tabor Y, Jimenez-Asensio J, Datiles MB, Magno B. The nucleus of the human lens: demonstration of a highly characteristic protein pattern by two-dimensional electrophoresis and introduction of a new method of lens dissection. *Exp Eye Res* 1996;62:285-291.
121. Schey KL, Anderson DM, Rose KL. Spatially-directed protein identification from tissue sections by top-down LC-MS/MS with electron transfer dissociation. *Anal Chem* 2013;85:6767-6774.

122. Harris GA, Nicklay JJ, Caprioli RM. Localized *in situ* hydrogel-mediated protein digestion and extraction technique for on-tissue analysis. *Anal Chem* 2013;85:2717-2723.
123. Taverna D, Norris JL, Caprioli RM. Histology-directed microwave assisted enzymatic protein digestion for MALDI MS analysis of mammalian tissue. *Anal Chem* 2015;87:670-676.
124. Lewis JK, Wei J, Siuzdak G. Matrix-Assisted Laser Desorption/Ionization Mass Spectrometry in Peptide and Protein Analysis. In: Meyers RA (ed), *Encyclopedia of Analytical Chemistry*. Chichester John Wiley & Sons Ltd; 2000:5880-5894.
125. Tanaka K, Waki H, Ido Y, et al. Protein and polymer analyses up to  $m/z$  100 000 by laser ionization time-of-flight mass spectrometry. *Rapid Communications in Mass Spectrometry* 1988;2:151-153.
126. Karas M, Hillenkamp F. Laser desorption ionization of proteins with molecular masses exceeding 10,000 daltons. *Anal Chem* 1988;60:2299-2301.
127. Caprioli RM, Farmer TB, Gile J. Molecular imaging of biological samples: localization of peptides and proteins using MALDI-TOF MS. *Anal Chem* 1997;69:4751-4760.
128. Seeley EH, Caprioli RM. MALDI imaging mass spectrometry of human tissue: method challenges and clinical perspectives. *Trends Biotechnol* 2011;29:136-143.
129. Seeley EH, Oppenheimer SR, Mi D, Chaurand P, Caprioli RM. Enhancement of protein sensitivity for MALDI imaging mass spectrometry after chemical treatment of tissue sections. *J Am Soc Mass Spectrom* 2008;19:1069-1077.
130. Angel PM, Spraggins JM, Baldwin HS, Caprioli R. Enhanced sensitivity for high spatial resolution lipid analysis by negative ion mode matrix assisted laser desorption ionization imaging mass spectrometry. *Anal Chem* 2012;84:1557-1564.
131. Grey AC, Chaurand P, Caprioli RM, Schey KL. MALDI imaging mass spectrometry of integral membrane proteins from ocular lens and retinal tissue. *J Proteome Res* 2009;8:3278-3283.

## **Chapter II – MALDI Imaging Mass Spectrometry Spatially Maps Age-Related Deamidation and Truncation of Human Lens Aquaporin-0**

**Adapted with permission from** Wenke JL, Rose KL, Spraggins JM, Schey KL. MALDI Imaging Mass Spectrometry Spatially Maps Age-Related Deamidation and Truncation of Human Lens Aquaporin-0. *Invest Ophthalmol Vis Sci* 2015;56:7398-7405.<sup>1</sup> © ARVO

### **Summary**

Spatially-resolved proteomics is a valuable tool for studying age-related protein changes across the lens. Here, we employed MALDI imaging mass spectrometry (MALDI IMS) to map modified forms of AQP0 across a wide age range of human lenses, from 2 months to 63 years. Our results confirm published data, showing a half-life of approximately 24 years for AQP0 truncation. Furthermore, we detected lipid-modified AQP0 in lens as young as 2 months and showed this lipid-modified AQP0 becomes truncated in older fiber cells, suggesting the lipid modification is irreversible. Finally, we used *in situ* digestion to generate spatially-localized tryptic peptides of AQP0, enabling high mass resolution imaging of deamidated AQP0 peptides. Distinct localization of differentially deamidated and truncated species was observed. These results show rapid and progressive deamidation within young outer cortical fiber cells, followed by truncation at the labile N/D sites. Microextraction of peptides followed by LC-MS/MS analysis was used to confirm the identification of peptides observed in imaging experiments and the predominant sites of deamidation. Our results are the first to image deamidation in human lens tissue, supporting a non-enzymatic mechanism for truncation that involves deamidation and isomerization of asparagine residues to (iso)-aspartic acid. Taken together, this study provides additional clues on the time course of several different modifications that may affect protein, and thus lens, function over time.

## Overview

The most abundant lens membrane protein is aquaporin-0 (AQP0), once known as the lens major intrinsic protein (MIP) or MP26. AQP0 is considered a dual-function water channel and adhesion molecule comprising ~50% of lens membrane protein.<sup>2</sup> The central pore of each AQP0 tetramer shuttles water across the plasma membrane.<sup>3</sup> AQP0 is also involved in junction formation and cell-to-cell adhesion.<sup>4-10</sup> Mutations or loss of AQP0 lead to cataract, highlighting the importance of this protein for lens function.<sup>11-22</sup>

AQP0 is a 28kD protein comprised of six transmembrane domains and an intracellular C-terminal tail. The highly modified tail regulates AQP0 permeability via calmodulin binding.<sup>23-25</sup> This region of AQP0 also binds cytoskeletal proteins including filensin, phakinin, and ezrin<sup>26, 27</sup> and may play a role in establishing fiber cell organization. Numerous PTMs decorate the AQP0 C-terminus over time, some of which have been functionally characterized. Phosphorylation of Ser-235 reduces the binding affinity of calmodulin, thereby boosting the permeability of the channel.<sup>25, 28, 29</sup> Cleavage of the C-terminal tail removes protein-protein binding regions and may encourage AQP0 to form cell-cell junctions.<sup>7, 30</sup> More recently, fatty acid modifications were discovered on lysine 238 and on the N-terminal methionine, which may target the protein to detergent-resistant lipid raft regions of the membrane.<sup>31, 32</sup> Deamidation and isomerization of asparagine residues have been reported but have not been fully characterized.<sup>33, 34</sup> The localization of these PTMs within the lens can provide clues of the changing physiological role of AQP0 over time.

MALDI mass spectrometry (MS) has been used to examine the spatial localization of modified proteins within the lens, including AQP0. Matrix is applied to the sample, assisting with desorption and ionization of the protein analyte to produce a mass spectrum. Each distinct

protein produces a unique mass-to-charge ( $m/z$ ) signal, enabling the detection of many different species in one experiment. Protein modifications are characterized by specific shifts in  $m/z$  values. MALDI MS is compatible with endogenous protein analysis, with no requirement for enzymatic digestion prior to analysis. Data analysis is also straightforward, as most analytes are singly charged in the MALDI spectrum. In initial studies, regions of human lens were dissected into concentric rings, digested with cyanogen bromide to generate a C-terminal peptide of AQP0, and mixed with matrix on a target plate for MALDI analysis.<sup>35</sup> MALDI technology can also be used in profiling mode, where discrete spots of matrix are spotted directly on a thin human tissue section to target regions of interest.<sup>34</sup> Unique modifications, including fatty acid acylation and phosphorylation, have been discovered and spatially characterized using this method.<sup>31, 32</sup>

MALDI imaging mass spectrometry (IMS) has also been used to map modified AQP0 in the lens.<sup>31, 36</sup> In MALDI IMS,  $m/z$  values are mapped across a tissue section with intensity encoded as a heat map to generate an image for each distinct  $m/z$  signal across the lens at a spatial resolution of 200-300 $\mu\text{m}$ .<sup>37</sup> MALDI ion images are overlaid on an optical image of the tissue section, enabling comparison of analyte distribution based on tissue region. MALDI IMS is performed directly from the tissue section, making it advantageous over traditional ESI LC-MS/MS because spatial information is retained for each analyte. Previous MALDI imaging experiments revealed the localization of truncated and lipid-modified AQP0 in bovine and human lenses.<sup>31, 38</sup> Although informative, these molecular images captured a single timepoint in the complex aging process. Furthermore, the spatial distribution and accumulation of other modified forms of AQP0, including deamidated AQP0, have not been reported.

The aim of this study was to characterize the localization of modified AQP0 in human lens from birth through middle age using MALDI IMS. We optimized methods to image

modified AQP0, revealing unprecedented images of deamidated and truncated forms of the functionally-important AQP0 C-terminal tail. Understanding the localization of these modifications in young or old fiber cells can provide clues on how AQP0 function changes during development, aging, and cataract formation.

## Experimental Methods

### *Materials*

Proteomics-grade porcine trypsin, methanol, high-performance liquid chromatography (HPLC)-grade acetonitrile, formic acid, sinapinic acid, and  $\alpha$ -cyano-4-hydroxycinnamic acid (CHCA) were purchased from Sigma-Aldrich (St. Louis, MO). Acetic acid, ammonium bicarbonate, and Triton X-100 were from Fisher Scientific (Pittsburgh, PA). Gold-coated MALDI targets were from AB Sciex (Framingham, MA). Frozen human lenses were obtained from the National Disease Research Interchange (Philadelphia, PA) and stored at -80°C until further use. Lenses used in this study were from individuals with no reported ocular pathology. Eight lenses were analyzed in total: 2 month (male, M), 4 month (female, F), 21 year (M), 23 year (F), 39 year (M), 47 year (M), 56 year (M), and 63 year (F). All other reagents were purchased from Sigma-Aldrich unless otherwise stated.

### *Tissue Preparation*

Methods were initially optimized on bovine lenses. Frozen lenses were sectioned to 20 $\mu$ m thickness using a CM 3050 Cryostat (Leica Microsystems, Bannockburn, IL, USA). Sections were transferred to gold-coated MALDI target plates via methanol soft landing.<sup>36</sup> Using a modified protocol,<sup>36</sup> sections were pipette washed with ddH<sub>2</sub>O for 1 minute, followed by

desiccation to dryness after each wash. After ten water washes, sections were washed three times with 1% formic acid (1 minute), with 30 second water washes in between. Sections were desiccated prior to matrix application.

#### *MALDI IMS of Lens Membrane Protein AQP0*

Matrix was applied using a Portrait Spotter (Labcyte, Sunnyvale, CA). Arrays of matrix droplets were placed with 400 $\mu$ m spacing and were interleaved for a final droplet spacing of 200 $\mu$ m. Sinapinic acid matrix (20mg/mL in 70:29.7:0.3 ACN:H<sub>2</sub>O:TFA with 0.025% Triton-X 100) was spotted, one droplet per pass, for a total of 40 droplets per spot.

MALDI protein imaging data were collected on a Bruker Autoflex Speed II TOF instrument (Bruker Daltonics, Billerica, MA). External calibration was performed using a protein standard mix (equine cytochrome C, equine apomyoglobin, bovine trypsinogen, and rabbit carbonic anhydrase) prior to data collection. Methods were established in FlexControl software (1 kHz laser, medium spot size laser, 350 ns pulsed ion extraction, *m/z* 17,000-35,000, 300 laser shots per spot) and images were viewed in FlexImaging software. For images shown, all four human lens sections (4 month, 21 year, 39 year, 56 year) were imaged on one plate, in one data file, and normalized via total ion current (TIC).<sup>39</sup> TIC normalization calculates the normalized peak intensity for each spectral feature (peak) by dividing its intensity by the total ion current in each mass spectrum across an entire imaging data set, in this case across four lens images. Ion intensities are then displayed across the image by assigning the largest normalized signal for each *m/z* to a value of 100% and the lowest normalized signal as 0%. Therefore, each ion image is calculated independently from other ion images. For display purposes, data were interpolated and pixel intensities were rescaled using “brightness optimization” in FlexImaging software.

This feature optimizes the brightness of each individual signal to utilize the entire dynamic range, as indicated by the color scale bars. The integrated intensity for each  $m/z$  signal ( $\pm 0.3\%$   $m/z$  units) was plotted as a normalized TIC value. A total of three technical replicates were run to ensure reproducibility of molecular patterns. Triplicate images were also acquired from a second sample set including 2 month, 23 year, 47 year, and 63 year lenses.

#### *In Situ Digestion and MALDI IMS of AQP0 Tryptic Peptides*

For peptide imaging, lens sections were washed with water and 1% formic acid as described above and sprayed with trypsin (0.04 $\mu$ g/ $\mu$ L in 100mM ammonium bicarbonate, pH 8, with 10% ACN). Trypsin was applied in 8 passes by a TM Sprayer (HTX Technologies, Carrboro, NC, USA) modified with a syringe pump at 7.5 $\mu$ l/minute (Harvard Apparatus, Holliston, MA). Digestion was carried out in a humidified petri dish at 37°C with 0.2mL ammonium bicarbonate for 2 hours. Incubation conditions were optimized to minimize delocalization and no drying was required prior to matrix application. CHCA matrix was applied in 4 passes using the TM sprayer (5mg/mL CHCA in 50:49.7:0.3 ACN:H<sub>2</sub>O:TFA, 700mm/minute velocity, 2mm track spacing).

Peptide imaging data were collected on a Bruker SolariX 15T FTICR MS (Bruker Daltonics, Billerica, MA). Images over the entire peptide mass range ( $m/z$  600-10,000) were collected with 1000 laser shots per pixel with a raster step size of 100  $\mu$ m. Images were acquired using a Smartbeam II 2kHz Nd:YAG (355nm) laser using the small laser setting (estimated spot size ~60  $\mu$ m). Continuous accumulation of selected ions (CASI)<sup>40</sup> imaging was also used to achieve better sensitivity for low-abundance species. For CASI images, a narrow mass range around the signal of interest (1475-3000 for  $m/z$  2550) was selected with a Q1 mass of 2555 and

an isolation window of  $m/z$  20. An ICR transient length of 3.35 seconds was used to achieve a resolving power of 250,000 at  $m/z$  2550. The raster step size was 125  $\mu\text{m}$ ; 5000 laser shots were acquired per pixel. Ion images were generated in Bruker FlexImaging software. Full mass range data were normalized by TIC and each  $m/z$  signal was plotted  $\pm 0.005$   $m/z$  units.

#### *Microextraction and nanoLC-MS/MS Analysis for Peptide Identification*

Serial lens sections were washed and sprayed with trypsin as described above. Spatially-directed extraction of tryptic peptides was accomplished as described by Schey et al.<sup>41</sup> Extracts were collected from the outer and inner cortex of four lenses (4 month, 21 year, 39 year, and 56 year). Using a gel-loading pipet tip, one microliter solvent (20% ACN with 0.1% formic acid, HPLC-grade) was pipetted onto a lens region, aspirated repeatedly, and collected. This microextraction procedure was repeated, and the pooled peptide extract was diluted ten-fold with the same solvent. Half of the extract was bomb-loaded onto a reverse-phase 360 $\mu\text{m}$  outer diameter (o.d.) x 150 $\mu\text{m}$  inner diameter (i.d.) capillary trap column (3cm length/5 $\mu\text{m}$  Jupiter C18 beads, 300 $\text{\AA}$ , Phenomenex) in-line with a 360 $\mu\text{m}$  o.d. x 100 $\mu\text{m}$  i.d. reverse-phase analytical column equipped with a laser-pulled emitter tip and packed with 20cm of Jupiter C18 beads (3 $\mu\text{m}$ , 300 $\text{\AA}$ , Phenomenex). Using an Eksigent nanoHPLC, peptides were eluted at a flow rate of 500 nL/min over a 90-minute gradient of 0.1% formic acid in water (solvent A) and 0.1% formic acid in acetonitrile (solvent B). The gradient consisted of 2-40 %B in 64 minutes, 40-90 %B in 8 minutes, 90 %B for 2 minutes, followed by equilibration at 2 %B. Gradient-eluted peptides were mass analyzed on an LTQ Orbitrap Velos mass spectrometer with a nanoelectrospray ionization source (Thermo Scientific, San Jose, CA). The instrument was operated using a data-dependent method. Full scan ( $m/z$  300-2000) spectra were acquired with the Orbitrap (resolution 60,000)

using an MS<sup>1</sup> AGC target value of 1 x 10<sup>6</sup> with 100ms maximum injection time. Dynamic exclusion settings allowed for a repeat count of 1 within a repeat duration of 10sec, and the exclusion duration time was set to 15sec. The top 16 most abundant ions in each MS scan were selected for fragmentation via collision-induced dissociation (CID) in the LTQ. An isolation width of 2 *m/z*, activation time of 10 ms, and 35% normalized collision energy were used to generate MS<sup>2</sup> spectra. Tandem mass spectra were acquired using an MS<sup>2</sup> AGC target value of 1 x 10<sup>4</sup> with 100ms maximum injection time. An average of 30,000 MS<sup>2</sup> spectra were generated from each 90-minute run. For selected LC-MS/MS analyses, the LTQ Orbitrap Velos was operated using a method consisting of targeted scan events, for which specific *m/z* values corresponding to AQP0 peptides were provided in the data acquisition method to facilitate collection of targeted MS/MS spectra despite the low intensity of peptide precursors. Spectra acquired of AQP0 peptides of interest, including those with non-tryptic termini, were inspected using Xcalibur 3.0.63 Qual Browser software (Thermo Scientific). For manual peptide assignment, MS/MS spectra with a precursor mass within 5ppm of the calculated mass were compared to theoretical b- and y- ions. Other considerations included overall signal intensity, good coverage of the entire peptide sequence including modified residue(s), labeling of a majority of fragmentation ions, and few unattributed peaks of high intensity. For additional peptide identification, tandem mass spectra were converted into DTA files using Scansifter and searched using a custom version of Sequest (Thermo Fisher Scientific) operating on the Vanderbilt ACCRE computing cluster. MS/MS spectra were searched against a concatenated forward and reverse (decoy) database containing the *Homo sapiens* subset of UniprotKB Sprot protein database (20,360 proteins, [www.uniprot.org](http://www.uniprot.org)). Additional search parameters included: trypsin enzyme specificity, monoisotopic masses were used for searching product ions, and

oxidation of methionine and phosphorylation of serine, threonine and tyrosine were allowed as variable modifications. Scaffold 4.3.4 (Proteome Software, Portland, OR, USA) was used to summarize and validate search results, where a minimum probability threshold of 95% was required for peptide identifications and data were filtered to a false-discovery rate (FDR) of <1% at the protein level. Peptide signals from MALDI IMS (acquired on the FTICR instrument) and LC-MS/MS (acquired on the Orbitrap instrument) experiments were matched by accurate mass (<5ppm error required) to identify peptides from imaging experiments.

#### *nanoLC-MS/MS Gradient Optimization for Deamidated Species Separation*

To achieve better separation of deamidated peptide species, which differ by one or two asparagine residues converted to aspartic acid, the linear gradient in the peptide elution range was modified from 0.75% B/minute to 0.3% B/minute. This shallow gradient provided better chromatographic separation of differentially deamidated peptides, enabling quantification of each peptide. The gradient consisted of 2%-10% B in 18 minutes, followed by 10%-26% B in 16 minutes, up to 35% B in 9 minutes, 90% B for 1 minute, and equilibration at 2% B. The instrument was operated using both data-dependent and targeted scan events; high-resolution MS<sup>2</sup> data was acquired for AQP0 peptides of interest to definitively assign deamidation sites. Peptide abundance was calculated by extracted ion chromatogram peak area with a tolerance of 8ppm.

#### *Lens Homogenization and LC-MS/MS for Identifying Lipid-Modified Peptides*

Lipid modification of AQP0 C-terminal peptide in a 4 month-old lens was confirmed by LC-MS/MS, using a modified protocol due to the hydrophobic nature of fatty acid acylated

peptides.<sup>31</sup> Shavings from cryosectioning were collected in an Eppendorf tube and membranes were separated as follows. Tissue was manually homogenized with a Teflon homogenizer using buffer (50 mM ambic, 5mM EDTA, 10mM NaF, 1mM DTT, pH 8) and spun at 100,000xg for 30 minutes. After discarding the supernatant, the pellet was resuspended in 8M urea in buffer, then spun at 100,000xg for 30 minutes. This procedure was repeated, followed by washes with water, 0.1M NaOH, and water (x3) with centrifuging and supernatant removal between each step. Pellets were reduced and alkylated, then digested in 10% ACN/90% 50mM ammonium bicarbonate. The digested pellet was dried down and soluble peptides were extracted using 0.1% formic acid and transferred to a separate tube. The remaining pellet was then extracted with 100% ACN to extract more hydrophobic peptides, and this mixture was transferred, dried down, and peptides reconstituted with 5% ACN/0.1% formic acid before analysis by LC-MS/MS as described above.

#### *Multiple-Charging for Intact AQP0 Analysis by FTICR MS*

Our strategy for identifying modified forms of AQP0 has been to enzymatically digest the protein into smaller peptides that can be sequenced by tandem mass spectrometry. While this approach is generally successful, it is difficult to know whether the most abundant species detected by LC-MS/MS are the same as those detected by MALDI MS. Furthermore, the fatty acid acylated forms of AQP0 detected in MALDI TOF imaging experiments are likely a mixture of palmitic acid- and oleic acid-modified AQP0; at 28kDa, these additions (+238 and +264 *m/z*) cannot be resolved. Thus, we developed a strategy to obtain high-resolution FTICR MS data for intact AQP0. A thin human lens tissue section was methanol soft-landed and washed as described above to remove soluble proteins. A specific matrix, 2- nitrophloroglucinol (2-NPG),

was hand-spotted onto the tissue section in several regions in the outer and inner cortex. This matrix is reported to enhance multiple charging in MALDI experiments,<sup>42</sup> which would enable detection of the 28kDa AQP0 protein by FTICR MS. Tissue was analyzed in MALDI profiling mode on a Bruker SolariX 15T FTICR using an expanded mass range (*m/z* 1,000-18,000).

## Results

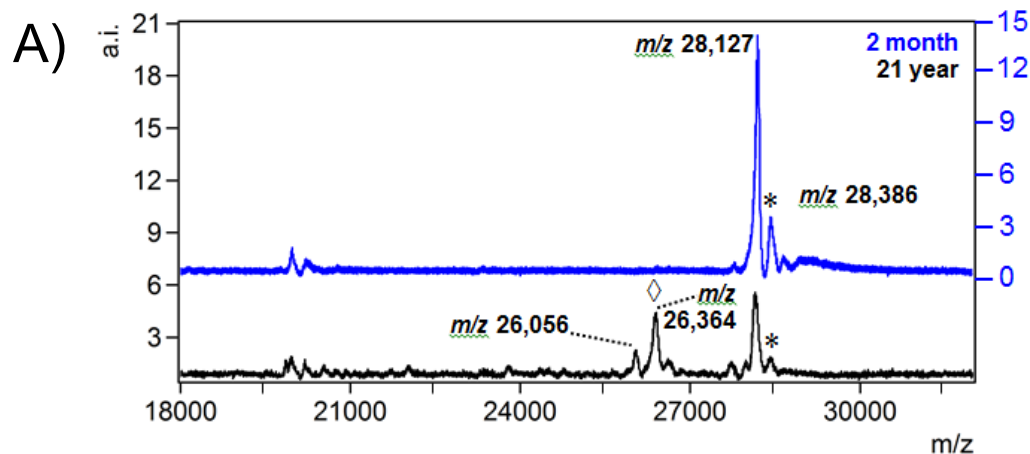
### *MALDI IMS of Lens Membrane Protein AQP0*

MALDI images of endogenous protein were acquired from young and older human lenses to spatially map age-related processing of AQP0. The procedure of Grey *et al* was modified by adding a series of 1% formic acid washes to remove soluble crystallins in order to facilitate AQP0 imaging.<sup>36, 43</sup> The matrix solution was also optimized to include 70% ACN with 0.025% Triton X-100 detergent. This matrix solution generated uniform spots and provided excellent extraction and co-crystallization of AQP0 with matrix.

We imaged 4 lenses in one experiment, ranging from 0-63 years, which allowed a direct comparison of protein changes within each lens core (a region that is formed during embryonic development and contains cells as old as the individual) and within each lens cortex (which contains newly-differentiated cells). We display both rainbow-scale images, which illustrate the changing intensity of one ion, and false-colored overlays, which allow comparison and visualization of multiple signals. Protein imaging revealed fatty acid acylated and truncated AQP0 patterns. *In situ* digestion and MALDI IMS enabled unprecedented imaging of deamidated AQP0 peptides. Together with LC-MS/MS, these data reveal time-dependent deamidation as it relates to truncation in the human lens.

Representative mass spectra from two human lenses highlight the accumulation of truncated AQP0 with age (Figure 2.1). Full-length AQP0 1-263 ( $m/z$  28,127  $\pm$  0.3%) is abundant in the 2 month lens and very few soluble crystallin protein signals (19-23kDa) are present due to extensive tissue washing. Fatty acid acylated AQP0 is also observed ( $m/z$  28,386  $\pm$  0.15%). In a 21 year-old lens, full-length AQP0 signal decreases, while lower  $m/z$  signals appear due to C-terminal cleavage. Truncated AQP0 corresponding to 1-259 ( $m/z$  27,704  $\pm$  0.15%), 1-246 ( $m/z$  26,364  $\pm$  0.3%), and 1-243 ( $m/z$  26,056  $\pm$  0.15%) could be detected in all lenses except 2 month and 4 month. Ion images reveal that AQP0 1-263 is present throughout the 4 month lens but only in the very outer cortex of the older lenses (Figures 2.2A and 2.3A). In the older lens cores, major C-terminal cleavage products are abundant (Figures 2.2B-D). In agreement with previous reports, truncation at residue 259 is most intense in the outer cortex, while truncated products 1-246 and 1-243 are most abundant in the central core. The absence of signal from the 56 year lens core is likely due to further truncation and other post-translational modifications, resulting in a heterogeneous population of AQP0 forms. MALDI IMS experiments were repeated on another set of human lenses, ranging from 2 months to 63 years, and the observed truncation patterns are very similar to these results (data not shown).

**Figure 2.1**



B)

[M+H] <sup>+</sup> of Human Lens AQP0		
	Theoretical <i>m/z</i>	Observed <i>m/z</i>
1-263	28,123	28,127
1-263 + oleic acid	28,387	28,386
1-259	27,709	27,704
1-246	26,359	26,364
1-246 + oleic acid	26,623	26,623
1-243	26,059	26,056

**Figure 2.1.** Representative MALDI-TOF Spectra from 2-Month and 21-Year Human Lens. (A) The major signal in the 2 month lens is full-length AQP0 1-263. Lipid-modified AQP0 (\*) is present in both lenses, while major truncation peaks (◊) are only apparent in the 21 year lens. Spectra were generated from regions of interest including the cortex and core of each lens. (B) Theoretical and observed *m/z* values for modified forms of AQP0. Putative identifications listed are based on accurate mass and previous publications.<sup>36</sup> a.i.= arbitrary intensity

**Reprinted with permission from** Wenke JL, Rose KL, Spraggins JM, Schey KL. MALDI Imaging Mass Spectrometry Spatially Maps Age-Related Deamidation and Truncation of Human Lens Aquaporin-0. *Invest Ophthalmol Vis Sci* 2015;56:7398-7405. © ARVO

**Figure 2.2**

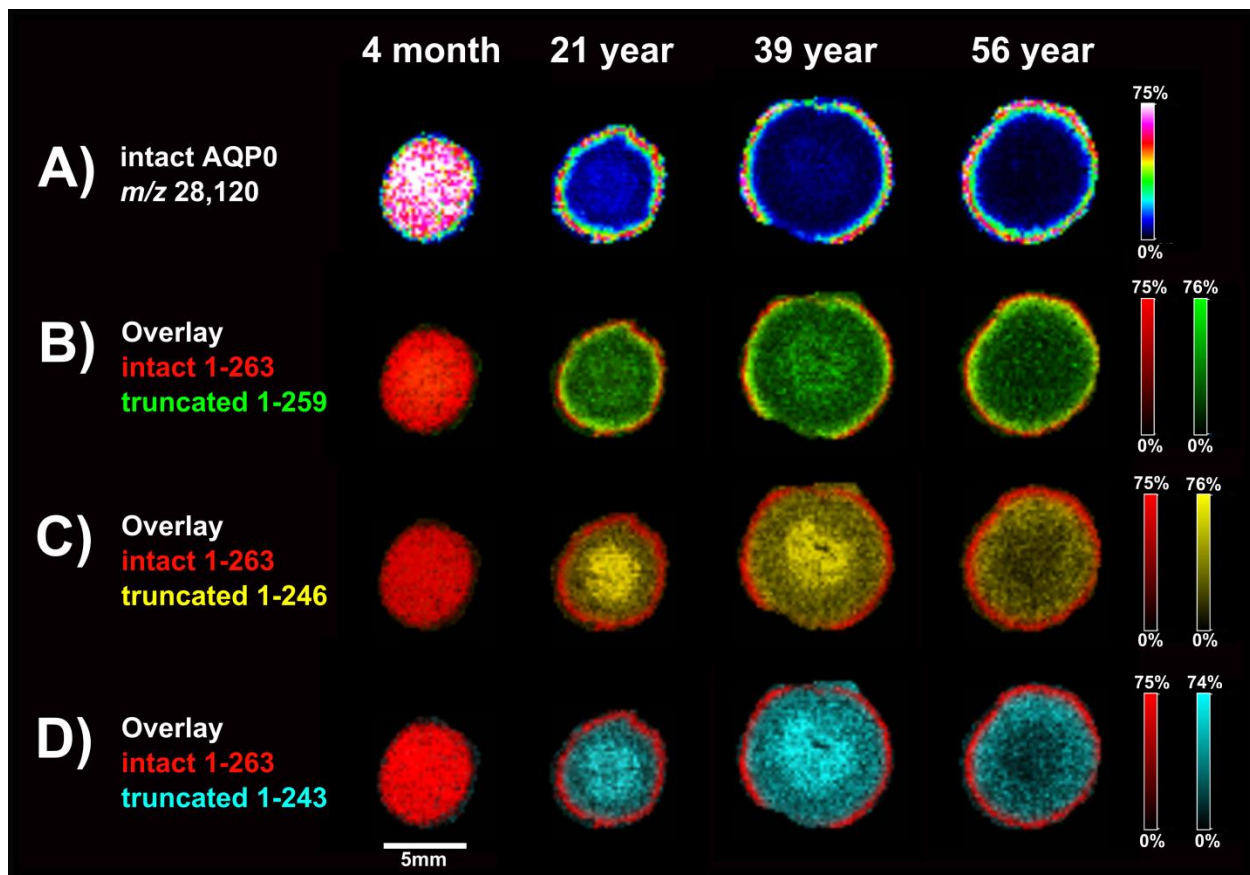


**Figure 2.2.** AQP0 Protein Imaging Demonstrates Age-Related Truncation (Overlays). (A) Full-length AQP0 1-263 signal is lost due to extensive C-terminal truncation in older lens cores. Accumulation of 1-259 (B), 1-246 (C), and 1-243 (D) truncated AQP0 is apparent in older lens cores. Images were acquired with 200 $\mu$ m raster step size on a Bruker Autoflex TOF. Ion intensities are normalized to the TIC for each ion across the tissue section and color scale bars indicate the range of intensities plotted.

**Reprinted with permission from** Wenke JL, Rose KL, Spraggins JM, Schey KL. MALDI Imaging Mass Spectrometry Spatially Maps Age-Related Deamidation and Truncation of Human Lens Aquaporin-0. *Invest Ophthalmol Vis Sci* 2015;56:7398-7405. © ARVO

**Figure 2.3**

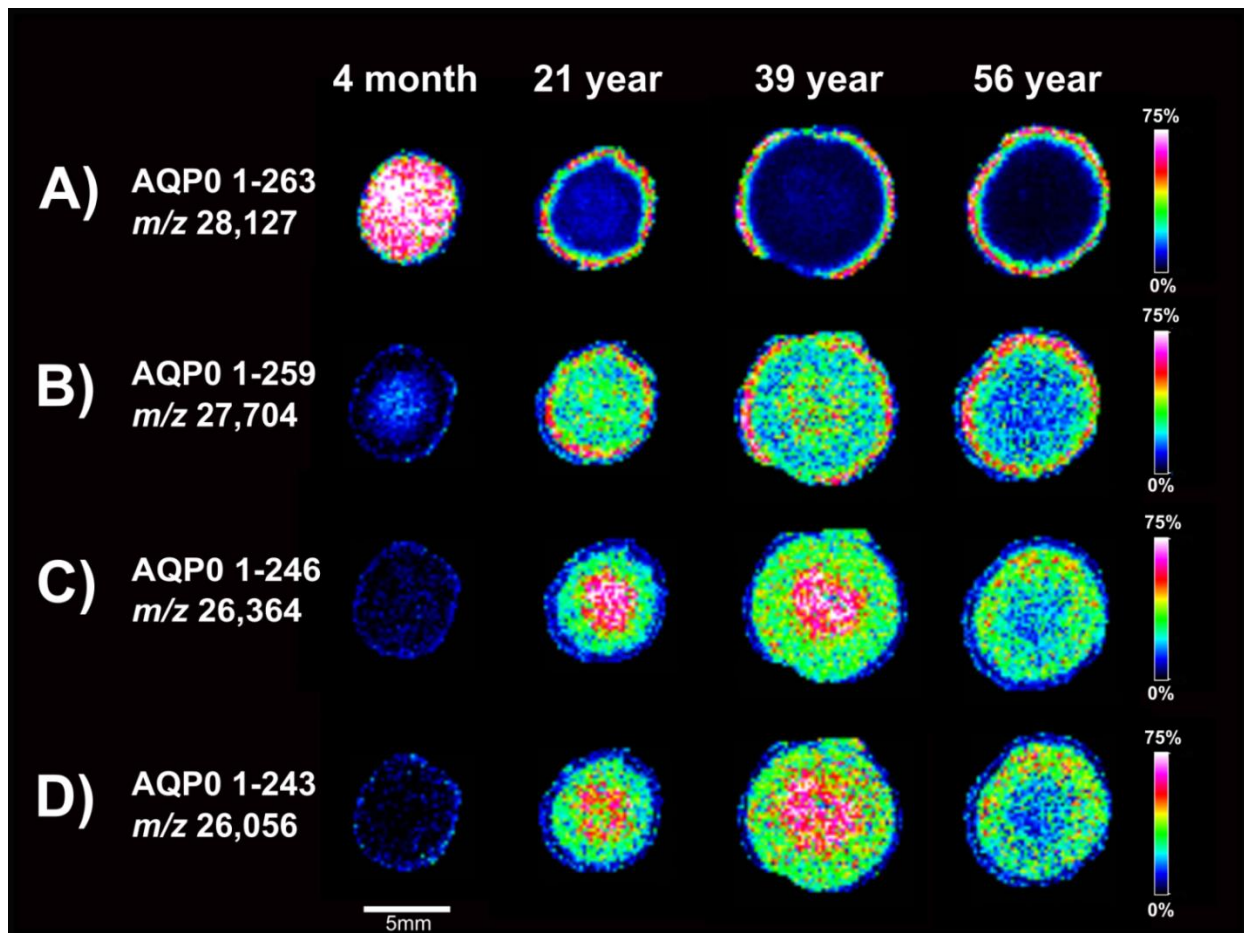


**Figure 2.3.** AQP0 Protein Umaging Demonstrates Age-Related Truncation. Individual ion images for truncated forms of AQP0 are shown. Images were acquired with 200 $\mu$ m raster step size on a Bruker Autoflex TOF. Ion intensities are normalized to the TIC for each ion across the tissue section and rainbow scale bars indicate the range of intensities plotted.

**Reprinted with permission from** Wenke JL, Rose KL, Spraggins JM, Schey KL. MALDI Imaging Mass Spectrometry Spatially Maps Age-Related Deamidation and Truncation of Human Lens Aquaporin-0. *Invest Ophthalmol Vis Sci* 2015;56:7398-7405. © ARVO

Fatty acid acylated AQP0 was detected in all lenses (Figures 2.4 and 2.5). In the 4 month lens, full-length, fatty acid acylated AQP0 was present in the lens cortex and core. This finding represents the youngest lens reported to contain lipid-modified AQP0 and suggests that AQP0 lipidation is an early processing event. MS/MS spectra indicate both oleic acid and palmitic acid are present on the N-terminal methionine in the 4 month lens (Figure 2.6). Older lenses contained both full-length (1-263 + lipid) and truncated acylated AQP0 (1-246 + lipid), depending on fiber cell age. The lipid modification detected by MALDI is observed as a fairly broad peak, likely containing a combination of oleic acid (C18:1, +264 Da) and palmitic acid (C16:0, +238 Da) as previously reported<sup>31</sup> and other less abundant lipid modifications (unpublished).

**Figure 2.4**

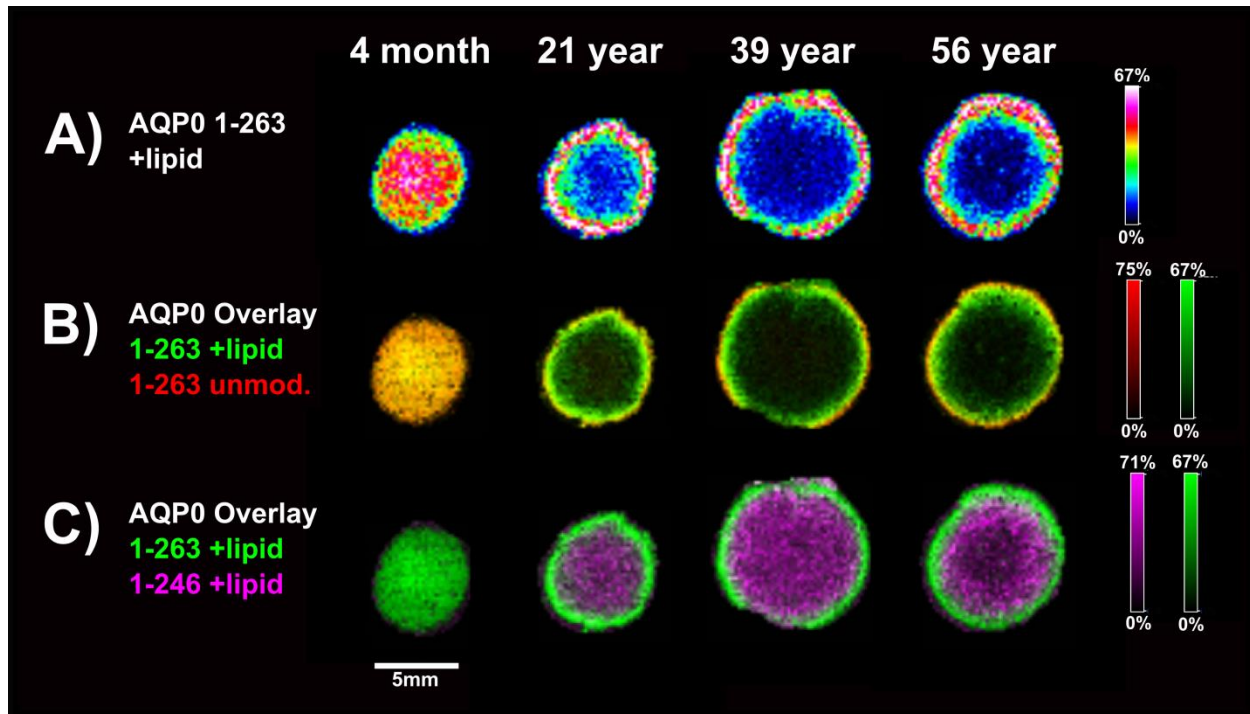


**Figure 2.4.** Fatty Acid Acylated AQP0 Protein Overlays.

AQP0 is modified with a fatty acid in young fiber cells (A), with a narrow ring of unmodified AQP0 before the lipid is added (B). The fatty acylated form is also C-terminally truncated, predominantly at residue 246 (C). Images were acquired with 200 $\mu$ m raster step size on a Bruker Autoflex TOF. Ion intensities are normalized to the TIC for each ion across the tissue section and color scale bars indicate the range of intensities plotted.

**Reprinted with permission from** Wenke JL, Rose KL, Spraggins JM, Schey KL. MALDI Imaging Mass Spectrometry Spatially Maps Age-Related Deamidation and Truncation of Human Lens Aquaporin-0. *Invest Ophthalmol Vis Sci* 2015;56:7398-7405. © ARVO

**Figure 2.5**

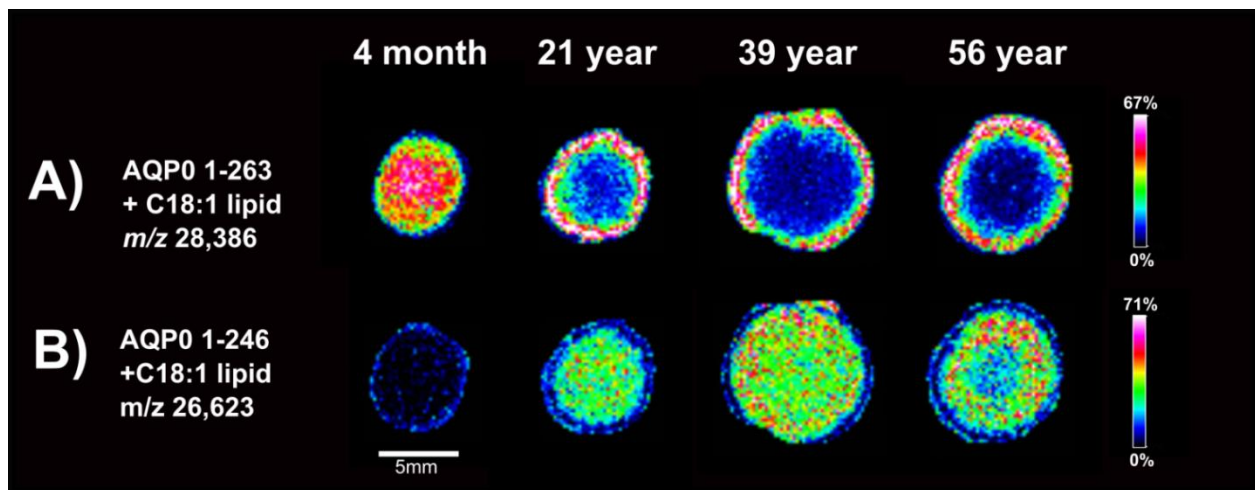


**Figure 2.5.** Fatty Acid Acylated AQP0 Protein.

Individual ion images for full-length and truncated fatty acid acylated AQP0 are shown. Images were acquired with 200 $\mu$ m raster step size on a Bruker Autoflex TOF. Ion intensities are normalized to the TIC for each ion across the tissue section and rainbow scale bars indicate the range of intensities plotted.

**Reprinted with permission from** Wenke JL, Rose KL, Spraggins JM, Schey KL. MALDI Imaging Mass Spectrometry Spatially Maps Age-Related Deamidation and Truncation of Human Lens Aquaporin-0. *Invest Ophthalmol Vis Sci* 2015;56:7398-7405. © ARVO

**Figure 2.6**

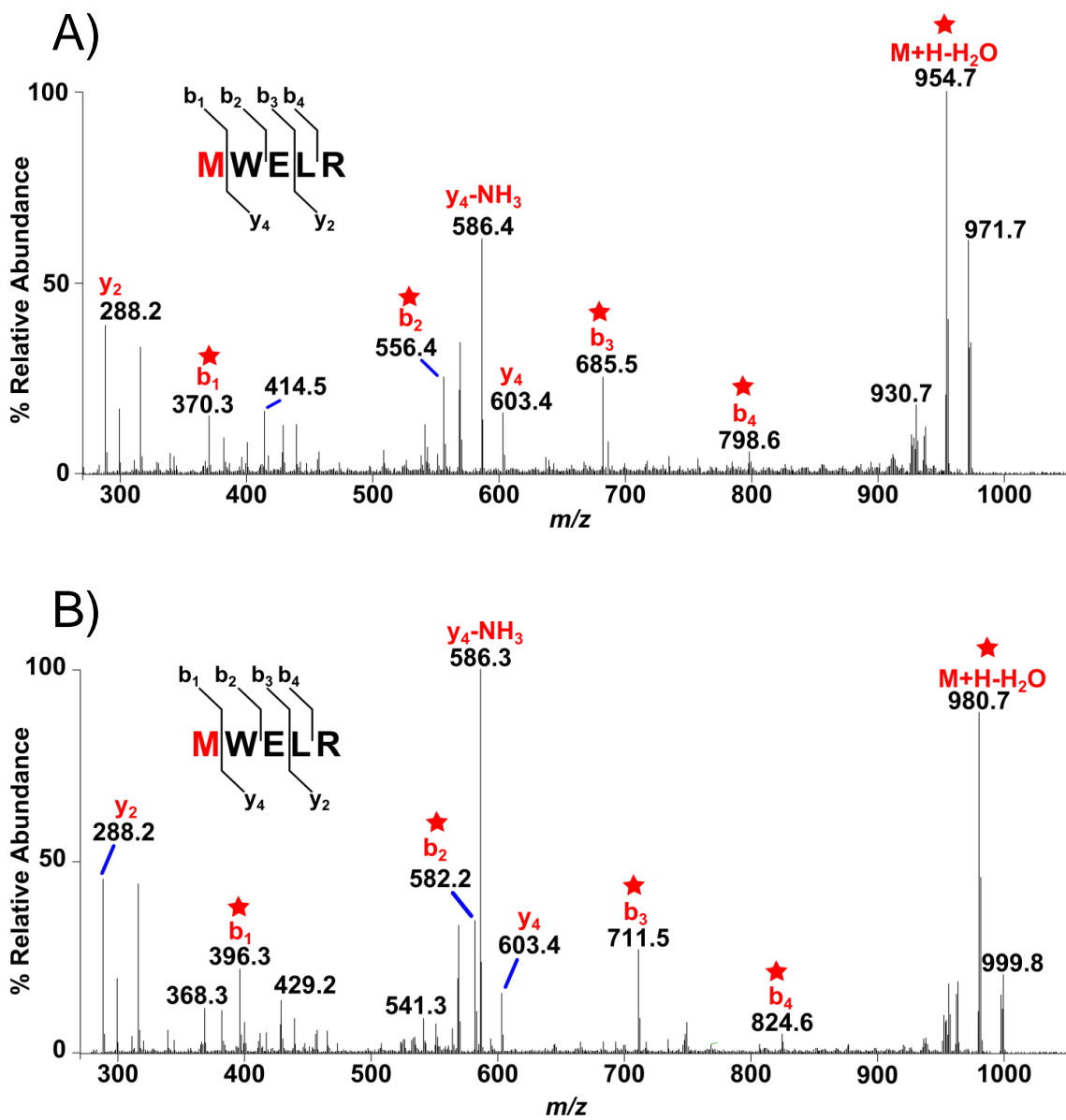


**Figure 2.6.** Tandem Mass Spectrum Confirming Lipid Modification of AQP0 in 4-Month Lens.

- A) CID spectrum of singly-charged AQP0 peptide 1-5,  $m/z$  972.6, with the addition of palmitic acid ( $m/z$  238).
- B) CID spectrum of singly-charged AQP0 peptide 1-5,  $m/z$  998.6, with the addition of oleic acid ( $m/z$  264).

**Reprinted with permission from** Wenke JL, Rose KL, Spraggins JM, Schey KL. MALDI Imaging Mass Spectrometry Spatially Maps Age-Related Deamidation and Truncation of Human Lens Aquaporin-0. *Invest Ophthalmol Vis Sci* 2015;56:7398-7405. © ARVO

### *In Situ Digestion and MALDI IMS of AQP0 Tryptic Peptides*

After extensive washing to remove soluble proteins, lens sections were digested with spray-coated trypsin to generate spatially-localized peptides that reflect endogenous protein distribution. Using a high mass resolution FTICR MS instrument operated in CASI mode, peptides were analyzed by MALDI IMS. CASI afforded increased sensitivity during high mass resolution (250,000) experiments, enabling resolution of isotopic clusters of deamidated and undeamidated AQP0 peptides. Measurement of mass defect was used to determine deamidation of AQP0 peptides, as shown for lens crystallins at the peptide level.<sup>44</sup>

The C-terminal tryptic peptide of AQP0 (239-263) can be deamidated at two asparagine residues, N246 and N259.<sup>33</sup> Figure 2.7B shows the CASI spectrum for this AQP0 peptide from a 4 month lens. The undeamidated 239-263 AQP0 peptide ( $m/z$  2550.274  $\pm$  0.005) was only detected in the outer cortex of a 4 month human lens with low intensity (Figure 2.7A). Singly- and doubly-deamidated AQP0 ( $m/z$  2551.257  $\pm$  0.005 and 2552.238  $\pm$  0.005, respectively) could be detected in this young lens, suggesting deamidation can occur early in developing humans. Note the observed isotopic distribution matches the predicted isotopic distribution at a mass resolving power of ~250,000. In older lenses, undeamidated AQP0 cannot be detected by MALDI, and the doubly-deamidated peptide is most abundant (Figures 2.8 and 2.9). Overlaid ion images show concentric rings of singly- and doubly-deamidated AQP0, while truncated AQP0 is localized more centrally in older lenses, suggesting deamidation precedes truncation. The loss of AQP0 239-259 signal in the center of lenses is likely due to further truncation, although we do not detect the major truncation fragment 239-243 because of its low mass. These unprecedented MALDI images acquired at 250,000 resolving power show early and progressive deamidation and truncation of AQP0.

**Figure 2.7**

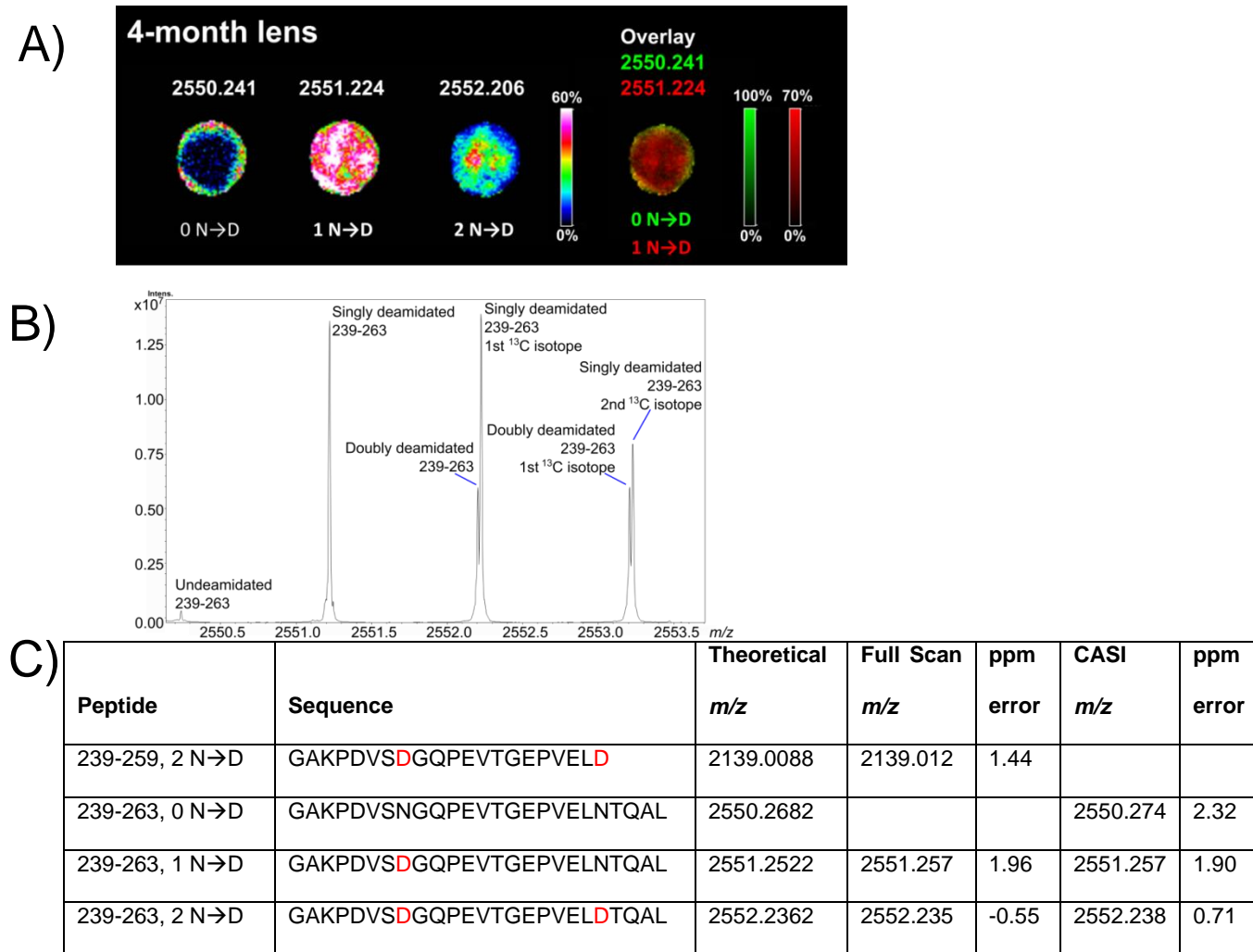


**Figure 2.7.** Deamidation of C-terminal AQP0 Peptide 239-263

(A) Undeaminated AQP0 is present in the very young outer cortical fiber cells of a 4 month lens. Deamidation is more abundant in the lens core. Images were acquired with 125 $\mu$ m raster step size using FTICR MS. All *m/z* values are plotted  $\pm$  0.005 *m/z*. Ion intensities are normalized to the TIC for each ion across the tissue section and color scale bars indicate the range of intensities plotted.

(B) CASI FTICR spectrum showing un-, singly- and doubly-deamidated AQP0 peptide.

(C) Calculated and experimental *m/z* values for AQP0 C-terminal peptide deamidation. Reported full scan and CASI *m/z* values were acquired on a Bruker SolariX 15T FTICR MS. Red “D” indicates sites of N→D conversion.

**Reprinted with permission from** Wenke JL, Rose KL, Spraggins JM, Schey KL. MALDI Imaging Mass Spectrometry Spatially Maps Age-Related Deamidation and Truncation of Human Lens Aquaporin-0. *Invest Ophthalmol Vis Sci* 2015;56:7398-7405. © ARVO

**Figure 2.8**

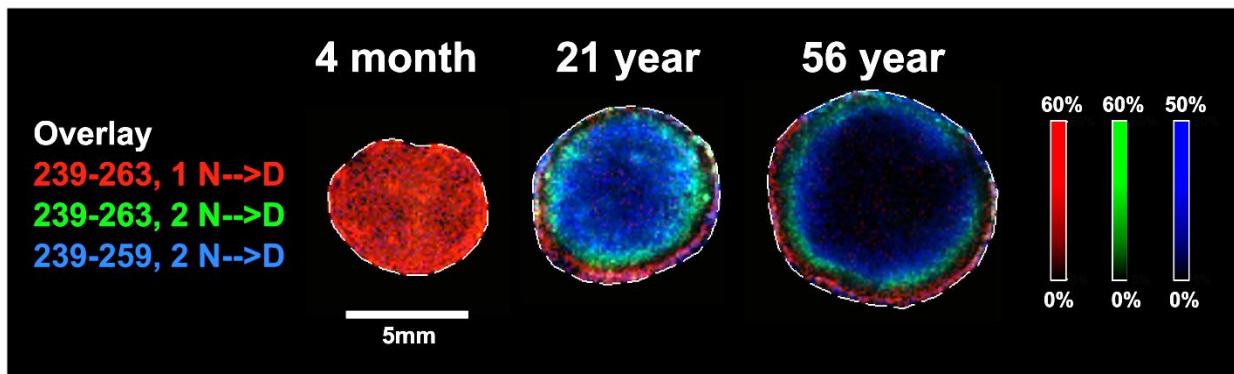


**Figure 2.8.** Age-related Accumulation of Deamidation and Truncation (Overlay). Singly- and doubly-deamidated AQP0 peptide are visible in concentric rings in older lenses. Slightly older fiber cells contain deamidated peptide that has been truncated at residue 259. Images were acquired with 100 $\mu$ m raster step size on a Bruker SolariX 15T FTICR MS. Ion intensities are normalized to the TIC for each ion across the tissue section and color scale bars indicate the range of intensities plotted.

**Reprinted with permission from** Wenke JL, Rose KL, Spraggins JM, Schey KL. MALDI Imaging Mass Spectrometry Spatially Maps Age-Related Deamidation and Truncation of Human Lens Aquaporin-0. *Invest Ophthalmol Vis Sci* 2015;56:7398-7405. © ARVO

**Figure 2.9**

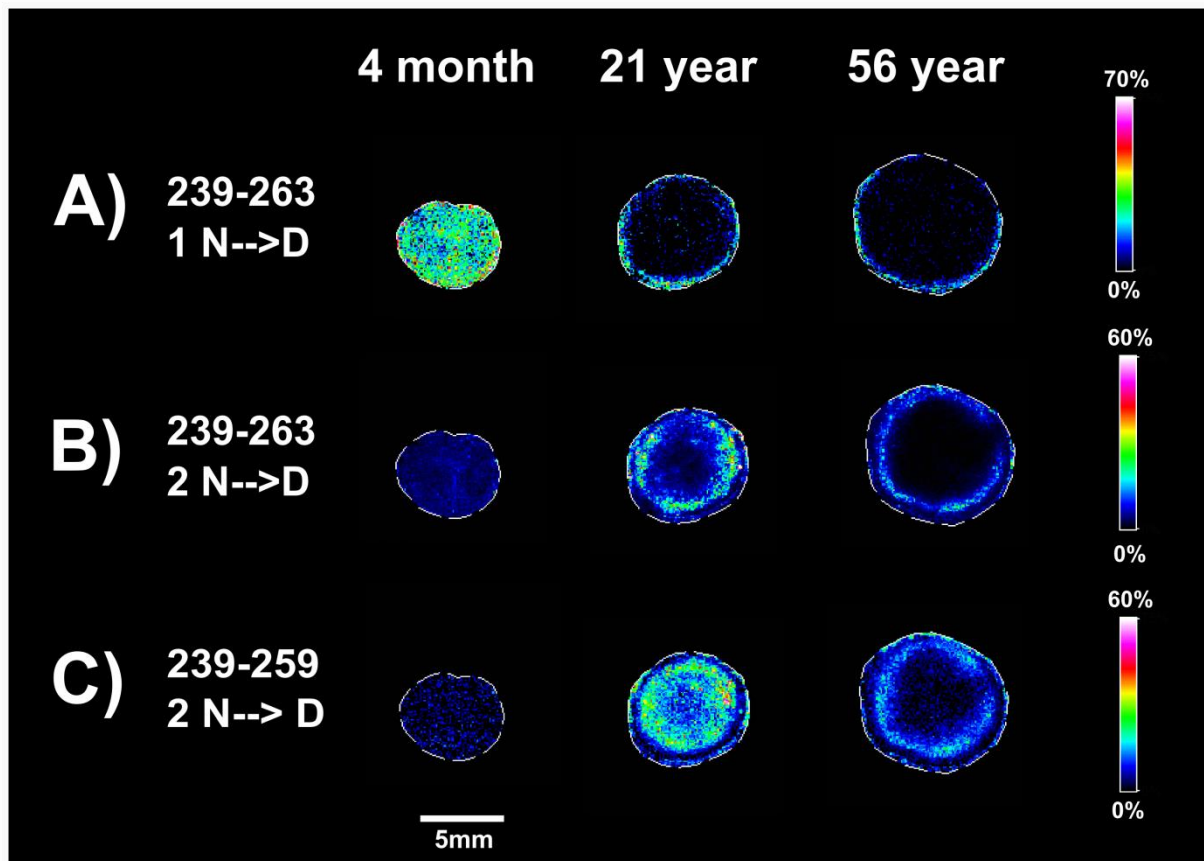


**Figure 2.9.** Age-related Accumulation of Deamidation and Truncation.

Individual ion images for full-length and truncated deamidated AQP0 C-terminal peptide are shown. Images were acquired with 100 $\mu$ m raster step size on a Bruker SolariX 15T FTICR MS. Ion intensities are normalized to the TIC for each ion across the tissue section and rainbow scale bars indicate the range of intensities plotted.

**Reprinted with permission from** Wenke JL, Rose KL, Spraggins JM, Schey KL. MALDI Imaging Mass Spectrometry Spatially Maps Age-Related Deamidation and Truncation of Human Lens Aquaporin-0. *Invest Ophthalmol Vis Sci* 2015;56:7398-7405. © ARVO

### *Microextraction and nanoLC-MS/MS Analysis for Peptide Identification*

LC-MS/MS analysis was performed to ensure the correct identification of AQP0 peptides detected in MALDI imaging experiments. Using high mass resolution Orbitrap-based instrumentation, un-, singly-, and doubly-deamidated AQP0 239-263 peptides can be distinguished by a shift in molecular weight. Using the tissue microextraction protocol, digested peptides were extracted from outer and inner cortex regions from each lens. High-resolution tandem mass spectra were acquired to confirm the deamidation sites. Figure 2.10 shows a labeled MS<sup>2</sup> spectrum for the doubly-charged, singly-deamidated 239-263 peptide, *m/z* 1276.13, confirming N246 as the deamidation site in a 21 year outer cortex region. Both N246 and N259 were modified in the doubly-deamidated peptide (data not shown). MALDI images show the singly-deamidated peptide is present in younger fiber cells, followed by the doubly-deamidated peptide in slightly older fiber cells. Together with LC-MS/MS data, these results indicate N246 is deamidated earlier than N259. This finding agrees with predicted rates of deamidation based on primary sequence; N246 is followed by a small glycine residue, whereas N259 is adjacent to a larger threonine residue.<sup>45</sup>

**Figure 2.10**

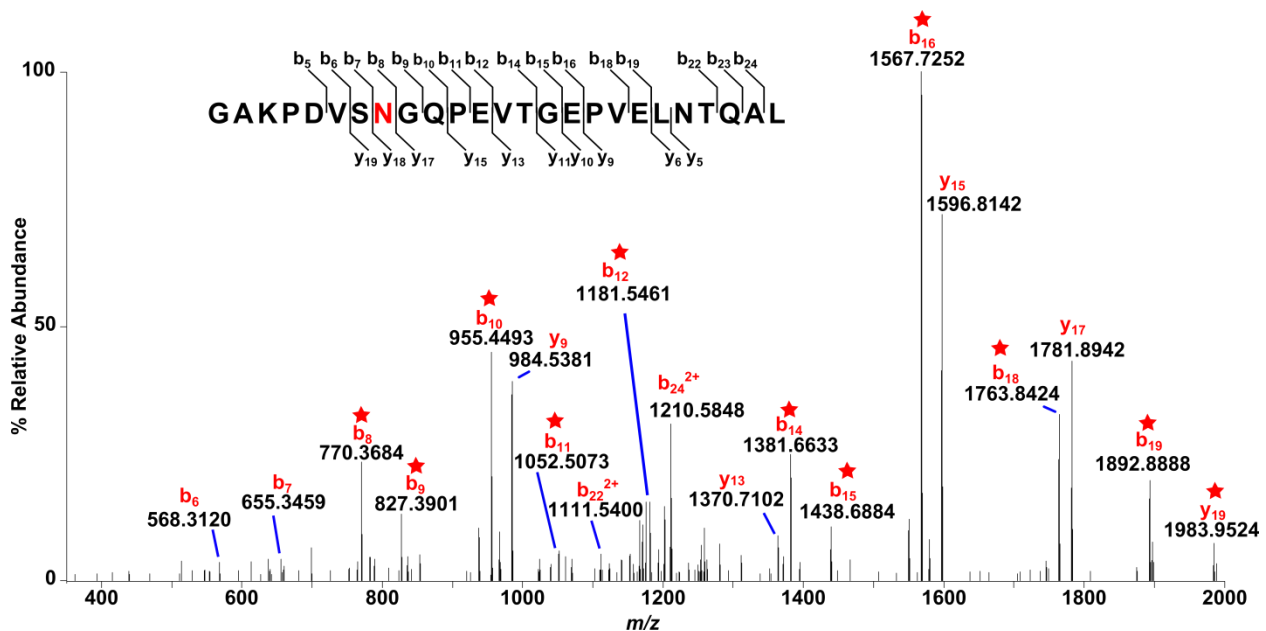


**Figure 2.10.** Tandem Mass Spectrum Identifying AQP0 Deamidation Site at N246.

High mass resolution CID spectrum of doubly-charged AQP0 peptide 239-263,  $m/z$  1276.13, acquired on a Thermo LTQ Orbitrap Velos. The observed mass corresponds to one deamidated residue on the peptide; starred peaks indicate fragments containing deamidated residue N246. The amino acid sequence showing fragmentation coverage is included above. Data shown is from microextraction of a 21 year human lens outer cortex region.

**Reprinted with permission from** Wenke JL, Rose KL, Spraggins JM, Schey KL. MALDI Imaging Mass Spectrometry Spatially Maps Age-Related Deamidation and Truncation of Human Lens Aquaporin-0. *Invest Ophthalmol Vis Sci* 2015;56:7398-7405. © ARVO

### *nanoLC-MS/MS Gradient Optimization for Deamidated Species Separation*

We demonstrated deamidation of N246 on the singly-deamidated peptide and sought to quantify the relative abundance of a variety of deamidated and truncated AQP0 C-terminal peptides. These modifications cause a shift in *m/z* and a change in isotopic distribution pattern that can be detected by high-resolution mass spectrometry instrumentation (Figure 2.11). However, deamidated peaks often overlap in the chromatogram, which renders useless quantitation based on monoisotopic extracted ion chromatogram peak area (also seen in Figure 2.11). Therefore, our strategy was to extend the gradient in the AQP0 C-terminal peptide elution range by slowing the %B rate from 0.75% B/minute to 0.3% B/minute. We also modified the method to target AQ0 peptides of interest based on *m/z* value. This ensured that even low-abundance peptides were selected for fragmentation in order to collect high-resolution MS<sup>2</sup> data for deciphering deamidation sites. Results obtained from the modified method are shown in Figure 2.12. Panel 2.12C shows the baseline separation of the 1<sup>st</sup> 13C isotope of the singly-deamidated peak (on the left) from the monoisotopic peak of the doubly-deamidated peptide. This enables use of peak areas to quantify relative abundance of deamidated and truncated species. Figure 2.13 shows the accumulation of deamidated and truncated AQP0 with fiber cell age, plotted as peak areas from LC-MS/MS data of a 21 year lens microextraction. These results agree with imaging data (Figures 2.8 and 2.9), revealing early deamidation followed by truncation.

Asparagine and aspartic acid residues are extremely labile, prone to reactions that can result in deamidation, isomerization, racemization, and backbone cleavage as depicted in Figure 2.14. In our peptide imaging experiments, we detect deamidated species, which proceed through a succinimide intermediate. Backbone cleavage occurs at asparagine or aspartic acid through an

alternate mechanism. These reactions have been reported extensively in the long-lived lens, for both crystallins<sup>44</sup> and AQP0.<sup>34</sup> Additional confirmation of these reactions is shown in the irregular chromatography of the AQP0 C-terminal peptide. Note the non-Gaussian chromatographic peak shape in Figure 2.12C; this is likely due to isomerization and racemization at labile asparagine residues. Despite our attempts to optimize the chromatographic gradient, we were not able to fully separate isomers of these peptides. However, our lab has previously demonstrated isomers of human lens AQP0 peptide (239-244) can be chromatographically resolved.<sup>34</sup>

**Figure 2.11**

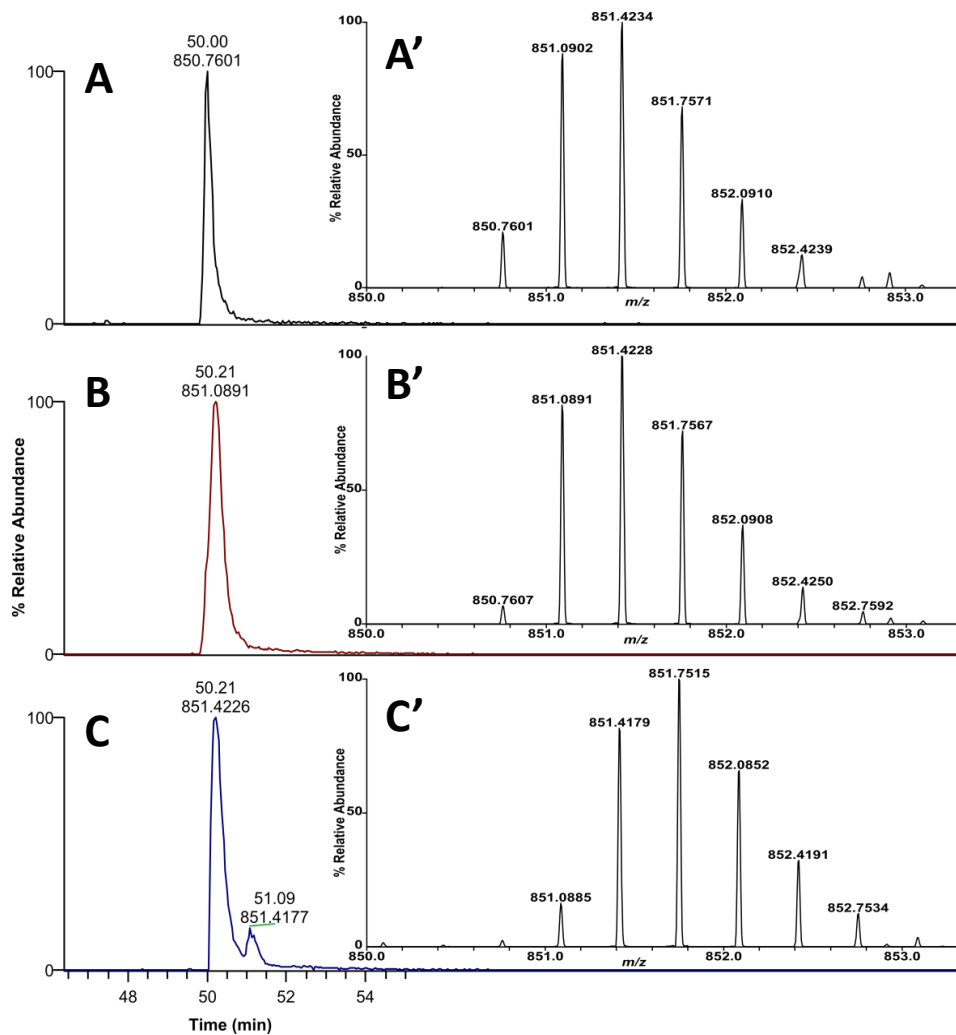


**Figure 2.11.** Chromatographic Traces for Original Elution Gradient (0.75 %B/min) for Triply-Charged AQP0 C-terminal Peptide 239-263 with 0, 1, and 2 Deamidation Events. Data shown are from microextraction of a 4-month human lens outer cortex region. Each trace is an extracted ion chromatogram for the monoisotopic peak corresponding to the triply-charged AQP0 peptide. Note overlapping retention times for undeamidated (A) and singly-deamidated peptide (B).

(A): Undeamidated AQP0 peptide, GAKPDVSNGQPEVTGEPVELNTQAL,  $m/z$  850.7601 (0.9 ppm error)

(B): Singly deamidated AQP0 peptide, GAKPDVS~~D~~GQPEVTGEPVELNTQAL,  $m/z$  851.0891 (0.2 ppm error)

(C): Doubly deamidated AQP0 peptide, GAKPDVS~~D~~GQPEVTGEPVELDTQAL,  $m/z$  851.4179 (1.2 ppm error)

(A')(B')(C'): Insets show a representative MS1 spectrum underneath each chromatographic trace. Note the shifting isotopic distribution as deamidation occurs (moving from A' to C').

**Figure 2.12**

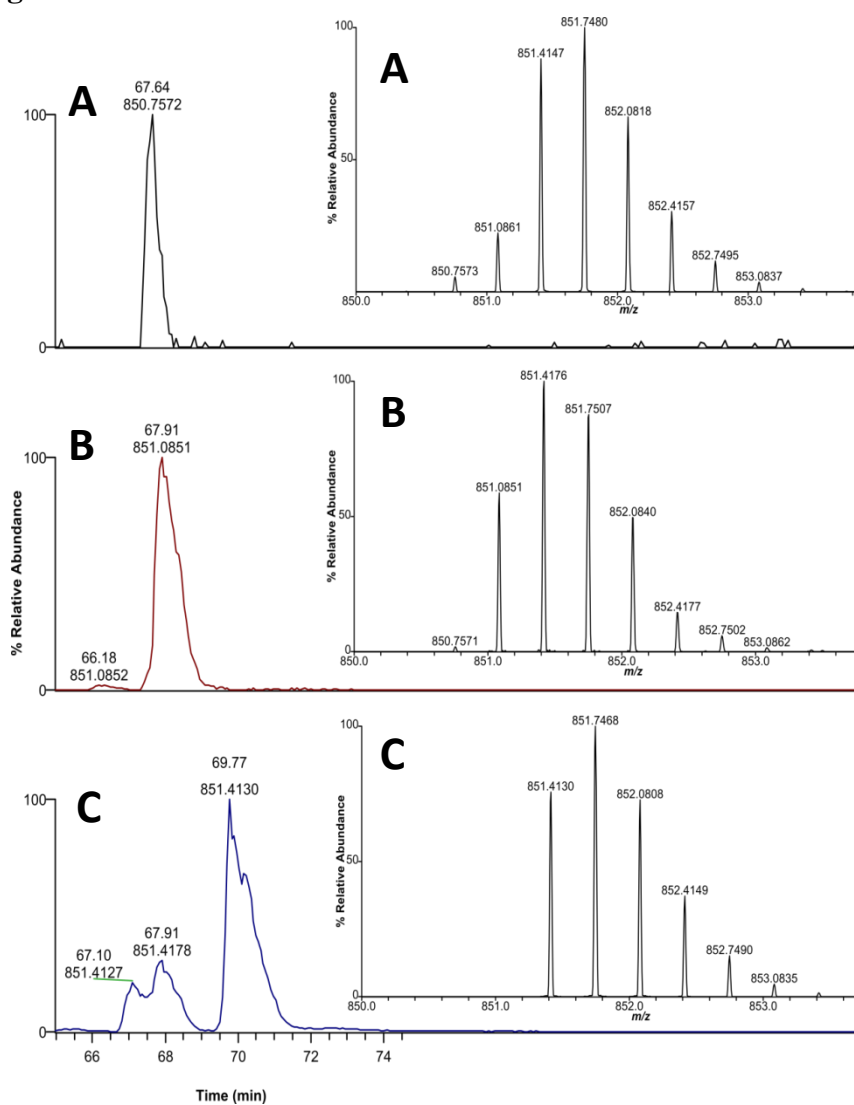


**Figure 2.12.** Extended Gradient (0.3 % B/min) in AQP0 Peptide Elution Range Enables Baseline Separation of Differentially-Deamidated Species. Data shown are from microextraction of a 21 year human lens outer cortex region. Each trace is an extracted ion chromatogram for the monoisotopic peak corresponding to the triply-charged AQP0 peptide.

- (A): Undeamidated AQP0 peptide, GAKPDVSNGQPEVTGEPVELNTQAL,  $m/z$  850.7572 (4.3 ppm error)
- (B): Singly deamidated AQP0 peptide, GAKPDVS~~D~~GQPEVTGEPVELNTQAL,  $m/z$  851.0851 (4.5 ppm error)
- (C): Doubly deamidated AQP0 peptide, GAKPDVS~~D~~GQPEVTGEPVELDTQAL,  $m/z$  851.4130 (4.6 ppm error)
- (A')(B')(C'): Insets show a representative MS1 spectrum underneath each chromatographic trace. Note the shifting isotopic distribution as deamidation occurs (moving from A' to C').

**Figure 2.13**

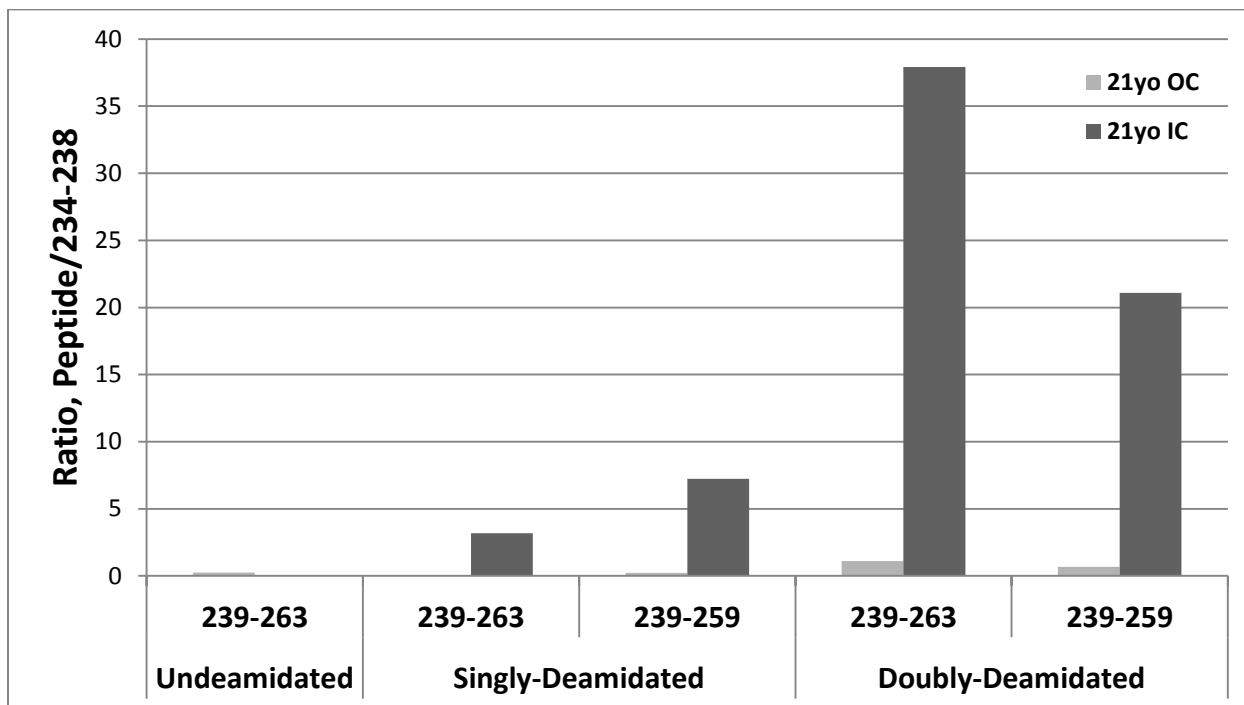


**Figure 2.13.** Deamidation of AQP0 C-terminal Peptide Accumulates with Age.

Peptide peak areas generated from the extracted ion chromatogram were plotted and normalized to an unmodified AQP0 peptide (LSVLK, residues 234-238). Levels of deamidation are higher in the inner cortical fiber cells (21yo OC) compared to the outer cortex (21yo IC). Signal of the truncated peptide is highest in the inner cortex.

**Reprinted with permission from** Wenke JL, Rose KL, Spraggins JM, Schey KL. MALDI Imaging Mass Spectrometry Spatially Maps Age-Related Deamidation and Truncation of Human Lens Aquaporin-0. *Invest Ophthalmol Vis Sci* 2015;56:7398-7405. © ARVO

**Figure 2.14**

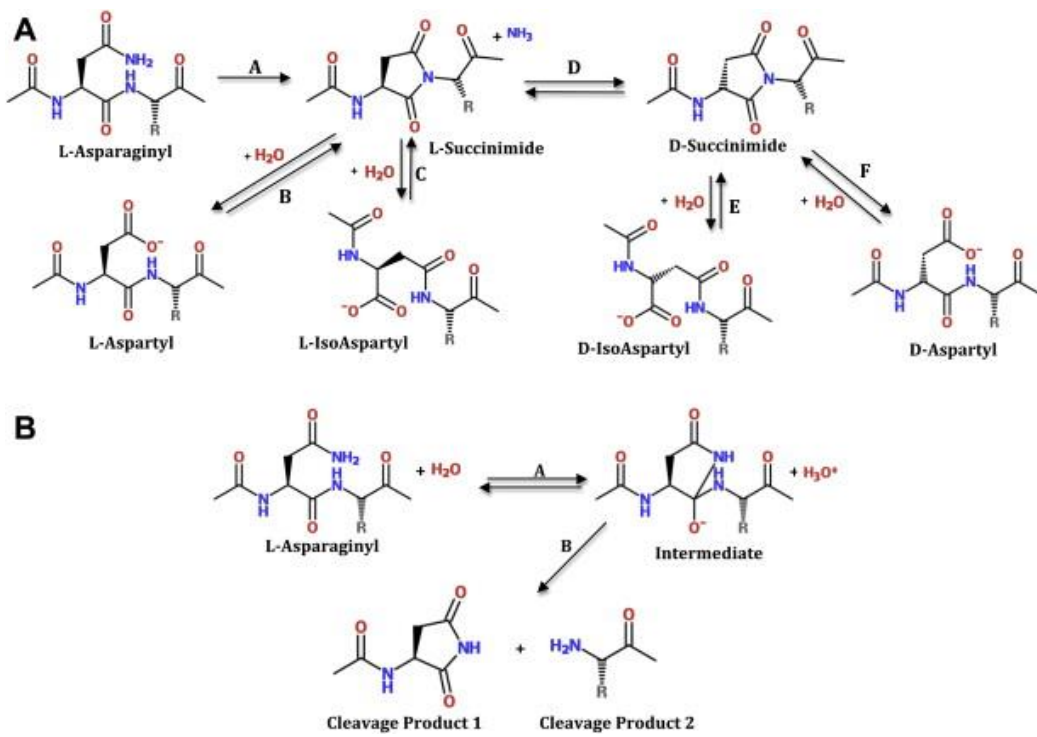


**Figure 2.14.** Reactions of the Labile Asn/Asp residues in Proteins from Aged Lenses.

Step A, formation of a succinimide ring structure and loss of ammonia. Step B, hydrolysis of succinimide ring and formation of L-Asp. Note: L-Asp residues can also undergo the reverse reaction to form the succinimide ring. Step C, alternate hydrolysis of succinimide ring to form L-IsoAsp. Step D, racemization of L-succinimide ring to the D-succinimide ring form. Steps E and F, hydrolysis of D-succinimide ring to either D-IsoAsp or D-Asp, respectively. B. Backbone cleavage at Asn/Asp (shown for Asn). The cleavage reaction is in competition with formation of the succinimide ring shown in Fig. 1A.

**Reprinted with permission from** Lampi KJ, Wilmarth PA, Murray MR, David LL. Lens beta-crystallins: the role of deamidation and related modifications in aging and cataract. *Prog Biophys Mol Biol* 2014;115:21-31.<sup>46</sup>

### *Multiple-Charging for Intact AQP0 Analysis by FTICR MS*

By spotting 2-NPG matrix, shown to produce multiply-charged analytes by MALDI,<sup>42</sup> we could detect the intact AQP0 protein by FTICR MS. Figure 2.15 shows the full mass spectrum from a 21-year cortex profiling experiment. The major peak, average mass  $m/z$  7031.57, corresponds to quadruply-charged AQP0 protein. Zooming in on this peak, we can detect isotopes (separated by 0.25 Da), calculate the charge state (+4) and calculate the exact mass of this species (Figure 15 inset). This peak from the 21-year human lens outer cortex corresponds to full-length AQP0,  $m/z$  28,122.73 (predicted mass 28,123.72). Unfortunately, we did not detect fatty acid acylated or other modified forms of AQP0 in this experiment. The use of 2-NPG enabled detection of the large 28kDa protein AQP0 directly from human lens sections. To our knowledge, this is one of the larger proteins to be detected from tissue by MALDI FTICR MS and certainly the first integral membrane protein. Future work will test different solvents and matrix application methods to enable better extraction and co-crystallization of extremely hydrophobic forms of AQP0 with the matrix. This method has the potential to reveal small  $m/z$  modifications on the intact AQP0 protein, something that has remained impossible with traditional MALDI TOF analysis.

**Figure 2.15**

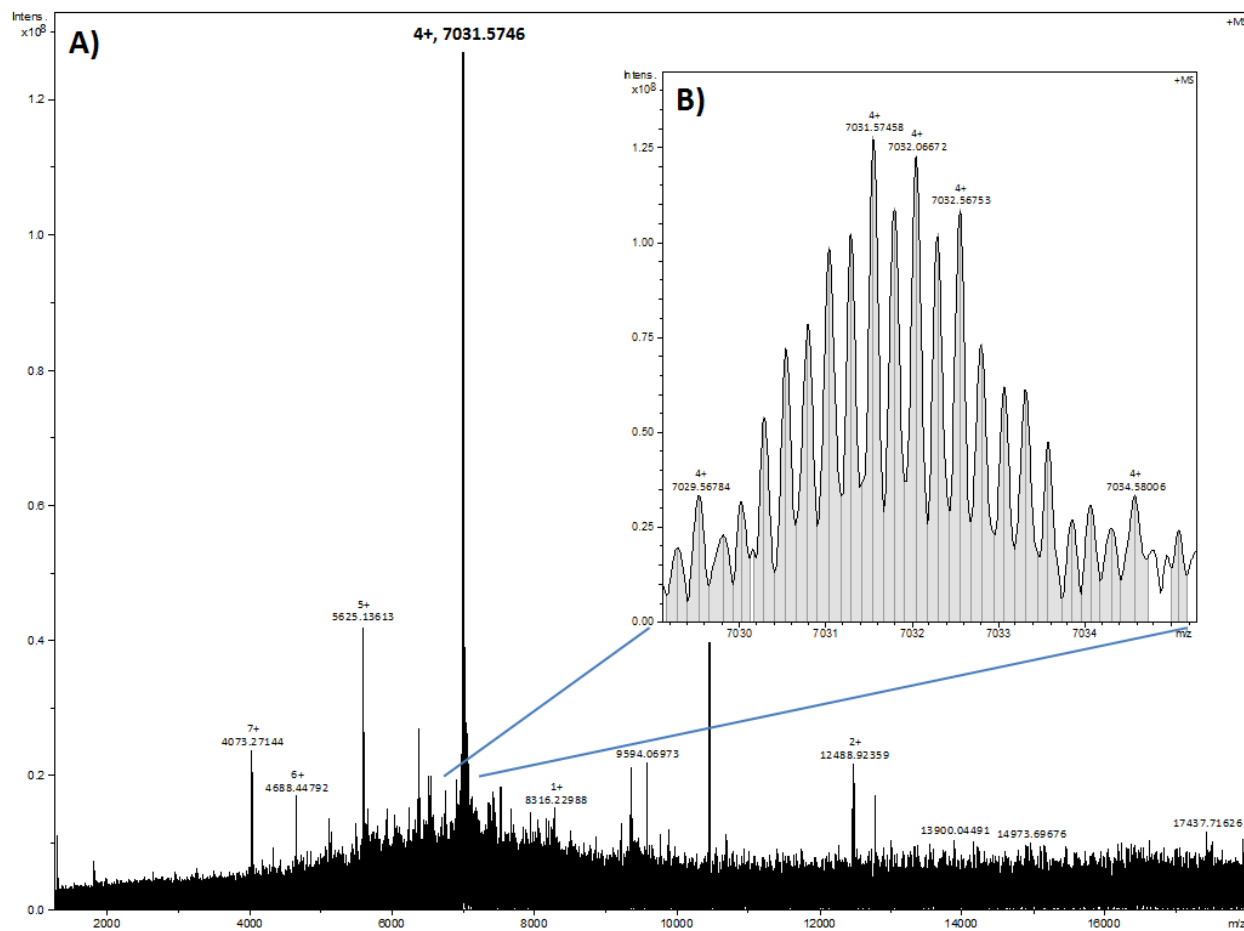


**Figure 2.15.** Multiply-Charged Intact AQP0 is Detected by MALDI FTICR MS Profiling using 2-NPG Matrix.

(A) Mass spectrum from 21-year human outer cortex. Peak at 7031 corresponds to +4 AQP0.  
(B) Zoomed-in spectrum showing isotopic distribution of AQP0 peak.

### *In situ Digestion and MALDI IMS of Other Insoluble Lens Proteins*

Although imaging AQP0 C-terminal peptide was the focus of our *in situ* digestion and MALDI IMS experiments, our results yielded hundreds of peptide peaks with unique distribution throughout the lens. We also imaged a 69-year lens after washing and tryptic digestion to look for the accumulation of insoluble proteins. Signals from the MALDI IMS experiment were identified by matching FTICR MS accurate mass to peptides identified by microextraction and analysis on the LTQ Orbitrap Velos. Several crystallin peptides were detected, including  $\alpha$ A 13-21 and  $\gamma$ S 159-174. The presence of these peptides after a series of stringent water washes indicates these crystallins are rather insoluble. Furthermore, we detected peptide fragments of larger membrane and cytoskeletal proteins including MP20, and beaded filament proteins filensin and phakinin (Figure 2.16). These proteins are typically challenging to detect in imaging experiments for several reasons. The membrane protein MP20 is much less abundant than AQP0 and falls in the same mass range as many crystallins. Filensin and phakinin are large proteins (~75kDa and ~45kDa, respectively) outside the typical working mass range for many commercial instruments. By digesting these proteins into smaller fragments, we enabled spatial mapping of fragments from numerous proteins that have not been detected by MALDI IMS in the past.

**Figure 2.16**

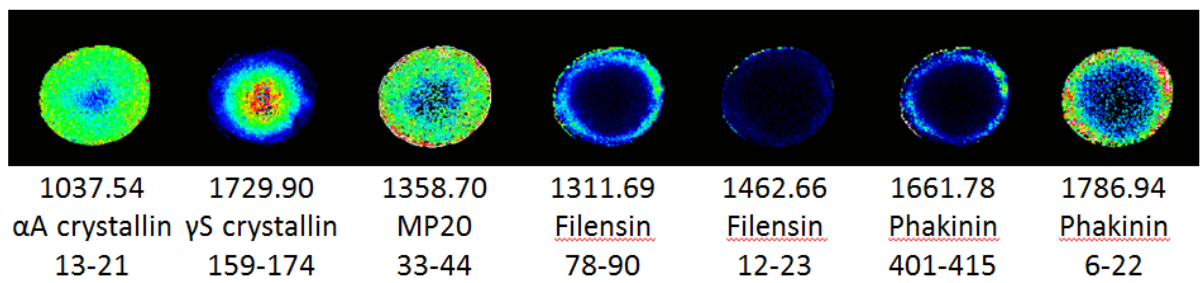


**Figure 2.16.** *In situ* Digestion and MALDI IMS of Insoluble Lens Proteins from a 69-Year Human Lens. This technique enabled imaging of peptide fragments from proteins that are not typically detected by MALDI IMS.

## Discussion

Extensive AQP0 truncation is detected in the inner cortex and nucleus of all lenses except the youngest, 2 month and 4 month lenses (Figures 2.1, 2.2, and 2.3). Data from a 21 year lens indicate that nearly half of AQP0 is truncated. These results agree with published data, which concludes that the half-life of AQP0 truncation is 24 years.<sup>32</sup> AQP0 cleavage is expected to be non-enzymatic, as there is little enzymatic activity in mature fiber cells and truncation at asparagine residues likely proceeds via a well-studied backbone cleavage mechanism (Figure 2.14).<sup>47</sup> Furthermore, *in vitro* studies demonstrated spontaneous cleavage at N246 and N259 after peptide incubation at 37°C in ammonium bicarbonate buffer.<sup>34</sup> Although most AQP0 is fated for truncation, the functional consequences of this modification are disputed. Crystals formed from nuclear AQP0, which is mostly truncated, tended to form bilayers.<sup>7</sup> Treatment of AQP0 with proteolytic enzymes generates more junctional AQP0<sup>7</sup> and structural characterization suggests the truncated junctional form has a closed water pore.<sup>48</sup> However, functional studies demonstrated equal permeability of full-length and truncated AQP0<sup>5, 35</sup> and showed full-length AQP0 has adhesive properties.<sup>6</sup> Another possible consequence of C-terminal truncation is that key residues involved in AQP0 protein-protein interactions are removed. Perhaps AQP0 binding with cytoskeletal proteins filensin, phakinin, and ezrin are no longer required in deep cortical cells since the fiber cell architecture has already been established in the outer cortex.<sup>26, 27, 30</sup> Removal of the AQP0 C-terminus could also permit binding of increasingly insoluble proteins and complexes to the plasma membrane, potentially contributing to the lens permeability barrier and hardening around age 50.<sup>30, 49</sup> Recent studies conclude that truncation of AQP0 termini could help establish a proper refractive index gradient across the lens.<sup>5, 50</sup> Although the precise function of truncated AQP0 remains to be determined, it is remarkable that such extensive cleavage

occurs even in healthy lenses at relatively young ages. Labile asparagine residues could serve as a molecular clock for predictable truncation, as a means of modulating AQP0 function in mature fiber cells.

Imaging results show fatty acid acylated AQP0 in all lenses, including young (2 month) cortex and core (Figures 2.4 and 2.5). Previous MALDI profiling and imaging experiments revealed full-length (1-263) and truncated (1-246) fatty acid acylated AQP0 in an 11 year lens,<sup>31</sup> <sup>32</sup> but other studies did not detect lipidated AQP0 in fetal lens.<sup>30</sup> Our discovery of lipid-modified AQP0 in a very young lens suggests acylation may be developmentally programmed in younger fiber cells and not simply a consequence of AQP0 co-existing with membrane lipids for years. Our results suggest AQP0 is acylated in primary fiber cells of the fetal nucleus and in newly-synthesized AQP0 of secondary fibers. Over time, the fatty acid modification is observed on truncated AQP0, suggesting fatty acylation is an irreversible post-translational modification in lens. Although N-terminal acylation is a fairly common modification, the mechanism for fatty acid acylation of lysine is unknown and no acyl transferases have been discovered that attach lipids to lysine residues. Lipid-modified AQP0 was shown to purify with detergent-resistant, or lipid-raft, regions of the plasma membrane.<sup>31</sup> We hypothesize that the presence of a large fatty acid on the N- or C-terminus of AQP0 could help anchor the protein to the plasma membrane or target the protein to lipid raft regions for specific protein-protein interactions. AQP0 localization within the plasma membrane changes based on distance into the lens, starting with an even distribution throughout the plasma membrane and eventually forming ribbon-like structures on the broad sides of fiber cells.<sup>51</sup> The mechanism of AQP0 redistribution remains to be determined.

For the first time, deamidated forms of a protein were resolved and imaged by MALDI FTICR IMS (Figures 2.7, 2.8, and 2.9). Deamidation is a common protein modification, resulting

in an extremely small mass shift (+0.9847 Da), and is considered a molecular clock that reflects protein age. If both deamidated and undeamidated peptides are present in a sample, it is challenging to mass resolve the monoisotopic form of the deamidated peptide from the first  $^{13}\text{C}$  isotope (+1.0034 Da) of the undeamidated peptide. To overcome this issue, we performed *in situ* digestion directly on lens sections to generate spatially-localized tryptic peptides and used a high mass resolution FTICR for imaging analysis (~250,000 resolving power at  $m/z$  2,550). Tryptic digestion on tissue sections has been used to profile and image peptides from formalin-fixed, paraffin-embedded (FFPE) and frozen tissue sections.<sup>52-54</sup>

Based on AQP0 peptide images, differentially deamidated AQP0 forms have distinct, age-specific spatial localization within the lens. As shown in Figure 2.7, the 4 month lens contained un-, singly, and doubly-deamidated AQP0 peptides. These peptides form concentric rings in the lens as deamidation accumulates with increasing fiber cell age. Undeamidated AQP0 was only detected by MALDI in the 4 month lens. Figures 2.8 and 2.9 highlight the accumulation of deamidation and then truncation in older lenses. Loss of truncated, doubly-deamidated AQP0 peptide is likely due to further truncation, as observed in AQP0 protein images and in Figure 2.13. It is noteworthy that the major truncation sites of AQP0 occur at residues 246 and 259 in AQP0; asparagine residues known to be deamidated in AQP0 and consistent with a non-enzymatic mechanism of cleavage. Singly-deamidated peptides contain N246D, indicating deamidation occurs more rapidly at N246 than at N259. Furthermore, it is unlikely that the observed deamidation is due to sample preparation because undeamidated AQP0 is still detected in the outer cortex of the 4 month lens and deamidated forms of AQP0 have unique spatial localization.

Asparagine residues can spontaneously form a cyclic succinimide intermediate, which can produce iso- or aspartic acid through loss of NH<sub>3</sub> (see Figure 2.14A).<sup>47</sup> As shown in Figure 2.14B, this pathway can also lead to non-enzymatic truncation, as described for crystallins<sup>55</sup> and for AQP0 *in vitro*.<sup>34</sup> Deamidation rates can be reliably predicted based on protein primary structure, although secondary structure and other factors including pH, temperature, and time also dictate the rate of formation. Asparagine residues followed by small amino acids are rapidly deamidated, whereas larger residues provide steric hindrance and slow deamidation rates considerably.<sup>45</sup> In AQP0, we observed N246 (sequence SNG) to be deamidated more rapidly than N259 (sequence LNT). Previous work also indicates truncation is more common at slowly-deamidating residues.<sup>56</sup> In AQP0, residue 259 undergoes deamidation more slowly than 246 and truncation at residue 259 is the first to accumulate based on our imaging results.

It remains to be seen whether asparagine and aspartic acid residues in AQP0 could serve as a programmed way to direct cleavage events along the peptide backbone. Although deamidation could be a random aging event, it is noteworthy that asparagine residues occur 28% more frequently in all proteins than expected by random chance.<sup>47</sup> The primary sequence of AQP0 could be designed to include susceptible residues for targeted cleavage in human lens over time. As the human lens is understood to contain less calpain than other species, this could serve as an alternative to calpain-directed cleavage more common in rodent lens.<sup>38</sup> More work is needed to fully understand the functional implications of deamidation and truncation in AQP0 and in the lens overall.

## Conclusions

These studies have utilized cutting-edge mass spectrometry technology and optimized methods to analyze modified AQP0 across multiple ages of human lens. MALDI imaging of AQP0 protein and tryptic peptides, combined with microextraction proteomics data from LC-MS/MS analysis, enabled mapping of large and small AQP0 PTMs ranging from lipidation to deamidation. LC-MS/MS gradient optimization was helpful in separating differentially deamidated species, and multiply-charged FTICR MS MALDI profiling showed promising results for determining accurate mass at the intact protein level. Most importantly, these technologies provide additional insight into age-related processing of AQP0 over time. Our results are the first to show that AQP0 is fatty acid acylated in a very young lens nucleus. For the first time, we imaged deamidated tryptic peptides and showed the time course of AQP0 deamidation in human lens, which begins at a very young age. Spatial mapping of modified forms of AQP0 shows where AQP0 function is likely to change across the human lens.

In the future, these methods can be applied to study other lens protein modifications. This technology could provide a better understanding of crystallin racemization and deamidation reactions, which are accelerated in cataract lenses.<sup>57, 58</sup> *In situ* digestion and imaging is also useful for mapping other membrane and cytoskeletal proteins that are not typically detected at the intact protein level due to large size or lower abundance in lens. As instrumentation and sample preparation techniques continue to improve, we anticipate that spatially-resolved proteomics will continue to shed light on age-related lens modifications, advancing our understanding of lens physiology and aging.

## References

1. Wenke JL, Rose KL, Spraggins JM, Schey KL. MALDI Imaging Mass Spectrometry Spatially Maps Age-Related Deamidation and Truncation of Human Lens Aquaporin-0. *Invest Ophthalmol Vis Sci* 2015;56:7398-7405.
2. Alcala J, Lieska N, Maisel H. Protein composition of bovine lens cortical fiber cell membranes. *Exp Eye Res* 1975;21:581-595.
3. Kushmerick C, Rice SJ, Baldo GJ, Haspel HC, Mathias RT. Ion, water and neutral solute transport in Xenopus oocytes expressing frog lens MIP. *Exp Eye Res* 1995;61:351-362.
4. Costello MJ, McIntosh TJ, Robertson JD. Distribution of gap junctions and square array junctions in the mammalian lens. *Invest Ophthalmol Vis Sci* 1989;30:975-989.
5. Kumari SS, Varadaraj K. Intact and N- or C-terminal end truncated AQP0 function as open water channels and cell-to-cell adhesion proteins: end truncation could be a prelude for adjusting the refractive index of the lens to prevent spherical aberration. *Biochim Biophys Acta* 2014;1840:2862-2877.
6. Kumari SS, Varadaraj K. Intact AQP0 performs cell-to-cell adhesion. *Biochem Biophys Res Commun* 2009;390:1034-1039.
7. Gonen T, Cheng Y, Kistler J, Walz T. Aquaporin-0 membrane junctions form upon proteolytic cleavage. *J Mol Biol* 2004;342:1337-1345.
8. Fotiadis D, Hasler L, Muller DJ, Stahlberg H, Kistler J, Engel A. Surface tongue-and-groove contours on lens MIP facilitate cell-to-cell adherence. *J Mol Biol* 2000;300:779-789.
9. Colom A, Casuso I, Boudier T, Scheuring S. High-speed atomic force microscopy: cooperative adhesion and dynamic equilibrium of junctional microdomain membrane proteins. *J Mol Biol* 2012;423:249-256.
10. Simon SA, Zampighi G, McIntosh TJ, Costello MJ, Ting-beall HP, Robertson JD. The structure of junctions between lens fiber cells. *Biosci Rep* 1982;2:333-341.
11. Kumari SS, Gandhi J, Mustehsan MH, Eren S, Varadaraj K. Functional characterization of an AQP0 missense mutation, R33C, that causes dominant congenital lens cataract, reveals impaired cell-to-cell adhesion. *Exp Eye Res* 2013;116:371-385.
12. Varadaraj K, Kumari SS, Patil R, Wax MB, Mathias RT. Functional characterization of a human aquaporin 0 mutation that leads to a congenital dominant lens cataract. *Exp Eye Res* 2008;87:9-21.

13. Hu S, Wang B, Qi Y, Lin H. The Arg233Lys AQP0 mutation disturbs aquaporin0-calmodulin interaction causing polymorphic congenital cataract. *PLoS ONE* 2012;7:e37637.
14. Shiels A, Bassnett S, Varadaraj K, et al. Optical dysfunction of the crystalline lens in aquaporin-0-deficient mice. *Physiol Genomics* 2001;7:179-186.
15. Shiels A, Mackay D, Bassnett S, Al-Ghoul K, Kuszak J. Disruption of lens fiber cell architecture in mice expressing a chimeric AQP0-LTR protein. *FASEB J* 2000;14:2207-2212.
16. Shentu X, Miao Q, Tang X, Yin H, Zhao Y. Identification and Functional Analysis of a Novel MIP Gene Mutation Associated with Congenital Cataract in a Chinese Family. *PLoS ONE* 2015;10:e0126679.
17. Song Z, Wang L, Liu Y, Xiao W. A novel nonsense mutation in the MIP gene linked to congenital posterior polar cataracts in a Chinese family. *PLoS ONE* 2015;10:e0119296.
18. Yu Y, Chen P, Li J, Zhu Y, Zhai Y, Yao K. A novel MIP gene mutation associated with autosomal dominant congenital cataracts in a Chinese family. *BMC Med Genet* 2014;15:6.
19. Francis P, Berry V, Bhattacharya S, Moore A. Congenital progressive polymorphic cataract caused by a mutation in the major intrinsic protein of the lens, MIP (AQP0). *Br J Ophthalmol* 2000;84:1376-1379.
20. Okamura T, Miyoshi I, Takahashi K, et al. Bilateral congenital cataracts result from a gain-of-function mutation in the gene for aquaporin-0 in mice. *Genomics* 2003;81:361-368.
21. Gu F, Zhai H, Li D, et al. A novel mutation in major intrinsic protein of the lens gene (MIP) underlies autosomal dominant cataract in a Chinese family. *Mol Vis* 2007;13:1651-1656.
22. Senthil Kumar G, Kyle JW, Minogue PJ, et al. An MIP/AQP0 mutation with impaired trafficking and function underlies an autosomal dominant congenital lamellar cataract. *Exp Eye Res* 2013;Exp Eye Res:136-141.
23. Reichow SL, Clemens DM, Freites JA, et al. Allosteric mechanism of water-channel gating by Ca<sup>2+</sup>-calmodulin. *Nat Struct Mol Biol* 2013;20:1085-1092.
24. Reichow SL, Gonon T. Noncanonical binding of calmodulin to aquaporin-0: implications for channel regulation. *Structure* 2008;16:1389-1398.
25. Rose KML, Wang Z, Magrath GN, Hazard ES, Hildebrandt JD, Schey KL. Aquaporin 0-calmodulin interaction and the effect of aquaporin 0 phosphorylation. *Biochemistry* 2008;47:339-347.

26. Lindsey Rose KM, Gourdie RG, Prescott AR, Quinlan RA, Crouch RK, Schey KL. The C terminus of lens aquaporin 0 interacts with the cytoskeletal proteins filensin and CP49. *Invest Ophthalmol Vis Sci* 2006;47:1562-1570.
27. Wang Z, Schey KL. Aquaporin-0 interacts with the FERM domain of ezrin/radixin/moesin proteins in the ocular lens. *Invest Ophthalmol Vis Sci* 2011;52:5079-5087.
28. Varadaraj K, Kumari S, Shiels A, Mathias RT. Regulation of aquaporin water permeability in the lens. *Invest Ophthalmol Vis Sci* 2005;46:1393-1402.
29. Nemeth-Cahalan KL, Hall JE. pH and calcium regulate the water permeability of aquaporin 0. *J Biol Chem* 2000;275:6777-6782.
30. Korlimbinis A, Berry Y, Thibault D, Schey KL, Truscott RJW. Protein aging: truncation of aquaporin 0 in human lens regions is a continuous age-dependent process. *Exp Eye Res* 2009;88:966-973.
31. Schey KL, Gutierrez DB, Wang Z, Wei J, Grey AC. Novel Fatty Acid Acylation of Lens Integral Membrane Protein Aquaporin-0. *Biochemistry* 2010;49:9858-9865.
32. Gutierrez DB, Garland D, Schey KL. Spatial analysis of human lens aquaporin-0 post-translational modifications by MALDI mass spectrometry tissue profiling. *Exp Eye Res* 2011;93:912-920.
33. Schey KL, Little M, Fowler JG, Crouch RK. Characterization of human lens major intrinsic protein structure. *Invest Ophthalmol Vis Sci* 2000;41:175-182.
34. Ball LE, Garland DL, Crouch RK, Schey KL. Post-translational modifications of aquaporin 0 (AQP0) in the normal human lens: spatial and temporal occurrence. *Biochemistry* 2004;43:9856-9865.
35. Ball LE, Little M, Nowak MW, Garland DL, Crouch RK, Schey KL. Water Permeability of C-Terminally Truncated Aquaporin 0 (AQP0 1-243) Observed in the Aging Human Lens. *Invest Ophthalmol Vis Sci* 2003;44:4820-4828.
36. Grey AC, Chaurand P, Caprioli RM, Schey KL. MALDI imaging mass spectrometry of integral membrane proteins from ocular lens and retinal tissue. *J Proteome Res* 2009;8:3278-3283.
37. Caprioli RM, Farmer TB, Gile J. Molecular imaging of biological samples: localization of peptides and proteins using MALDI-TOF MS. *Anal Chem* 1997;69:4751-4760.
38. Grey AC, Li L, Jacobs MD, Schey KL, Donaldson PJ. Differentiation-dependent modification and subcellular distribution of aquaporin-0 suggests multiple functional roles in the rat lens. *Differentiation* 2009;77:70-83.

39. Deininger SO, Cornett DS, Paape R, et al. Normalization in MALDI-TOF imaging datasets of proteins: practical considerations. *Anal Bioanal Chem* 2011;401:167-181.
40. Shen M, Xiang P, Shi Y, Pu H, Yan H, Shen B. Mass imaging of ketamine in a single scalp hair by MALDI-FTMS. *Anal Bioanal Chem* 2014;406:4611-4616.
41. Schey KL, Anderson DM, Rose KL. Spatially-directed protein identification from tissue sections by top-down LC-MS/MS with electron transfer dissociation. *Anal Chem* 2013;85:6767-6774.
42. Trimpin S, Ren Y, Wang B, et al. Extending the laserspray ionization concept to produce highly charged ions at high vacuum on a time-of-flight mass analyzer. *Anal Chem* 2011;83:5469-5475.
43. Thibault DB, Gillam CJ, Grey AC, Han J, Schey KL. MALDI tissue profiling of integral membrane proteins from ocular tissues. *J Am Soc Mass Spectrom* 2008;19:814-822.
44. Robinson NE, Lampi KJ, McIver RT, et al. Quantitative measurement of deamidation in lens betaB2-crystallin and peptides by direct electrospray injection and fragmentation in a Fourier transform mass spectrometer. *Mol Vis* 2005;11:1211-1219.
45. Robinson NE, Robinson AB. Deamidation of human proteins. *Proc Natl Acad Sci U S A* 2001;98:12409-12413.
46. Lampi KJ, Wilmarth PA, Murray MR, David LL. Lens beta-crystallins: the role of deamidation and related modifications in aging and cataract. *Prog Biophys Mol Biol* 2014;115:21-31.
47. Robinson NE, Robinson AB. *Molecular Clocks*. Cave Junction, OR: Althouse Press; 2004.
48. Gonen T, Sliz P, Kistler J, Cheng Y, Walz T. Aquaporin-0 membrane junctions reveal the structure of a closed water pore. *Nature* 2004;429:193-197.
49. Heys KR, Friedrich MG, Truscott RJW. Presbyopia and heat: changes associated with aging of the human lens suggest a functional role for the small heat shock protein,  $\alpha$ -crystallin, in maintaining lens flexibility. *Aging Cell* 2007;6:807-815.
50. Kumari SS, Varadaraj K. Aquaporin 0 plays a pivotal role in refractive index gradient development in mammalian eye lens to prevent spherical aberration. *Biochem Biophys Res Commun* 2014;452:986-991.
51. Zampighi GA, Eskandari S, Hall JE, Zampighi L, Kreman M. Micro-domains of AQP0 in lens equatorial fibers. *Exp Eye Res* 2002;75:505-519.

52. Groseclose MR, Andersson M, Hardesty WM, Caprioli RM. Identification of proteins directly from tissue: in situ tryptic digestions coupled with imaging mass spectrometry. *J Mass Spectrom* 2007;42:254-262.
53. Casadonte R, Caprioli RM. Proteomic analysis of formalin-fixed paraffin-embedded tissue by MALDI imaging mass spectrometry. *Nat Protoc* 2011;6:1695-1709.
54. Stauber J, MacAleese L, Franck J, et al. On-tissue protein identification and imaging by MALDI-Ion mobility mass spectrometry. *J Am Soc Mass Spectrom* 2010;21:338-347.
55. Voorter CE, A. dH-HW, van den Oetelaar PJ, Bloemendaal H, de Jong WW. Spontaneous peptide bond cleavage in aging alpha-crystallin through a succinimide intermediate. *J Biol Chem* 1988;263:19020-19023.
56. Geiger T, Clarke S. Deamidation, isomerization, and racemization at asparaginyl and aspartyl residues in peptides. Succinimide-linked reactions that contribute to protein degradation. *J Biol Chem* 1987;262:785-794.
57. Hooi MY, Raftery MJ, Truscott RJ. Racemization of two proteins over our lifespan: deamidation of asparagine 76 in gammaS crystallin is greater in cataract than in normal lenses across the age range. *Invest Ophthalmol Vis Sci* 2012;53:3554-3561.
58. Hooi MY, Raftery MJ, Truscott RJ. Accelerated aging of Asp 58 in alphaA crystallin and human cataract formation. *Exp Eye Res* 2013;106:34-39.

## **Chapter III – Spatially-Resolved Proteomics of the Human Lens Remodeling Zone**

### **Summary**

The recently observed lens remodeling zone is a region approximately 20-40  $\mu\text{m}$  wide, located 100  $\mu\text{m}$  beneath the capsule in human lenses. Microscopy studies have described the morphological features of cells in this region, including the rapid appearance of ball-and-socket joints and the presence of nuclei. Deeper into the lens, the transition zone is characterized by the absence of nuclei and regular membrane undulations as the cells become more recognizable and return to a classic hexagonal shape. Still, the remodeling zone remains to be characterized at the molecular level. Although the MALDI IMS methods outlined in Chapter II provided an abundance of information about protein changes across the entire human lens, the effective spatial resolution (100-200  $\mu\text{m}$ ) would not be helpful for differentiating the remodeling zone from surrounding regions. Therefore, we took a different approach to characterize proteomic changes in the remodeling zone. Laser capture microdissection (LCM) was used to isolate narrow fiber cell regions (differentiating fiber cells, DF; remodeling zone, RZ; transition zone, TZ; inner cortex, IC) followed by LC-MS/MS to identify significant protein changes in the fiber cell plasma membrane fraction. Using a chromatographic separation step enabled fractionation of peptides based on their retention time, resulting in the identification of numerous proteins from subsequent MS/MS data. Our results show a correlation between the remodeling zone and a switch from intermediate filaments, composed of vimentin, to beaded filaments consisting of the filensin and phakinin heterodimer. Targeted, quantitative proteomic follow-up experiments confirmed significant changes in these proteins as well as other intermediate filament associated proteins (IFAPs). Using these methods, we successfully isolated and characterized major protein changes of the human lens remodeling zone. Further studies are required to explore the

functional significance of this disorganized region characteristic of human and other primate lenses.

## Overview

Unique structural and molecular features enable the transparent lens to perform its physiological function. Throughout life, the monolayer of lens epithelial cells differentiates into elongated lens fiber cells, which span from anterior to posterior of the lens.<sup>1</sup> Differentiating fiber cells lose all organelles and express high concentrations of lens-specific proteins including crystallins, AQP0, and beaded filament proteins filensin and phakinin.<sup>1-5</sup> An equatorial cross-section image of the lens reveals hexagonal fiber cells are tightly packed in order to reduce extracellular space and thus prevent light scattering.<sup>1</sup> Further into the lens, fiber cells develop interdigitations that enable communication and structural stability.<sup>1, 6, 7</sup> Ball and socket joints are localized to the sides of fiber cells, while longer interlocking protrusions are at the vertices or corners of cells. Disruption of cellular packing and intracellular connections results in abnormal light scattering or cataract, as demonstrated by the dysregulation of interdigitations in AQP0 and beaded filament knockout animals.<sup>7</sup> Thus, well-regulated differentiation and fiber cell organization is critical for normal lens physiology.

Recently, an uncharacteristically disorganized region was described in human lens outer cortex, termed the remodeling zone.<sup>8</sup> Immunofluorescence microscopy images showed the ordered differentiating human fiber cells undergo extreme morphological changes in the narrow (~20-40 µm wide) remodeling zone, followed by a return to classic hexagonal cell shape and organized fiber cell packing before compaction in the adult nucleus.<sup>9</sup> Figure 3.1 illustrates these distinct regions observed in the human lens outer cortex. Although clear cellular outlines and

radial cell columns cannot be easily distinguished in the remodeling zone, it is not a barrier to diffusion and cells within the zone are nucleated, indicating they can synthesize new protein.<sup>8, 9</sup>

The remodeling zone has only been observed in human lenses to date. Transmission electron microscopy (TEM) images revealed irregular cell shape and numerous ball-and-socket joints originating in the RZ.<sup>9</sup> These zones are very reproducible across a wide age range of human lenses, suggesting the remodeling zone is a regulated process of differentiation in human lens.<sup>8, 9</sup>

The function and molecular changes associated with the human-specific remodeling zone remain to be characterized.

The purpose of this study was to characterize the membrane-associated proteome of the remodeling zone and surrounding regions. Because the narrow remodeling zone is located ~100μm beneath the lens capsule and is approximately 20-40μm wide, we used laser capture microdissection (LCM) to collect tissue for spatially-resolved proteomics. We implemented a mass spectrometry-compatible fixation protocol that preserved the morphology of the lens outer cortex. Four regions were isolated for analysis: differentiating zone (DF), remodeling zone (RZ), transition zone (TZ), and inner cortex (IC). Shotgun proteomics revealed initial candidates for targeted protein quantification, and heavy-labeled peptides were synthesized as internal standards for multiple reaction monitoring (MRM) proteomics experiments. Our results highlight a shift from the intermediate filament vimentin to beaded filaments filensin and phakinin at the remodeling zone, and significant changes in other cytoskeletal proteins in these regions. Additional microscopy studies of macaque monkey lens, in collaboration with Dr. Joe Costello at UNC-Chapel Hill, provide evidence that the remodeling zone is also present in non-human primate lenses.

**Figure 3.1**

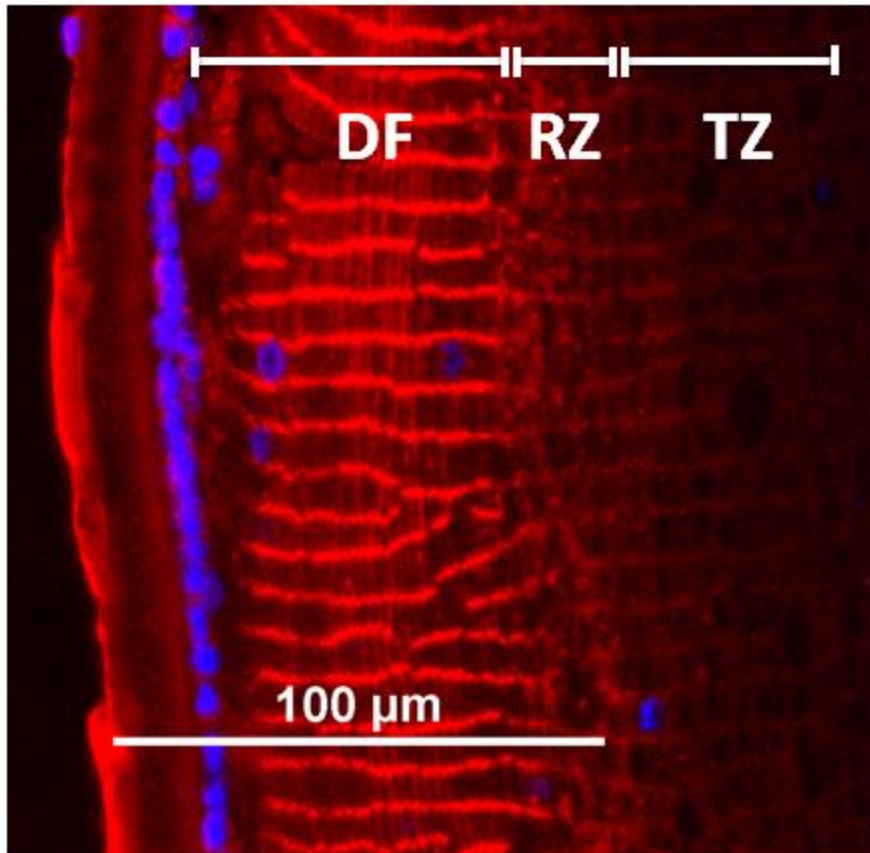


**Figure 3.1.** Confocal Microscopy Image of 22-Year Human Lens. Lens was ethanol-fixed and sectioned, followed by labeling with WGA-TRITC to highlight cell membranes. The ordered differentiating fiber cells (DF) rapidly become disordered in the remodeling zone (RZ) before radial cell columns are again visible in the transition zone (TZ).

## **Experimental Methods**

### *Materials*

Proteomics-grade porcine trypsin, ethanol, high-performance liquid chromatography (HPLC)-grade acetonitrile, formic acid, urea, phosphate buffered saline (PBS), sodium hydroxide, tris, and xylenes were purchased from Sigma-Aldrich (St. Louis, MO). Acetic acid, ammonium bicarbonate, dithiothreitol (DTT), chloroacetamide (ClAA), high-performance liquid chromatography (HPLC)-grade H<sub>2</sub>O with 0.1% formic acid, HPLC-grade H<sub>2</sub>O, and HPLC-grade acetonitrile with 0.1% formic acid were from Fisher Scientific (Pittsburgh, PA).

Frozen human lenses were obtained from the National Disease Research Interchange (Philadelphia, PA) and stored at -80°C until further use. Lenses used in this study were from individuals with no reported ocular pathology. Three lenses were analyzed in total: 21-year (M), 22-year (M), and 27-year (F). All other reagents were purchased from Sigma-Aldrich unless otherwise stated.

### *Sample Preparation and Laser Capture Microdissection*

Lenses were stored on wet ice during shipment and fixed upon arrival. A solution of 75:25 ethanol:acetic acid was used to lightly fix tissue while avoiding traditional formaldehyde crosslinking that can interfere with mass spectrometry experiments.<sup>10</sup> Whole lenses were fixed for 12 hours, manually cut in half across the equator using a razor blade, and fixed for an additional 12 hours. After fixation, lenses were processed and embedded in paraffin. Eight micron sections were collected using a Microm HM 325 Microtome (Thermo Scientific, Waltham, MA, USA) and allowed to dry on glass slides overnight at 37°C. Sections were

deparaffinized prior to labeling, using a series of xylene and alcohol washes (xylenes x 3, 100% ethanol, 95% ethanol, 70% ethanol, PBS – 5 minutes each).

To visualize the remodeling zone, lenses were incubated in wheat germ agglutinin-TRITC (Life Technologies, Eugene, OR, USA), using a 1mg/ml stock solution at 1:100 dilution for 2 hours, followed by three, 5-minute PBS washes. Sections for laser capture microdissection were coverslipped until dry to maintain a flat section. Sections used for confocal imaging were covered with VECTASHIELD mounting medium (Vector Laboratories, Burlingame, CA) and sealed with a coverslip.

Laser capture microdissection was performed on a PALM MicroBeam system (Carl Zeiss Microscopy, Thornwood, NY). Uncovered sections were visualized at 20x magnification using the fluorescence setting. Regions of interest were manually selected in the software, based on cellular morphology and measured distance from lens capsule. Tissue was cut in brightfield mode and catapulted into an Eppendorf cap containing 25 $\mu$ L HPLC-grade H<sub>2</sub>O. Microdissection was carried out until 2x10<sup>6</sup>  $\mu$ m<sup>2</sup> tissue was collected for each region to ensure approximately equal starting material. In total, tissue from four regions was collected: differentiating zone (DF), remodeling zone (RZ), transition zone (TZ), and inner cortex (IC). Tissue was then spun down into the tube and frozen for side-by-side membrane preparation of all four regions. For each lens, a total of three replicates of DF, RZ, TZ, and IC were collected for initial experiments. Three lenses were analyzed in total (21-, 22-, and 27-year).

#### *Membrane Preparation and Shotgun Proteomics*

Collected cells were washed to prepare membranes and to remove soluble proteins, as described previously.<sup>11</sup> Samples were first reduced (250mM DTT, 56°C for 1 hour) and

alkylated (55mM chloroacetamide, room temperature, 45 minutes in dark) before a series of washing and centrifugation steps to remove soluble proteins. The sample was vortexed and incubated for 30 minutes in homogenizing buffer containing 8M urea (50mM ammonium bicarbonate, 5mM EDTA, 10mM NaF, 1mM DTT, pH 8), followed by 20-minute centrifugation at 100,000 xg (Sorvall MTX150 Micro Ultracentrifuge, Thermo Scientific). The supernatant was removed and the pellet was saved and washed further using this procedure: homogenizing buffer containing 8M urea (3 times total), 0.1M NaOH (1 times), HPLC-grade H<sub>2</sub>O (1 time), 95% ethanol (1 time) and HPLC-grade H<sub>2</sub>O (3 times). Prior to trypsin digestion, the pellet was re-suspended in 50% TFE in 50mM ammonium bicarbonate, then diluted to 5% TFE before addition of 1µL of 0.1 µg/µL trypsin (Pierce) in a volume of 100µL. Digestion proceeded overnight at 37°C and was stopped with the addition of a small amount of neat formic acid.

For each tissue region, the entire sample was bomb-loaded onto a reverse-phase 360µm outer diameter (o.d.) x 100µm inner diameter (i.d.) capillary trap column (3cm length/5µm Jupiter C<sub>18</sub> beads, 300Å, Phenomenex) in-line with a 360µm o.d. x 100µm i.d. reverse-phase analytical column packed with 20cm of Jupiter C<sub>18</sub> beads (3 µm, 300 Å, Phenomenex) and equipped with a laser-pulled emitter tip. Using an Eksigent nanoLC-ultra, peptides were eluted at a flow rate of 500 nl/min over a 120-minute gradient of 0.1% formic acid in water (solvent A) and 0.1% formic acid in acetonitrile (solvent B). The gradient consisted of 2-10 %B in 20 minutes, 10-30 %B in 30 minutes, 30-95 %B in 15 minutes, 95 %B for 15 minutes, followed by equilibration at 2 %B. Gradient-eluted peptides were mass analyzed on an LTQ Velos Pro mass spectrometer with a nanoelectrospray ionization source (Thermo Scientific, San Jose, CA). The instrument was operated using a data-dependent method with dynamic exclusion enabled. Full scan (*m/z* 300-2000) spectra were acquired and the top 10 most abundant ions in each MS scan

were selected for fragmentation via collision-induced dissociation (CID). Tandem mass spectra were converted into DTA files using Scansifter and searched using a custom version of Sequest (Thermo Fisher Scientific) operating on the Vanderbilt ACCRE computing cluster. MS/MS spectra were searched against a concatenated forward and reverse (decoy) database containing the *Homo sapiens* subset of UniprotKB Sprot protein database ([www.uniprot.org](http://www.uniprot.org)). Additional search parameters included: trypsin enzyme specificity, monoisotopic masses were used for searching product ions, and oxidation of methionine, carbamidomethylation of cysteine, and phosphorylation of serine, threonine and tyrosine were allowed as variable modifications. Scaffold 4.3.4 (Proteome Software, Portland, OR, USA) was used to summarize and validate search results, where a minimum probability threshold of 95% was required for peptide identifications and data were filtered to a false-discovery rate (FDR) of <1% at the protein level. Peptide abundance in each region was compared using normalized spectral counts and a student's t-test was used to determine whether differences between the DF and RZ were statistically-significant ( $p < 0.05$ ).

### *Quantitative MRM*

Proteins with statistically-significant changes near the RZ were selected for further quantitation using multiple reaction monitoring (MRM), also called selected reaction monitoring (SRM).<sup>12</sup> A schematic of MRM is shown in Figure 3.2. Representative peptides for each protein were selected based on their appearance across multiple samples in the discovery phase of analysis. Heavy-labeled peptide standards were synthesized by jpt (SpikeTides TQL peptides, jpt, Berlin, Germany). Peptides contained isotopically-labeled terminal arginine or lysine residues (<sup>13</sup>C and <sup>15</sup>N) and a trypsin-cleavable C-terminal tag. Peptide standards were used to

generate a calibration curve, which confirmed a linear response between 1.5-100 fmol/ $\mu$ L (data not shown). Isotopically-labeled peptides were spiked into samples at approximately endogenous levels prior to digestion. Skyline software (University of Washington, MacCoss lab) was used to set up scheduled, targeted MRM methods and four to five MS/MS transitions were monitored per peptide. For targeted proteomics,  $6 \times 10^6 \mu\text{m}^2$  tissue was collected and membranes prepared as described. Prior to trypsin digestion, the pellet was re-suspended in 8M urea (100 mM Tris buffer, pH 8), then diluted with 100mM tris to 2M urea before addition of 1 $\mu$ L of 0.1  $\mu$ g/ $\mu$ L trypsin (mass spectrometry-grade, Pierce) in a total volume of 10 $\mu$ L. Digestion proceeded overnight at 37°C and was stopped with the addition of a small amount of neat formic acid.

The 10 $\mu$ L digest was transferred to a reduced-volume autosampler vial and 2.5 $\mu$ L sample per run was injected via autosampler and analyzed on a TSQ Vantage (Thermo Scientific, San Jose, CA). Results were viewed in Skyline software; transitions were summed to represent the intensity of endogenous peptides, which were normalized to the internal standard. For statistical analysis, a one-way ANOVA was performed with a post-hoc multiple comparison Tukey test using SPSS software (IBM, Armonk, New York, USA).

**Figure 3.2**

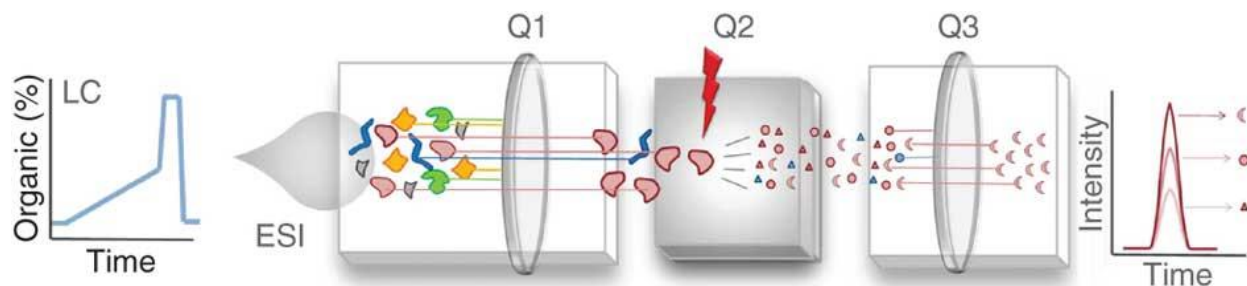


**Figure 3.2.** The Selected Reaction Monitoring Technique.

Molecular ions of a specific analyte are selected in Q1 and fragmented in Q2. ESI, electrospray ionization. Molecular ions of one or several contaminants are isolated and fragmented together. A specific fragment ion from the target analyte (transition) is selected in Q3 and guided to the detector. The number of target fragment ions is counted over time, resulting in an SRM trace for each transition. On the far right, cycles through three transitions, corresponding to three different fragments of the target analyte, and the corresponding three SRM traces are shown.

**Reprinted with permission from** Picotti P, Aebersold R. Selected reaction monitoring-based proteomics: workflows, potential, pitfalls and future directions. Nat Methods 2012;9:555-566.<sup>13</sup>

### *High-Resolution Lipid Imaging*

Ten micron sections of fresh frozen human lens were thaw-mounted onto gold MALDI target plates. Sections were washed to remove salts by immersing the plates in cold ammonium formate (50mM, pH 6.4) for 30 seconds (two washes total). For negative ion mode imaging, diaminonaphthalene (DAN) matrix was sublimated onto tissue using a home-built sublimation apparatus. The sandbath temperature was set to 120°C and sublimation proceeded for 15 minutes. Samples were analyzed on a Bruker RapiFlex Tissuetyper, over a mass range of 300-1600  $m/z$ , with a raster step size of 15 $\mu$ m. Laser parameters were optimized to minimize the laser footprint. Profilometry measurements were acquired after the imaging mass spectrometry experiment and show that minimal oversampling occurred (data not shown). For positive ion mode imaging, 2-mercaptobenzothiazole (2-MBT) matrix was applied by sublimation using a sandbath temperature of 110°C for 11 minutes. Samples were analyzed on a Bruker UltrafleXtreme TOF with a raster step size of 15 $\mu$ m over the mass range 400-1500  $m/z$ . Prior to analysis, both instruments were mass calibrated with red phosphorus.

### *Microscopy Analysis of Macaque Monkey Lens*

Macaque monkey lenses were obtained from euthanized animals in an unrelated study conducted at Vanderbilt University following institutional animal care guidelines through an approved tissue-sharing protocol. For confocal microscopy studies, lenses were fixed in 10% neutral-buffered formalin for 24 hours, followed by fixation in 4% paraformaldehyde for 48 hours. Lenses were cryoprotected by incubating in a series of sucrose solutions in PBS: 10% sucrose for 1 hour (RT), 20% sucrose for 1 hour (RT), and finally 30% sucrose overnight at 4°C. After this step, lenses were frozen and embedded in OCT prior to cryosectioning. Sections were

labeled with wheat germ agglutinin (WGA)-TRITC and DAPI to highlight membranes and nuclei. Images were collected on a confocal fluorescence microscope. For transmission electron microscopy experiments, lenses were fixed in 10% neutral buffered formalin for 24 hours during shipment to our collaborator Dr. Joe Costello at UNC-Chapel Hill. After an additional 48 hours fixation in 4% paraformaldehyde in cacodylate buffer, vibratome sections were processed for TEM as described.<sup>9</sup>

## Results

### *Lens Fixation for LCM and LC-MS/MS*

Although traditional fixation enables excellent antibody and lectin labeling of lens fiber cells, it causes protein-protein crosslinking that can interfere with conventional mass spectrometry proteomic analysis, which uses trypsin to cleave at basic residues.<sup>10</sup> Thus, we attempted alternative mass spectrometry-compatible fixation methods that could preserve cellular structure, including the lens capsule and outer cell layers. Fresh human lenses were lightly fixed in 75:25 ethanol:acetic acid for a total of 24 hours. WGA-labeled paraffin sections showed the outer cell layers remained intact and cellular morphology could be visualized. Confocal fluorescence microscopy images confirmed the presence of the remodeling zone approximately 100 $\mu$ m beneath the lens capsule (Figure 3.1). A return to more ordered cellular organization is visible in the transition zone where cellular compaction begins. A test section was used to ensure this fixation did not interfere with trypsin digestion and mass spectrometry (data not shown).

### *Shotgun Proteomics*

After light fixation and WGA labeling, lens sections were visualized on the LCM instrument using the fluorescence microscope setting. As shown in Figure 3.3, regions of interest were manually selected based on membrane morphology and distance from the capsule. Regions and approximate measurements included differentiating fiber cells (DF, outer fiber cell layers, 0 - 100  $\mu\text{m}$  from lens capsule); remodeling zone (RZ, 100-140  $\mu\text{m}$  from lens capsule); transition zone (TZ, 140-240  $\mu\text{m}$  from lens capsule); inner cortex (IC, 240  $\mu\text{m}$  and beyond). Several tests were performed to ensure enough material was collected for proteomic analysis (data not shown). We collected  $2 \times 10^6 \mu\text{m}^2$  per region, which is equivalent to approximately 80,000 fiber cell cross-sections based on average fiber cell diameter.<sup>14</sup> After each sample was prepared to isolate membrane-associated proteins and digested with trypsin, peptides were analyzed by LC-MS/MS. Shotgun proteomics results revealed a number of protein IDs, ranging from crystallins to cytoskeletal proteins (full protein list in Figure 3.4; 31 average protein IDs for 22-year lens analyzed). Compared to conventional tissue homogenization proteomics experiments, total spectral counts from our LCM samples are quite low due to the very small amount of tissue captured and prepared for proteomic analysis. Furthermore, although we analyzed the plasma membrane fraction, membrane proteins are not among the top peptides identified from our LCM experiments because of their low abundance and insolubility compared to lens crystallins and cytoskeletal proteins.

To identify proteins that were changing in the remodeling zone, we initially performed the student's t-test to compare peptide spectral counts between the DF and RZ regions. Statistically-significant changes were detected for the intermediate filament protein vimentin, which decreases by approximately 80% from the DF to the RZ (Figure 3.5) and decreases further

in the TZ and IC. A concurrent increase in the beaded filament proteins filensin and phakinin is observed at the RZ, suggesting a switch of intermediate filaments occurs near the remodeling zone. Other cytoskeletal proteins including periplakin also change significantly, while spectrins and several crystallins remained fairly constant across the regions analyzed. These results were used to develop a targeted mass spectrometry assay for more accurate quantitation of proteins of interest with significant changes at the remodeling zone.

**Figure 3.3**

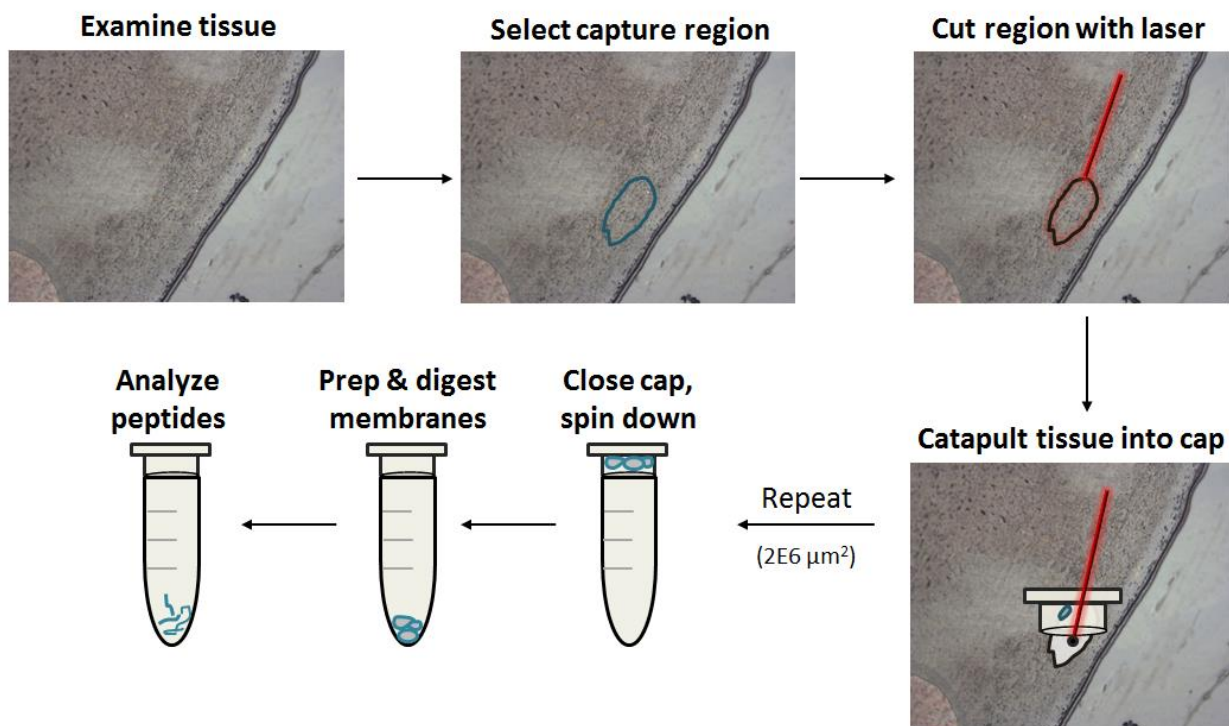


**Figure 3.3.** Summary of Laser Capture Microdissection (LCM) and LC-MS/MS Analysis.

Stained or labeled tissue is viewed on the LCM microscope and the desired capture region is manually outlined. The LCM laser is used to cut around the region, then pulsed to catapult the separated tissue into an Eppendorf cap containing water or buffer. This process is repeated until enough tissue has been collected from each region to obtain signal by LC-MS/MS. Tissue is spun down and washed with urea buffer, followed by subsequent washes and centrifugation steps, to enrich for plasma membranes. Finally, proteins are digested into peptides and analyzed by LC-MS/MS.

**Figure 3.4.** List of Protein IDs from Shotgun Proteomics, by Region

A. Differentiating Fiber Cells (DF)

UniProt AC	Protein	Average Spectral Counts
P60709	Actin, cytoplasmic	10
P02489	Alpha-crystallin A chain	101
P02511	Alpha-crystallin B chain	56
P04083	Annexin A1	6
P07355	Annexin A2	2
P53672	Beta-crystallin A2	3
P05813	Beta-crystallin A3	21
P53673	Beta-crystallin A4	48
P53674	Beta-crystallin B1	47
P43320	Beta-crystallin B2	107
P26998	Beta-crystallin B3	2
P22914	Beta-crystallin S	25
P80723	Brain acid soluble protein 1	7
P16152	Carbonyl reductase [NADPH] 1	6
P81605	Dermcidin	2
Q12934	Filensin	12
P04075	Fructose-bisphosphate aldolase A	2
P09972	Fructose-bisphosphate aldolase C	2
P47929	Galectin-7	2
P07315	Gamma-crystallin C	4
P07320	Gamma-crystallin D	7
P04406	Glyceraldehyde-3-phosphate dehydrogenase	2
P04792	Heat shock protein beta-1	8
P00338	L-lactate dehydrogenase A chain	2
O60437	Periplakin	3
Q13515	Phakinin	10
P00352	Retinal dehydrogenase 1	2
P04279	Semenogelin-1	9
Q02383	Semenogelin-2	5
P02768	Serum albumin	2
Q13813	Spectrin alpha chain, non-erythrocytic 1	3
Q01082	Spectrin beta chain, non-erythrocytic 1	2
P07437	Tubulin beta chain	4
P08670	Vimentin	37
O60281	Zinc finger protein 292	2

## B. Remodeling Zone (RZ)

<b>UniProt AC</b>	<b>Protein</b>	<b>Average Spectral Counts</b>
P62736	Actin, aortic smooth muscle	14
P60709	Actin, cytoplasmic	17
P02489	Alpha-crystallin A chain	155
P02511	Alpha-crystallin B chain	100
P05813	Beta-crystallin A3	29
P53673	Beta-crystallin A4	63
P53674	Beta-crystallin B1	73
P43320	Beta-crystallin B2	158
P26998	Beta-crystallin B3	3
P22914	Beta-crystallin S	28
P80723	Brain acid soluble protein 1	12
P16152	Carbonyl reductase [NADPH] 1	12
P81605	Dermcidin	2
Q12934	Filensin	41
P04075	Fructose-bisphosphate aldolase A	3
P09972	Fructose-bisphosphate aldolase C	4
P07315	Gamma-crystallin C	6
P07320	Gamma-crystallin D	13
P48637	Glutathione synthetase	4
P04406	Glyceraldehyde-3-phosphate dehydrogenase	6
P04792	Heat shock protein beta-1	10
Q86YZ3	Hornerin	4
P30301	Lens fiber major intrinsic protein	3
P00338	L-lactate dehydrogenase A chain	3
P30041	Peroxiredoxin-6	2
Q13515	Phakinin	22
Q99497	Protein DJ-1	4
P14618	Pyruvate kinase isozymes M1/M2	2
P00352	Retinal dehydrogenase 1	5
Q00796	Sorbitol dehydrogenase	2
Q13813	Spectrin alpha chain, non-erythrocytic 1	4
Q01082	Spectrin beta chain, non-erythrocytic 1	2
P08670	Vimentin	9

### C. Transition Zone (TZ)

<b>UniProt AC</b>	<b>Protein</b>	<b>Average Spectral Counts</b>
P60709	Actin, cytoplasmic	10
P02489	Alpha-crystallin A chain	141
P02511	Alpha-crystallin B chain	84
P06733	Alpha-enolase	2
P05813	Beta-crystallin A3	27
P53673	Beta-crystallin A4	56
P53674	Beta-crystallin B1	59
P43320	Beta-crystallin B2	115
P26998	Beta-crystallin B3	5
P22914	Beta-crystallin S	25
P80723	Brain acid soluble protein 1	10
P16152	Carbonyl reductase [NADPH] 1	8
P81605	Dermcidin	3
Q12934	Filensin	29
P04075	Fructose-bisphosphate aldolase A	3
P09972	Fructose-bisphosphate aldolase C	4
P07316	Gamma-crystallin B	2
P07315	Gamma-crystallin C	4
P07320	Gamma-crystallin D	10
P04406	Glyceraldehyde-3-phosphate dehydrogenase	6
P04792	Heat shock protein beta-1	6
Q86YZ3	Hornerin	5
P30041	Peroxiredoxin-6	2
Q13515	Phakinin	17
Q99497	Protein DJ-1	2
P00352	Retinal dehydrogenase 1	6
Q13813	Spectrin alpha chain, non-erythrocytic 1	2
P08670	Vimentin	2

D. Inner Cortex (IC)

<b>UniProt AC</b>	<b>Protein</b>	<b>Average Spectral Counts</b>
P60709	Actin, cytoplasmic	8
P02489	Alpha-crystallin A chain	119
P02511	Alpha-crystallin B chain	91
P05813	Beta-crystallin A3	49
P53673	Beta-crystallin A4	72
P53674	Beta-crystallin B1	137
P43320	Beta-crystallin B2	73
P26998	Beta-crystallin B3	2
P22914	Beta-crystallin S	62
P80723	Brain acid soluble protein 1	8
P16152	Carbonyl reductase [NADPH] 1	7
Q12934	Filensin	38
P04075	Fructose-bisphosphate aldolase A	3
P09972	Fructose-bisphosphate aldolase C	2
P07316	Gamma-crystallin B	19
P07315	Gamma-crystallin C	33
P07320	Gamma-crystallin D	16
P48637	Glutathione synthetase	5
P04406	Glyceraldehyde-3-phosphate dehydrogenase	9
P00338	L-lactate dehydrogenase A chain	2
P30041	Peroxiredoxin-6	2
Q13515	Phakinin	22
P00558	Phosphoglycerate kinase 1	2
Q99497	Protein DJ-1	3
P00352	Retinal dehydrogenase 1	15
P35237	Serpin B6	5
Q00796	Sorbitol dehydrogenase	2
Q13813	Spectrin alpha chain, non-erythrocytic 1	3
P29401	Transketolase	2

**Figure 3.5**

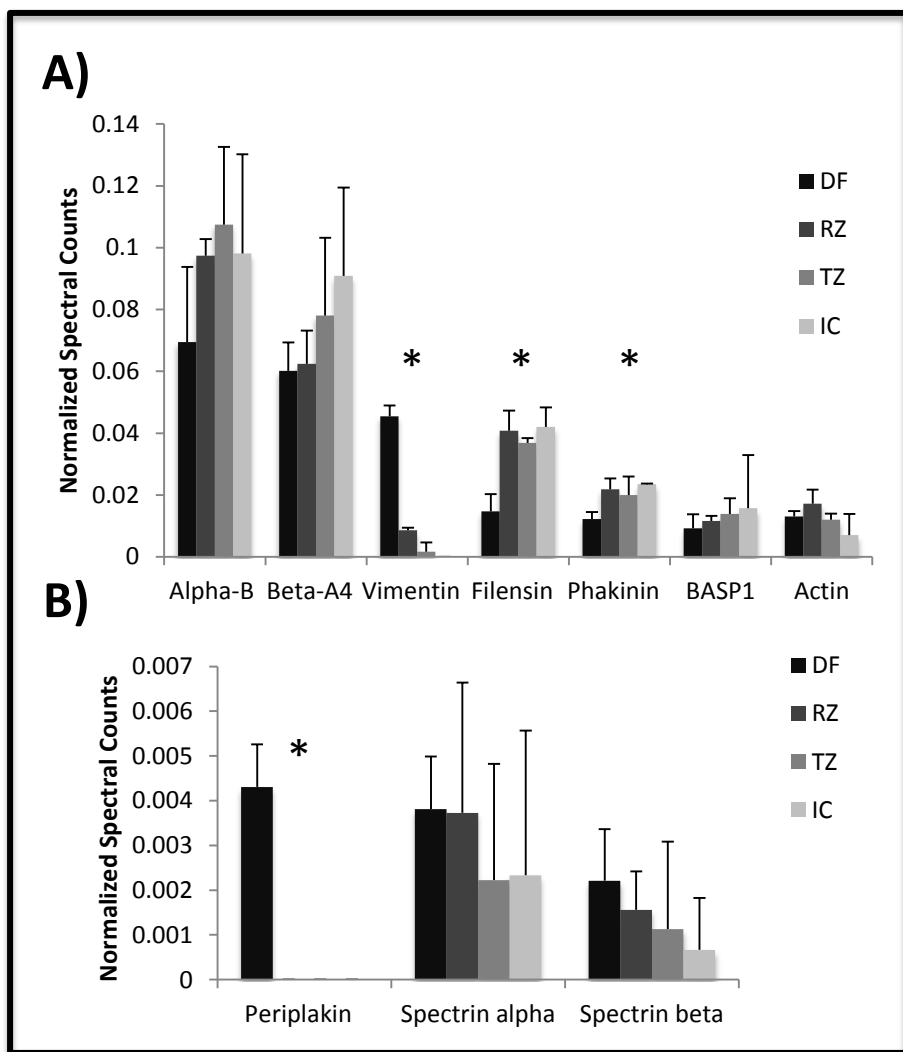


**Figure 3.5.** Shotgun Proteomics Results from a 22-Year Human Lens.

Three LC-MS/MS runs were averaged for each region. \* indicates a statistically-significant difference detected between the DF and RZ regions ( $p < 0.05$ ).

### *Quantitative MRM*

To more accurately quantify protein changes around the remodeling zone, we adopted a targeted proteomics strategy, using multiple reaction monitoring for protein quantitation. In this experiment, known concentrations of heavy-labeled isotopes for each peptide of interest are spiked into samples, which differ in mass from the endogenous peptide but share physiochemical properties and behave similarly in the instrument. Endogenous peptide concentrations can be calculated by taking a ratio of the endogenous peptide to its heavy-labeled counterpart, multiplied by the concentration of the heavy internal standard.

Using shotgun proteomics data, one or two representative peptides were chosen for each protein of interest. Peptides were selected based several criteria, including identification across several mass spectrometry runs and biological samples, absence of labile or modifiable residues like methionine or cysteine, and ideal peptide length for detection by mass spectrometry. Final peptide candidates were synthesized by jpt, containing heavy-labeled arginine or lysine residues and a C-terminal tag released by tryptic digestion. Calibration curve experiments were performed to determine the quantifiable range of the internal standards (data not shown) and the concentration of each internal peptide standard was optimized to reflect approximately endogenous conditions (Figure 3.6). For the final analysis, the 4 regions of interest were isolated from 3 separate lenses (21-, 22-, and 27-year). A larger amount of tissue ( $6 \times 10^6 \mu\text{m}^2$ ) was pooled for each region so technical replicates could be run via autosampler for each sample. A mix of heavy-labeled peptides was spiked in prior to sample digestion. An example of the transitions observed for an endogenous and heavy-labeled filensin peptide are shown in Figure 3.7. A schematic of the set-up for targeted quantitative proteomics, using a triple quadrupole instrument to selectively monitor precursor ions and peptide fragments using MRM, is shown in Figure 3.2.

**Figure 3.6, MRM Transitions Monitored**

		Precursor Mass	[M+2H] <sup>2+</sup>	Heavy Precursor Mass	Isotope [M+2H] <sup>2+</sup>	Transitions Monitored
<b>VIMENTIN (P08670)</b>		z				
51SLYASSPGGVYATR* <sub>64</sub>	2	1427.70	714.86	1437.71	719.86	y8, y9, y10, y12
295FADLSEAANR* <sub>304</sub>	2	1092.52	547.27	1102.53	552.27	b3, y5, y6, y8
<b>PERIAXIN (Q9BXM0)</b>						
56SLSLQEGDQLLSAR* <sub>69</sub>	2	1515.79	758.90	1525.80	763.91	y3, y8, y9, y10
<b>PERIPLAKIN (O60437)</b>						
1427LAALEQEEAEAR* <sub>1438</sub>	2	1328.66	665.34	1338.67	670.34	y5, y6, y7, y8
1447VVLQQDPQQAR* <sub>1457</sub>	2	1280.68	641.35	1290.69	646.35	y5, y6, y7, y8, y9
<b>BASP1 (P80723)</b>						
39ESEHQAAEPAEAK* <sub>52</sub>	2	1426.66	714.34	1434.67	718.34	y6, y8, y11, y11 <sup>2+</sup>
103APEQEQAAPGPAAGGEAPK* <sub>121</sub>	2	1774.85	888.43	1782.86	892.44	b8, y11, y12, y13
185ETPAATEAPSSTPK* <sub>198</sub>	2	1385.67	693.84	1393.68	697.85	y6, y8, y9, y12 <sup>2+</sup>
<b>FILENSIN (Q12934)</b>						
78LGELAGPEDALAR* <sub>90</sub>	2	1310.68	656.35	1320.69	661.35	b5, y7, y8, y9
240VELQAQTTLEQAIK* <sub>254</sub>	2	1671.90	836.96	1679.92	840.97	y8, y9, y10, y11
<b>PHAKININ (Q13515)</b>						
201AAEEEINSLYK* <sub>211</sub>	2	1265.61	633.81	1273.63	637.82	y5, y6, y7, y8
288VEAGALLQAK* <sub>297</sub>	2	998.58	500.30	1006.59	504.30	b2, y5, y7, y8

**Figure 3.6.** Precursor and Transition Masses Monitored for Endogenous and Heavy-Labeled Isotopes in MRM Runs.

**Figure 3.7**

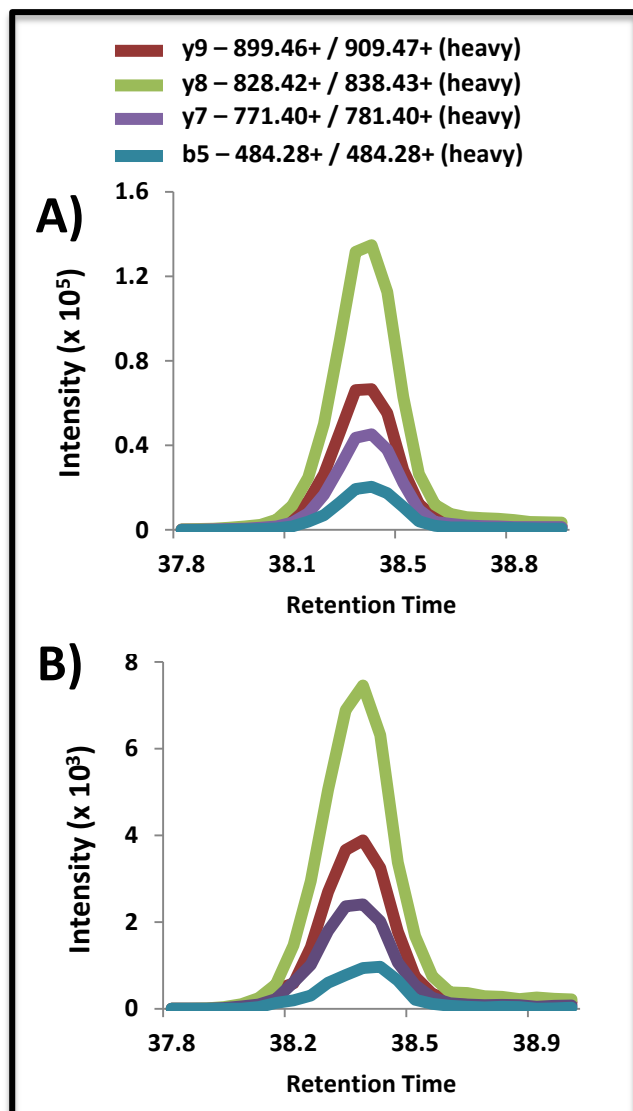


**Figure 3.7.** Transitions, or Peptide Fragmentation Patterns, Selected for Multiple Reaction Monitoring of a Filensin Tryptic Peptide ( $_{77}\text{LGELAGPEDALAR}_{89}$ ).

Precursor masses for endogenous ( $m/z$  656.35, +2) and heavy ( $m/z$  661.35, +2) peptides were monitored along with characteristic fragment transitions shown above. Relative intensity and retention time of heavy peptide standard transitions (A) are consistent with endogenous peptide (B).

Targeted, quantitative MRM results generally agreed with shotgun proteomics results, providing more confidence and better quantitation of small abundance changes between the four regions. Figure 3.8 shows the relative intensity of peptides quantified from 3 different lenses (two technical replicates per lens). Intensities are normalized to the region with the highest peptide concentration; other regions are expressed as a percentage of the highest value. Statistically-significant changes were determined using a one-way ANOVA with Tukey test. Both vimentin peptides decreased 80% from the DF to the RZ, in agreement with shotgun proteomics data, and continued to decrease in the TZ and IC (Figure 3.8A). Periplakin and periaxin follow similar trends, decreasing by 30-40% from DF to RZ and even further in the TZ (Figures 3.8B-C). Filensin and phakinin, which make up the beaded filament of the lens, increase at least two-fold at the remodeling zone and show slightly variable trends in the TZ, increasing again in the IC (Figure 3.8E). In Figure 3.8D, brain acid soluble protein 1 (BASP1) follows a similar trend, increasing at the remodeling zone with slightly less protein detected in the TZ and IC. Figure 3.9 shows the absolute quantitation of peptides between regions from 3 separate lenses, where fmol values calculated represent the peptide quantity in approximately  $2 \times 10^6 \mu\text{m}^2$  tissue collected. Despite some discrepancies in the absolute fmol calculated per lens, which could be due to differences in tissue thickness, the trends match very well among the three ages studied. ANOVA and Tukey test results for each peptide are displayed at the end of this chapter in Appendix A.

**Figure 3.8**

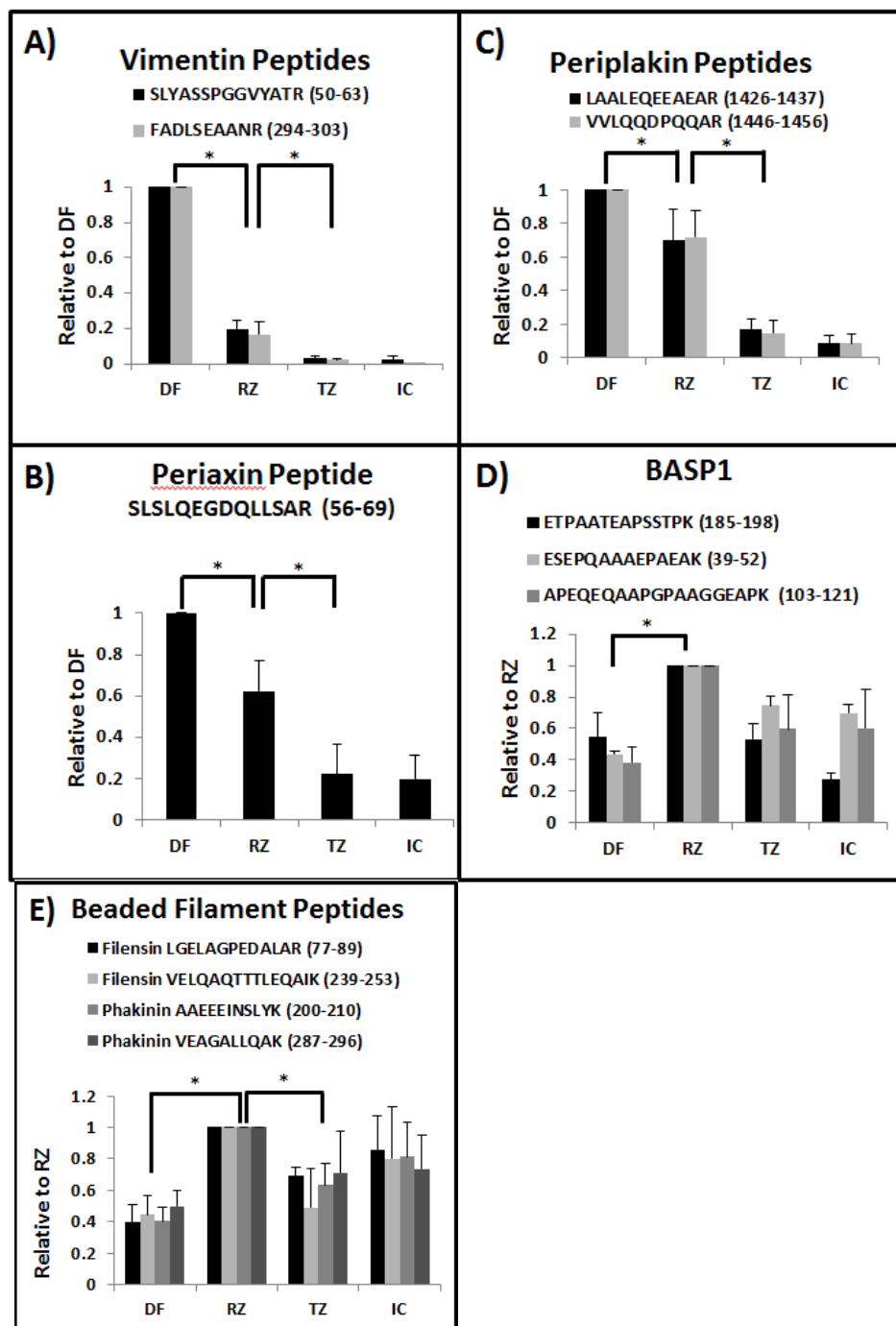


**Figure 3.8.** Quantitative Proteomics of Selected Lens Proteins. Each bar represents 6 measurements (2 technical replicates per lens, 3 lenses total: 21-, 22-, and 27-year). After calculating fmol values for each representative peptide, the region with the highest signal was set to “1” and other regions expressed as a fraction of that value. A one-way ANOVA with Tukey test was used to determine statistically-significant differences between regions. Brackets with (\*) indicate  $p < 0.05$ .

**Figure 3.9.** Absolute Quantitation of Cytoskeletal Peptides

A. Vimentin

		SLYASSPGGVYATR		FADLSEAANR	
		fmol	Std Dev	fmol	Std Dev
21-year	DF	198.73	5.59	23.15	0.55
	RZ	37.81	0.08	5.11	0.12
	TZ	5.99	0.28	0.76	0.02
	IC	2.36	0.35	0.15	0.02
22-year	DF	64.82	3.14	12.56	0.53
	RZ	9.64	0.01	0.90	0.05
	TZ	1.00	0.31	0.17	0.00
	IC	0.87	0.06	0.01	0.00
27-year	DF	29.29	0.05	4.08	0.01
	RZ	7.29	0.79	0.82	0.07
	TZ	1.40	0.22	0.09	0.00
	IC	1.34	0.29	0.01	0.00

B. Periaxin

		SLSLQEGDQLLSAR	
		fmol	Std Dev
21-year	DF	33.17	5.73
	RZ	16.39	1.96
	TZ	6.64	0.23
	IC	6.01	0.17
22-year	DF	3.12	0.19
	RZ	1.79	0.21
	TZ	0.23	0.15
	IC	0.24	0.01
27-year	DF	1.40	0.11
	RZ	1.12	0.18
	TZ	0.54	0.16
	IC	0.46	0.02

### C. Periplakin

		LAALEQEEAEAR		VVLQQDPQQAR	
		fmol	Std Dev	fmol	Std Dev
21-year	DF	0.72	0.03	1.17	0.08
	RZ	0.62	0.00	1.04	0.06
	TZ	0.16	0.02	0.23	0.02
	IC	0.09	0.01	0.13	0.01
22-year	DF	0.26	0.03	0.39	0.01
	RZ	0.18	0.04	0.27	0.04
	TZ	0.03	0.02	0.03	0.03
	IC	0.01	0.01	0.01	0.01
27-year	DF	0.20	0.02	0.28	0.02
	RZ	0.11	0.03	0.17	0.02
	TZ	0.03	0.00	0.05	0.00
	IC	0.02	0.01	0.03	0.02

### D. BASP1

		ESEPQAAAEPAEA		APEQEQAAPGPAAGGEAP		ETPAATEAPSSTP	
		K	K	K	K	K	K
		fmol	Std Dev	fmol	Std Dev	fmol	Std Dev
21-year	DF	1.27	0.11	0.51	0.03	3.21	0.03
	RZ	2.80	0.02	1.28	0.03	5.81	0.01
	TZ	1.58	0.00	0.64	0.01	2.42	0.16
	IC	1.36	0.03	0.43	0.07	1.81	0.09
22-year	DF	0.78	0.01	0.43	0.20	1.43	0.00
	RZ	1.34	0.17	0.96	0.22	1.96	0.06
	TZ	1.20	0.11	0.43	0.05	1.26	0.08
	IC	0.86	0.08	0.74	0.05	0.46	0.09
27-year	DF	0.36	0.10	0.13	0.04	0.78	0.00
	RZ	1.42	0.23	0.50	0.07	2.22	0.27
	TZ	1.09	0.19	0.42	0.04	1.18	0.06
	IC	1.35	0.02	0.34	0.02	0.62	0.08

E. Filensin

		LGELAGPEDALAR		VELQAQTTLEQAIK	
		fmol	Std Dev	fmol	Std Dev
21-year	DF	56.00	2.34	2832.85	239.12
	RZ	105.78	2.38	5044.58	1080.66
	TZ	65.75	2.59	2007.54	147.89
	IC	83.68	2.82	3628.20	195.39
22-year	DF	17.75	0.17	56.22	0.62
	RZ	47.10	0.44	161.94	6.29
	TZ	34.22	0.09	45.71	4.89
	IC	30.94	0.43	80.33	7.32
27-year	DF	12.54	0.09	32.96	2.82
	RZ	42.64	0.82	82.29	2.63
	TZ	30.84	1.96	63.19	0.99
	IC	47.80	0.60	95.59	10.37

F. Phakinin

		AAEEEINSLYK		VEAGALLQAK	
		fmol	Std Dev	fmol	Std Dev
21-year	DF	131.00	3.05	30.80	0.41
	RZ	291.82	4.41	72.65	13.22
	TZ	170.23	0.47	40.46	3.71
	IC	191.75	20.26	41.64	6.29
22-year	DF	22.49	0.23	7.09	0.22
	RZ	48.90	0.23	11.49	0.23
	TZ	25.81	1.65	6.36	0.22
	IC	35.14	1.39	7.24	0.05
27-year	DF	11.14	0.46	3.71	0.48
	RZ	36.95	1.56	8.32	0.38
	TZ	29.08	0.65	8.47	0.04
	IC	39.29	1.50	8.16	0.21

### *High-Resolution Lipid Imaging*

Morphological changes to fiber cells in the lens remodeling zone could be influenced by multiple molecules within the cell, including proteins and lipids. It is possible that the composition of the plasma membrane undergoes changes during fiber cell differentiation, which includes the extreme morphological changes in the remodeling zone. To examine whether lipid composition was affected during the extreme disorganization in this region, we performed high resolution lipid imaging experiments on human lens.

Positive ion mode (Figure 3.10) and negative ion mode (Figure 3.11) imaging data revealed distinct patterns for putative lipid signals in human lens. These images demonstrate successful lipid imaging at high spatial resolution ( $15\mu\text{m}$ ). Although no signals were observed exclusively in the remodeling zone, several  $m/z$  signals show an increase in abundance just beneath the lens capsule (Figure 3.10C and Figure 3.11C). Although some tentative IDs were assigned by accurate mass (see legends for Figures 3.10 and 3.11), these signals have not been definitively identified by MS/MS. Thus, further work is needed to characterize lipid changes in differentiating fiber cells of the very outer cortex. Optimizing sample preparation (including washing and matrix application) and confirming lipid identification by MS/MS will improve image quality and provide a better understanding of changes in lipid distribution throughout the lens. Improving sensitivity may highlight specific signals associated with the lens RZ.

**Figure 3.10**

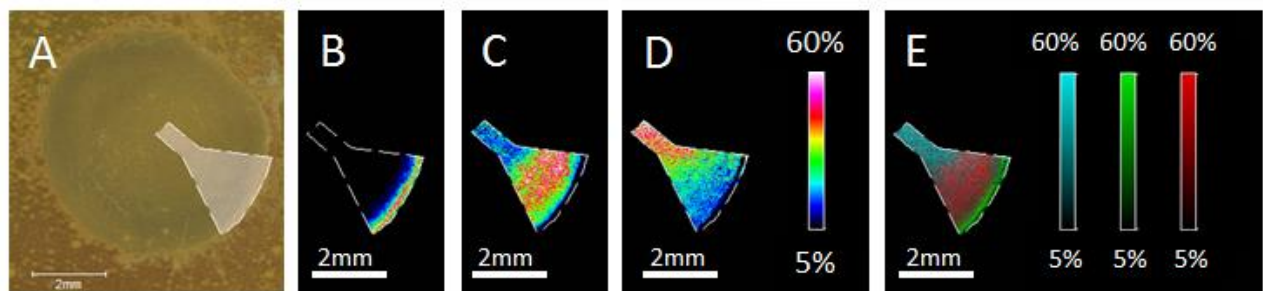


**Figure 3.10.** Lipid Imaging of 18-Year Human Lens at  $15\mu\text{m}$  Spatial Resolution in Positive Ion Mode.

(A) Optical image of lens highlighting the imaged region. Different signals in positive ion mode show distinct outer cortical (B,  $m/z$  734.570: tentative ID PC 16:0/16:0, 1.36 ppm error), inner cortical (C,  $m/z$  705.590: tentative ID SM(d18:0)/16:0, 1.42 ppm error), and nuclear (D,  $m/z$  630.94, unknown signal) distribution. (E) Overlay. Scale bar =  $1000\mu\text{m}$ . Image was acquired on a Bruker UltrafleXtreme TOF MS.

**Figure 3.11**

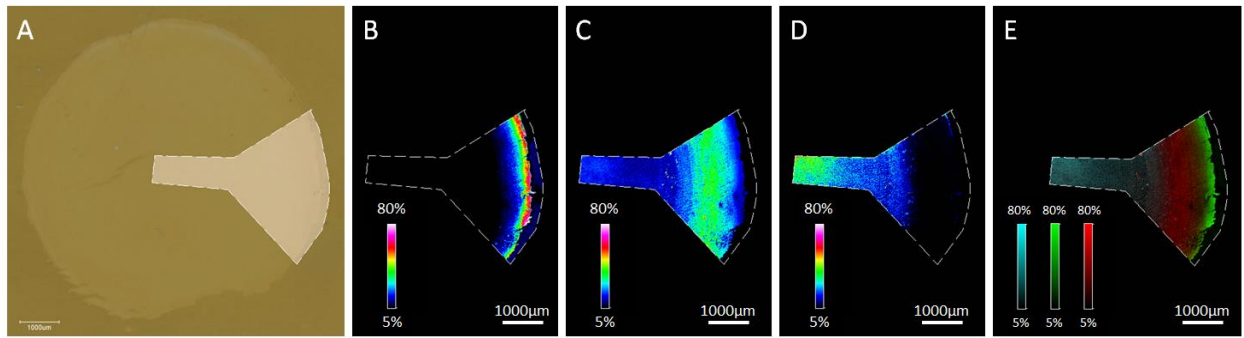


**Figure 3.11.** Lipid Imaging of 18-Year Human Lens at  $15\mu\text{m}$  Spatial Resolution in Negative Ion Mode.

(A) Optical image of lens highlighting the imaged region. Different signals in negative ion mode show distinct outer cortical (B,  $m/z$  780.5), inner cortical (C,  $m/z$  616.467: tentative ID CerP(d18:1)/16:0, 6ppm error), and nuclear (D,  $m/z$  862.625: tentative ID LacCer(d18:0)/16:0, 1.15 ppm error) distribution. (E) Overlay. Scale bar =  $1000\mu\text{m}$ . Image was acquired on a Bruker RapiFlex Tissuetyper TOF MS.

### *Microscopy Analysis of Macaque Monkey Lens*

By establishing a collaboration with laboratories using the animal facilities at Vanderbilt University, we were able to collect unused eyes from previously euthanized animals. This enabled us to study the lens of macaque (*Macaca mulatta*) monkey, a non-human primate, in order to establish whether the remodeling zone is indeed a human-specific phenomenon. As shown in Figure 3.12, WGA-TRITC labeling reveals these macaque lenses display a very similar disruption of fiber cell organization as seen in human lens. In macaque lens, this morphologically-distinct region is localized is approximately 100 $\mu$ m beneath the lens capsule and nuclei are still observed. Furthermore, our imaging studies of tree shrew lens, a closely related but non-primate mammal, did not reveal a remodeling zone in this species (Figure 3.13). Follow-up TEM studies, in collaboration with Dr. Joe Costello, revealed membrane blebbing and the origination of ball-and-socket joints in the remodeling zone of these macaque lenses.<sup>15</sup> Based on these studies, we concluded that the macaque lens remodeling zone shares the same features observed in human lens, indicating it could be a primate-specific phenomenon.

**Figure 3.12**

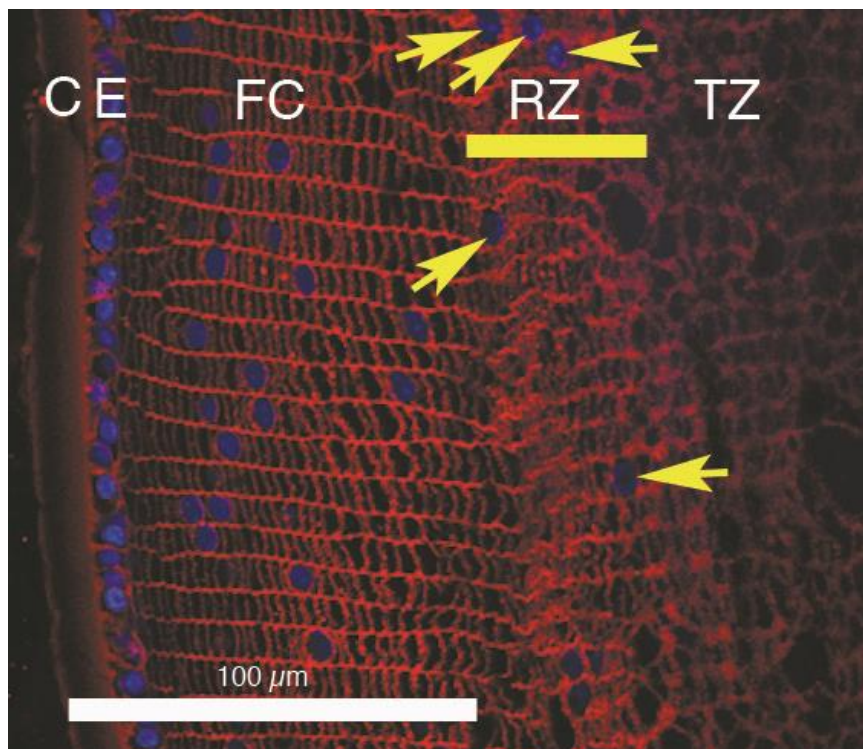


**Figure 3.12.** Confocal Microscopy of a Macaque Monkey Lens Labeled with WGA-TRITC (red) and DAPI (blue). The hexagonal differentiating fiber cells (FC) in the very outer cortex are arranged in radial cell columns and still contain nuclei. Approximately 100 $\mu$ m beneath the lens capsule (C) and epithelium (E), cell borders become indistinguishable in the remodeling zone (RZ). Yellow arrowheads indicate cell nuclei are still present in this region. Beyond, in the transition zone (TZ), no nuclei are present and cells return to a more ordered organization.

*Adapted with permission from* Costello MJ, Mohamed A, Gilliland KO, Wenke JL, Schey KL. Quantitative Morphology of the Remodeling Zone in Non-Human Primate Lenses. Poster presented at the annual Association for Research in Vision and Ophthalmology conference. Denver, CO; 2015.<sup>15</sup>

**Figure 3.13**

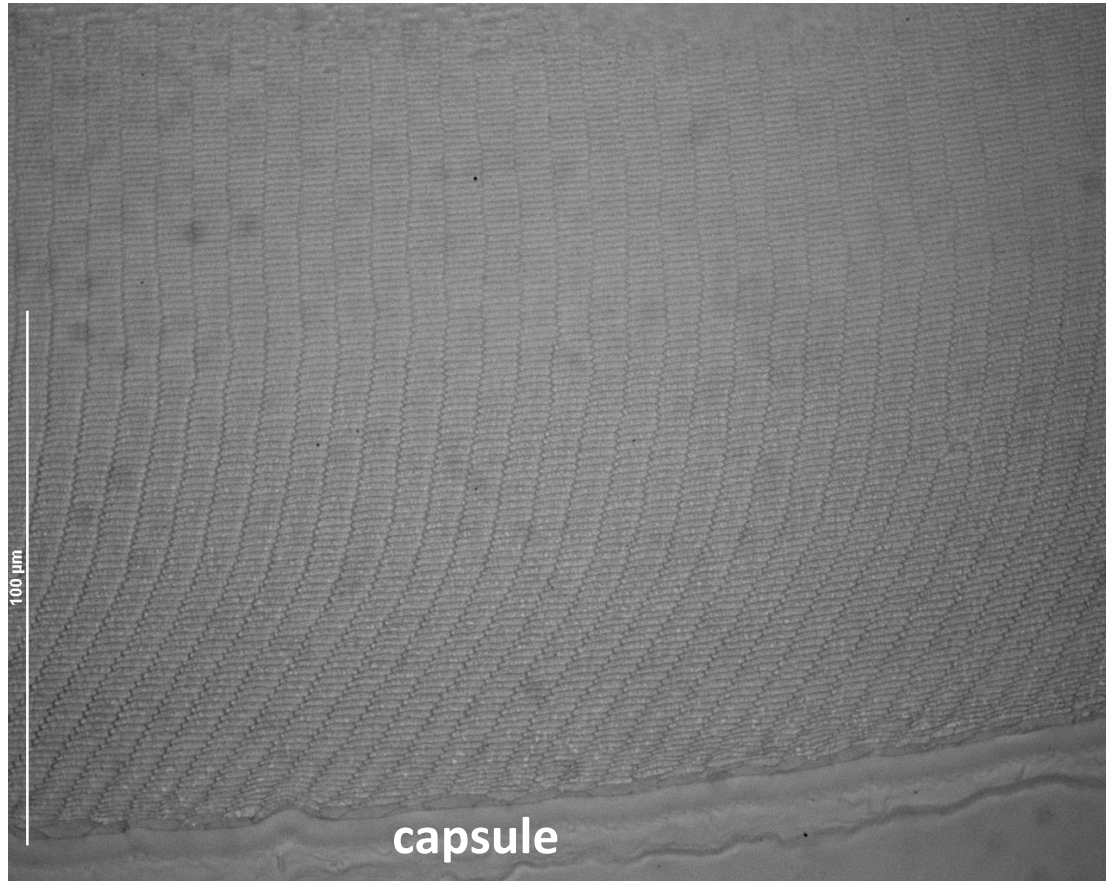


**Figure 3.13.** Brightfield Microscopy of a Tree Shrew Lens.

Fiber cells throughout the cortex have a regular, hexagonal appearance and are ordered in radial cell columns. Even 150  $\mu\text{m}$  beneath the lens capsule, no morphological changes can be observed, although cells do become more compact.

**Figure 3.14**

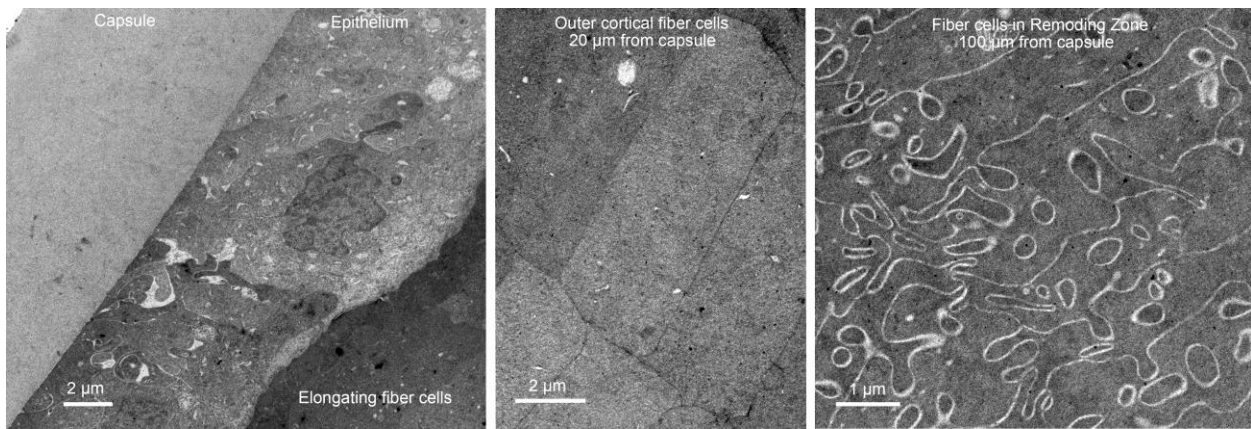


**Figure 3.14.** Transmission Electron Microscopy (TEM) of a Macaque Monkey Lens.

Fiber cells in the outer cortex have smooth cell borders and ordered arrangement (middle panel). Deeper into the lens, in the macaque remodeling zone, fiber cell borders cannot be distinguished and ball-and-socket joints between neighboring cells appear as circular blebs in the middle of cells or interdigitations at the edge of cells.

*Adapted with permission from* Costello MJ, Mohamed A, Gilliland KO, Wenke JL, Schey KL. Quantitative Morphology of the Remodeling Zone in Non-Human Primate Lenses. Poster presented at the annual Association for Research in Vision and Ophthalmology conference. Denver, CO; 2015.<sup>15</sup>

## Discussion

The combination of laser capture microdissection and LC-MS/MS has been used previously to analyze differences in the cortical and nuclear lens membrane proteome.<sup>11</sup> Here, we isolated extremely narrow regions (20-30 $\mu$ m) of tissue for quantitative proteomic analysis of the human lens outer cortex. These techniques enable spatially-resolved proteomics of regions that cannot be separated by manual dissection. Our strategy was to focus on membrane-associated proteins due to the extreme morphological changes of the plasma membrane in the remodeling zone.<sup>8, 9</sup> Although we enriched for the plasma membrane fraction, the majority of proteins detected by proteomic analysis were crystallins and cytoskeletal proteins, likely due to their abundance and reported association with the plasma membrane, even after treatment with urea.<sup>4, 16-18</sup> Based on these results, we could not assess membrane protein changes and instead focused on cytoskeletal proteins. Targeted MRM enabled accurate, absolute quantitation of peptides in these regions, even those present at low levels.

Intermediate filaments are a highly conserved family of cytoskeletal proteins that can be organized into several classes.<sup>19</sup> Immunohistochemical studies indicate vimentin, a major type III intermediate filament protein, is expressed in the lens epithelium and fiber cells, although the expression pattern changes based on lens age and region.<sup>4, 20</sup> Our results indicate vimentin is most abundant in the very outer fiber cells of the DF region, dropping off rapidly in the RZ and further into the lens. Because we analyzed the plasma membrane fraction, this decrease in vimentin signal at the RZ could be due to either reduced vimentin expression, increased solubility of the protein, or decreased association with the plasma membrane. It is possible that loss of vimentin in the RZ is due to a shift from membrane to cytoplasm, which has been documented in the literature.<sup>20</sup> Studies of adult mouse lens show membrane-specific vimentin

localization in outer cortical fibers, while vimentin antibody labeling becomes cytoplasmic and membranous further into the lens before signal is lost around the region of nuclei loss.<sup>20</sup> Similar labeling patterns have also been documented in bovine lens.<sup>21</sup> Furthermore, loss of vimentin antibody labeling has been correlated with nuclei loss in mouse lens.<sup>21</sup> Because RZ cells are still nucleated, our results suggest the drop in vimentin signal could be due to changes in solubility or membrane association.<sup>22</sup> Deeper into the lens cortex, vimentin is known to be cleaved, which could affect solubility and detection by both immunohistochemistry and mass spectrometry. Phosphorylation of vimentin is known to induce depolymerization of intermediate filaments, although this modification was not detected in our studies. Although vimentin knockout does result in any notable phenotype, vimentin overexpression causes cataract, suggesting that proper expression and regulation of vimentin is critical for lens clarity.<sup>23-25</sup>

The lens contains another divergent intermediate filament called the beaded filament. Filensin and phakinin are lens-specific proteins that form a heterodimer to make 6-8 nm beaded filaments.<sup>4</sup> Our results indicate filensin and phakinin increase significantly from the DF to the RZ, while vimentin decreases. The switch from vimentin intermediate filaments to lens-specific beaded filaments has been documented in several species including bovine and mouse.<sup>21, 26</sup> The control of these two intermediate filament systems appears to be independently modulated during fiber cell differentiation, as beaded filament expression is detected before vimentin labeling is lost.<sup>21</sup> Adult mouse lenses labeled with anti-filensin antibody reveal membranous labeling in the outer cortex, followed by membranous and cytoplasmic labeling further into the nucleated lens fiber cells.<sup>20</sup> However, filensin is not present in developing embryonic fiber cells until after elongation has progressed, suggesting it plays a role in lens organization after cells have begun differentiation.<sup>20</sup> Filensin and phakinin have also been shown to undergo truncation deeper into

the lens.<sup>27</sup> Our data show a dramatic increase in beaded filaments associated with the plasma membrane in the remodeling zone. The decrease in signal from RZ to TZ could be due to several factors, including altered solubility or membrane association. The functional consequences of beaded filament increase in the RZ have not been established. However, TEM studies indicate ball and socket joints arise in the RZ,<sup>9</sup> and knockout studies indicate beaded filaments are critical for maintaining interdigitations and long-range order of lens fiber cells.<sup>26</sup> Therefore, filensin and phakinin may become more associated with the membrane to establish interlocking domains and a beaded filament system that is maintained further into the lens cortex.

Periaxin and periplakin decrease from the RZ to the IC, similar to vimentin. Periaxin is localized at the plasma membrane, concentrated mostly at tricellular junctions where beaded filaments and vimentin labeling also occur.<sup>28</sup> Periaxin is critical for hexagonal geometry and membrane stabilization, perhaps functioning as a scaffolding protein in lens.<sup>28</sup> Periplakin, an IF-associated protein (IFAP), has been shown to bind both intermediate filaments and beaded filaments, directly interacting with vimentin and phakinin.<sup>29</sup> Periplakin and periaxin are also part of the EPPD (ezrin, periaxin, periplakin, desmoyokin) junction complex in lens.<sup>30</sup> Although their roles are not well understood, both periaxin and periplakin could anchor intermediate filaments to the plasma membrane through protein-protein interactions. AQP0 has been demonstrated to interact with beaded filaments, but AQP0 did not pull down with periplakin-BF complexes in previous studies, suggesting there may be another protein anchor connecting periplakin and BF to the plasma membrane.<sup>29</sup> Changes in protein-protein interaction, i.e. between periplakin and vimentin, could alter intermediate filament attachment to the plasma membrane, enabling cytoskeletal deformation and thus influencing membrane shape in the RZ. Actin polymerization could also be driving the formation of cellular interdigitations that originate in the remodeling

zone, as branching F-actin and the clathrin/AP-2 complex were shown to associate with interlocking domains in rat and monkey lenses.<sup>31</sup> Although we do not detect major changes in actin or clathrin abundance in our studies, their involvement cannot be ruled out. It is possible that changes in actin polymerization or interactions with other proteins are important but remain undetected in our quantitative proteomics studies. Additional work is required to understand how these proteins might be involved in membrane reorganization in the remodeling zone.

Although the switch from vimentin to beaded filaments has been documented in lens, this work is the first to show a rapid intermediate filament change associated with the human lens remodeling zone. Our proteomics results do not definitively prove that the intermediate filament switch is responsible for the morphological changes of the remodeling zone, but suggest the involvement of beaded filaments in establishing the ball and socket joints that originate in the remodeling zone.<sup>9</sup> Intermediate filaments can serve as mechanical support and scaffolding for membrane-associated proteins. Changes to the intermediate filament system could allow remodeling of the plasma membrane before the fiber cells return to a more ordered arrangement in the transition zone.

The function of the remodeling zone remains to be determined. In collaboration with Dr. Joe Costello, our work is the first to demonstrate the presence of the remodeling zone in macaque lens, a non-human primate, suggesting this is a primate-specific phenomenon.<sup>15</sup> Additional studies were performed on lenses from the tree shrew, which descends from the same grandorder (Euarchonta) as primates but is in the Scandentia family. No remodeling zone was observed in the closely related non-primate tree shrew species, suggesting this could be a divergent evolutionary trait. Perhaps accommodation in long-lived primates requires more extensive preparation of interdigitations between lens fiber cells. Future work should examine

human lenses with cataract-causing mutations in beaded filament genes to determine whether the formation of the remodeling zone is affected.

## **Conclusions**

Using spatially-resolved proteomics, we characterized protein changes in the narrow remodeling zone and surrounding regions of the human lens outer cortex. Intermediate filaments switch from vimentin to beaded filaments in this region, with changes in other IFAPs, suggesting involvement of the cytoskeleton and associated proteins in the dramatic membrane remodeling in the RZ. Consistent quantitative results between three separate lenses suggest the RZ region is part of a tightly-regulated differentiation process in human lens. Future work is necessary to characterize the function and necessity of the RZ for normal human and primate lens physiology.

## References

1. Mathias RT, Rae JL, Baldo GJ. Physiological properties of the normal lens. *Physiol Rev* 1997;77:21-50.
2. Wride MA. Lens fibre cell differentiation and organelle loss: many paths lead to clarity. *Philos Trans R Soc Lond B Biol Sci* 2011;366:1219-1233.
3. Bassnett S. Lens organelle degradation. *Exp Eye Res* 2002;74:1-6.
4. FitzGerald PG. Lens intermediate filaments. *Experimental Eye Research* 2009.
5. Schey KL, Wang Z, Wenke JL, Qi Y. Aquaporins in the eye: expression, function, and roles in ocular disease. *Biochim Biophys Acta* 2014;1840:1513-1523.
6. Zampighi G, Simon SA, Robertson JD, McIntosh TJ, Costello MJ. On the structural organization of isolated bovine lens fiber junctions. *J Cell Biol* 1982;93:175-189.
7. Lo WK, Biswas SK, Brako L, Shiels A, Gu S, Jiang JX. Aquaporin-0 targets interlocking domains to control the integrity and transparency of the eye lens. 2014;55:1202-1212.
8. Lim JC, Walker KL, Sherwin T, Schey KL, Donaldson PJ. Confocal microscopy reveals zones of membrane remodeling in the outer cortex of the human lens. *Invest Ophthalmol Vis Sci* 2009;50:4304-4310.
9. Costello MJ, A. M, Gilliland KO, Fowler WC, Johnsen S. Ultrastructural analysis of the human lens fiber cell remodeling zone and the initiation of cellular compaction. *Exp Eye Res* 2013;116:411-418.
10. Sompuram SR, Vani K, Messana E, Bogen SA. A molecular mechanism of formalin fixation and antigen retrieval. *Am J Clin Pathol* 2004;121:190-199.
11. Wang Z, Han J, Schey KL. Spatial differences in an integral membrane proteome detected in laser capture microdissected samples. *J Proteome Res* 2008;7:2696-2702.
12. Gerber SA, Rush J, Stemman O, Kirschner MW, Gygi SP. Absolute quantification of proteins and phosphoproteins from cell lysates by tandem MS. *Proc Natl Acad Sci U S A* 2003;100:6940-6945.
13. Picotti P, Aebersold R. Selected reaction monitoring-based proteomics: workflows, potential, pitfalls and future directions. *Nat Methods* 2012;9:555-566.
14. Taylor VL, al-Ghoul KJ, Lane CW, Davis VA, Kuszak JR, Costello MJ. Morphology of the normal human lens. *Invest Ophthalmol Vis Sci* 1996;37:1396-1410.

15. Costello MJ, Mohamed A, Gilliland KO, Wenke JL, Schey KL. Quantitative Morphology of the Remodeling Zone in Non-Human Primate Lenses. *Poster presented at the annual Association for Research in Vision and Ophthalmology conference*. Denver, CO; 2015.
16. Su SP, McArthur JD, Friedrich MG, Truscott RJ, Aquilina JA. Understanding the alpha-crystallin cell membrane conjunction. *Mol Vis* 2011;17:2798-2807.
17. Friedrich MG, Truscott RJ. Membrane association of proteins in the aging human lens: profound changes take place in the fifth decade of life. *Invest Ophthalmol Vis Sci* 2009;50:4786-4793.
18. Wang Z, Han J, David LL, Schey KL. Proteomics and phosphoproteomics analysis of human lens fiber cell membranes. *Invest Ophthalmol Vis Sci* 2013;54:1135-1143.
19. Steinert PM, Roop DR. Molecular and cellular biology of intermediate filaments. *Annu Rev Biochem* 1988;57:593-625.
20. Blankenship TN, Hess JF, FitzGerald PG. Development- and differentiation-dependent reorganization of intermediate filaments in fiber cells. *Invest Ophthalmol Vis Sci* 2001;42:735-742.
21. Sandilands A, Prescott AR, Carter JM, et al. Vimentin and CP49/filensin form distinct networks in the lens which are independently modulated during lens fibre cell differentiation. *J Cell Sci* 1995;108:1397-1406.
22. Alizadeh A, Clark J, Seeberger T, Hess J, Blankenship T, FitzGerald PG. Characterization of a mutation in the lens-specific CP49 in the 129 strain of mouse. *Invest Ophthalmol Vis Sci* 2004;45:884-891.
23. Colucci-Guyon E, Portier MM, Dunia I, Paulin D, Pournin S, Babinet C. Mice lacking vimentin develop and reproduce without an obvious phenotype. *Cell* 1994;79:679-694.
24. Capetanaki Y, Smith S, Heath JP. Overexpression of the vimentin gene in transgenic mice inhibits normal lens cell differentiation. *J Cell Biol* 1989;109:1653-1664.
25. Bloemendal H, Raats JM, Pieper FR, Benedetti EL, Dunia I. Transgenic mice carrying chimeric or mutated type III intermediate filament (IF) genes. *Cell Mol Life Sci* 1997;53:1-12.
26. Yoon KH, Blankenship T, Shibata B, Fitzgerald PG. Resisting the effects of aging: a function for the fiber cell beaded filament. *Invest Ophthalmol Vis Sci* 2008;49:1030-1036.
27. Wang Z, Obidike JE, Schey KL. Posttranslational modifications of the bovine lens beaded filament proteins filensin and CP49. *Invest Ophthalmol Vis Sci* 2010;51:1565-1574.

28. Maddala R, Skiba NP, Lalane Rr, Sherman DL, Brophy PJ, Rao PV. Periaxin is required for hexagonal geometry and membrane organization of mature lens fibers. *Dev Biol* 2011;357:179-190.
29. Yoon KH, FitzGerald PG. Periplakin interactions with lens intermediate and beaded filaments. *Invest Ophthalmol Vis Sci* 2009;50:1283-1289.
30. Straub BK, Boda J, Kuhn C, et al. A novel cell-cell junction system: the cortex adhaerens mosaic of lens fiber cells. *J Cell Sci* 2003;116:4985-4995.
31. Zhou CJ, Lo WK. Association of clathrin, AP-2 adaptor and actin cytoskeleton with developing interlocking membrane domains of lens fibre cells. *Exp Eye Res* 2003;77:423-432.

## **Chapter IV – Conclusions and Perspectives**

### **Contributions and Conclusions**

The aim of my work was to spatially characterize changes to human lens membrane-associated proteins based on fiber cell age and differentiation. At the tissue level, MALDI IMS was used to map age-related changes to AQP0 protein, revealing new information about AQP0 deamidation and fatty acid acylation. Zooming in on the lens outer cortex, LCM was used to isolate narrow regions of lens fiber cells to characterize proteomic changes in the morphologically-distinct remodeling zone. Quantitative proteomics showed the switch from intermediate filaments to beaded filaments occurs at the remodeling zone. Here, I summarize my findings and discuss how this work contributes to our understanding of lens biology, raising a new set of questions that will be important for the lens field in coming years.

#### *Imaging AQP0 in Human Lens*

Previous work in our lab has contributed to our understanding of age-related modifications to AQP0. Using MALDI MS in profiling and imaging modes, the localization of various forms of truncated, phosphorylated, and lipid-modified AQP0 were mapped to better understand programmed and age-related PTMs.<sup>1-4</sup> I combined endogenous protein imaging and tryptic peptide imaging of a wide age range of human lenses to better characterize AQP0 processing over time. The use of several ages of human lens better represents the time course of aging and helped clarify several unanswered questions in the lens field. A summary of major findings are listed here.

### **Fatty Acid Acylated AQP0**

MALDI IMS of 2-month- and 4-month-old human lenses revealed fatty acid acylation is present in the nucleus of very young lens. Although palmitic acid (C16:0, +238 Da) and oleic acid (C18:1, +264 Da) modifications were previously detected in rabbit, bovine, and 11 year human lens,<sup>3, 4</sup> these AQP0 modifications were not observed in fetal lens.<sup>5</sup> Our results are the first to show full-length AQP0 is fatty acid acylated in a very young lens core, suggesting programmed acylation in young fiber cells. Furthermore, these results confirm the presence of truncated, lipid-modified AQP0 that was observed in 29-year human lens<sup>3</sup> and reveal similar truncation patterns between unmodified and fatty acid acylated AQP0. Our time course experiments provide a complete picture AQP0 lipid modification, an irreversible acylation event in young fiber cells that remains attached to the protein throughout age-related C-terminal truncation events.

### **Deamidated AQP0 C-terminus**

I implemented *in situ* digestion to image the large, heavily-modified C-terminal fragment of AQP0. To our knowledge, these are the first MALDI images of deamidated peptides acquired directly from tissue sections. MALDI IMS of deamidated AQP0 tryptic peptides shows the time course of deamidation in human lens. Imaging at 100-125µm spatial resolution was critical for visualizing concentric rings of un-, singly-, and doubly-deamidated AQP0 in progressively older fiber cells. Deamidated full-length AQP0 is abundant in lenses as young as 2 months. LC-MS/MS studies also revealed N246 deamidation precedes N259 deamidation and showed that most truncation at residue 259 occurs during or after deamidation. Truncation at succinimide-prone residues suggests these residues serve as a way to direct cleavage in the long-lived lens.

## **Improved Sample Preparation Techniques and Analytical Methods for Imaging Protein PTMs**

This is the first application of *in situ* digestion and tryptic peptide imaging in lens. Imaging tryptic peptides can be advantageous for analyzing larger or less abundant proteins and small modifications. Although our focus was to characterize modified forms of AQP0, these experiments generated a rich dataset with information on numerous insoluble proteins in lens. Additional data analysis is expected to yield interesting information on insoluble crystallins, cytoskeletal proteins, and less-abundant membrane proteins. Future work will include cataract lens imaging to investigate insoluble proteins and posttranslational modifications associated with disease. The methods can also be adapted by performing more stringent washes to study how certain proteins become more insoluble over time. This work also highlights the power of high mass resolution FTICR instruments for imaging age-related changes in biological tissues.

### *Spatially-directed Proteomics of the Human Lens Outer Cortex and Remodeling Zone*

Confocal immunofluorescence microscopy and transmission electron microscopy (TEM) studies have characterized the morphological changes of the human lens plasma membrane at the remodeling zone.<sup>6, 7</sup> These studies revealed membrane remodeling and showed that ball-and-socket joints originate in the remodeling zone in human lens. However, follow-up studies to characterize the molecular changes in this region had not been conducted. Combining morphology-directed laser capture microdissection (LCM) with quantitative proteomics enabled us to isolate and characterize the remodeling zone and surrounding regions. Although protein changes were the focus of our studies, it remains possible that lipid changes in the plasma membrane are also important. Several interesting results came out of these experiments:

### **Switch from Intermediate Filaments to Beaded Bilaments in the RZ**

Initial shotgun proteomics studies showed significant changes in vimentin, filensin, and phakinin between differentiating fiber cells (DF) and the remodeling zone (RZ) located 100 $\mu$ m beneath the lens capsule. Follow-up studies using internal standards and quantitative proteomics confirmed these results. In the purified, urea-insoluble plasma membrane fraction, vimentin signal decreased at the remodeling zone, where beaded filament proteins filensin and phakinin had a significant increase in signal. Although these studies cannot be used to conclude whether intermediate filaments are responsible for morphological changes in the remodeling zone, they do show a strong correlation between the IF switch and the RZ.

### **Changes in Intermediate Filament Interacting Proteins (IFAPs)**

Several other cytoskeletal proteins were investigated using targeted quantitative proteomics. The intensity patterns for BASP1 match that of beaded filaments, while periaxin and periplakin match the pattern of vimentin, showing a decreased intensity in the remodeling zone and beyond. These interacting partners may be changing their association with the membrane or actin-binding proteins to allow deformation of the plasma membrane that is observed in the remodeling zone. Follow-up studies are needed to further assess their contribution to the characteristic morphological patterns in the RZ.

### **Lipid Changes in Human Lens Outer Cortex Detected by High Resolution MALDI IMS**

Follow-up studies using MALDI IMS were used to investigate whether any lipid changes could be detected in the RZ. Advances to MALDI MS technology enabled high spatial resolution

imaging, due in part to a small laser footprint and improved instrumentation capable of small raster step size. Furthermore, matrix application via sublimation results in less delocalization and is therefore compatible with 15 $\mu$ m imaging. Images were gathered in positive and negative ion mode, revealing a variety of lipids with localization changes based on distance from the lens capsule. Several signals had an increase in signal several hundred microns from the lens capsule, suggesting there could be changes in lipid synthesis or incorporation in the plasma membrane near the remodeling zone. Although tentative identifications were assigned based on accurate mass, future work requires additional studies and identification strategies to determine which lipid signals are changing in these regions.

## Future Research

Although this work contributes to our understanding of lens protein modifications based on fiber cell age and differentiation, there are a number of questions that remain unanswered. Integrating spatial information garnered from proteomics experiments with functional studies will be critical for painting a picture of how protein modifications affect lens physiology over time. Here, I discuss some important unanswered questions in the lens field and explore potential experiments that could contribute to our understanding of the lens.

### *What is the Function of the N- or C-terminal Fatty Acid Acylation?*

Initial studies revealed fatty acid acylation on N-terminal Met-1 and C-terminal Lys-238 of AQP0.<sup>3</sup> Both sites were found to be modified by palmitic acid, oleic acid, and others (unpublished).<sup>3</sup> Plasma membrane fractionation and purification revealed acylated AQP0 purified with the detergent-resistant lipid raft fraction.<sup>3</sup> Follow-up studies using sucrose density

gradient centrifugation showed two populations of AQP0 that purify with lipid raft-like and non-lipid raft fractions.<sup>8</sup> Fatty acid acylated AQP0 was in the lipid raft fraction, although some unmodified AQP0 was also present, suggesting there may be multiple means of targeting AQP0 to specific plasma membrane domains.<sup>8</sup> Treatment of lipid raft fractions with cholesterol-depleting methyl- $\beta$ -cyclodextrin removes this association, indicating some cholesterol dependence.<sup>8</sup> These data provide confirmation that fatty acylation influences plasma membrane domain localization of AQP0. Future studies should aim to investigate how this modification actually affects membrane trafficking. Super resolution microscopy is a promising tool for investigating protein localization within different components of the plasma membrane.

Furthermore, imaging studies at the protein level cannot distinguish between palmitic acid- (+238 Da) and oleic acid- (+264 Da) modified AQP0 because of the wide isotopic envelope of the large 28kDa protein. These peptides were not detected in our *in situ* digestion and peptide imaging experiments, presumably due to their extreme hydrophobicity. Improved instrumentation, like FTICR, could be useful for determining whether there is differential localization of oleoylated or palmytated AQP0. Follow-up studies should also address whether the N- or C-terminal lipid modification occur in the same regions of lens.

The functional consequences of lipid raft localization remain to be determined. Fatty acid acylation could be an important tool for modulating permeability, as plasma membrane composition has been shown to alter water permeability for both AQP0 and AQP4.<sup>9, 10</sup> The presence of a lipid could also alter protein-protein interactions by bringing proteins in close proximity. The lipid itself could block known protein interactions, as it is within the calmodulin-binding region of the AQP0 C-terminus.<sup>11</sup> It is unknown whether palmitic acid and oleic acid have the same effects on AQP0 function, or whether there are functional differences between N-

terminal and C-terminal fatty acid acylation. It will also be important to determine what enzymes, if any, are responsible for this modification.

*What is the Function of AQP0 C-terminal Cleavage?*

Truncation of AQP0 is a well-known AQP0 modification and has been demonstrated in numerous species.<sup>1, 4, 5, 12, 13</sup> In mouse and rat lens, truncation is observed at residues L234 and K238 early on, within the first few weeks of life. The abundance of calpain and demonstrated calpain enzymatic activity in rodent lens point to an enzymatic mechanism for cleavage at these sites.<sup>14, 15</sup> In human and bovine lens, cleavage has been demonstrated on a number of sites.<sup>5</sup> Unlike rodent lens, the major human truncation sites are at asparagine and aspartic acid residues.<sup>5</sup> Based on our imaging results showing deamidation of asparagine residues and the known phenomenon of cleavage at labile residues prone to succinimide formation, it is likely that human lens AQP0 truncation proceeds nonenzymatically.<sup>5, 16</sup> The presence of truncated AQP0 across a variety of species, and likely through different mechanisms, raises the possibility that AQP0 truncation plays an important role in modulating its function over time.

Initially, it was assumed that truncation was required to shift AQP0 from a water pore to a junctional or adhesion molecule.<sup>17, 18</sup> Follow-up studies indicate that permeability of the molecule does not change with C-terminal truncation<sup>19, 20</sup> and showed the full-length AQP0 molecule had similar adhesive properties.<sup>20, 21</sup> Other possible functions of C-terminal truncation could be to remove protein-protein interaction sites, or to potentially alter the C-terminal structure to make room for additional protein-protein interactions. It is possible that once fiber cell architecture is established, AQP0 interaction with beaded filament proteins filensin and phakinin, or ERM cytoskeletal proteins, is no longer required.<sup>22, 23</sup> Truncation of the C-terminus

may also expose the plasma membrane, enabling better access and binding of crystallin proteins. This could affect the lens refractive index in certain regions of the lens and could contribute to the barrier to diffusion observed in middle age.

Additional studies are required to elucidate the consequences of truncation on lens physiology. Immunofluorescence studies could reveal the localization of different protein-protein interactions and how they change based on fiber cell age. Innovative functional studies, including cell adhesion and permeability assays, are also expected to answer important questions about how cleavage can modulate AQP0 function.

#### *What Happens to the C-terminal Tail Upon Cleavage?*

AQP0 C-terminal truncation is a widespread phenomenon observed across many species. In human, major truncation sites at D243, N246, and N259 are observed. These cleavage events likely proceed through nonenzymatic truncation events. The fate of the cleaved C-terminal AQP0 peptide fragments remains to be determined. As fiber cells have little enzymatic activity, the fragments are not expected to undergo typical degradation or recycling.

Other proteins in the lens undergo cleavage, generating peptide fragments that traffic to the plasma membrane. Filensin truncation occurs at residues L39 and D431.<sup>24</sup> Upon cleavage, the new N-termini of the fragments can be modified by acetylation (A40) or myristoylation (G432).<sup>24</sup> Immunohistochemical studies showed the C-terminal fragment of filensin changes localization from cytoplasmic in younger fiber cells to membrane-associated in mature fiber cells.<sup>25</sup> Analysis of the urea-insoluble (or plasma membrane fraction) of both human and bovine lens showed the myristoylated C-terminal fragment of filensin, indicating the myristylation may target the newly-generated peptide to the plasma membrane. The N-terminus of AQP0 can be

acylated and fatty acid acylated (with oleic or palmitic acid) as well as truncated. Although N- and C-terminal fragments of AQP0 have not been detected in lens or shown to be myristoylated, it remains to be seen whether these are similarly modified or trafficked like filensin.

### *What is the Function of AQP5?*

Although AQP0, the most abundant membrane protein and water channel in the lens, was the focus of our studies, a second water channel, AQP5, was recently discovered in the lens. Characterizing the function, PTMs, and localization of both water channels is critical for our understanding of lens development and aging. Present at roughly 5% of AQP0 abundance, AQP5 was initially reported in lens via RT-PCR and immunohistochemistry<sup>26</sup> and has also been confirmed by Western blotting and mass spectrometry.<sup>27</sup> The function of AQP5 has not been elucidated, although confocal immunofluorescence microscopy studies provide some clues that suggest altered function based on lens region.<sup>12</sup> AQP5 is present in both epithelial and lens fiber cells.<sup>12, 26, 27</sup> In the outer cortex, AQP5 is localized to the cytoplasm, presumably in vesicles.<sup>12, 27</sup> Around the time of AQP0 cleavage, AQP5 moves to the plasma membrane.<sup>12</sup> PKA phosphorylation of AQP5 in a cell line induced internalization, indicating that phosphorylation plays a role in AQP5 trafficking.<sup>26</sup> Based on early expression during embryonic development and delayed insertion in the membrane,<sup>12</sup> it has been hypothesized that AQP5 serves as a back-up water channel in lens. However, since recent studies have shown AQP0 remains permeable after C-terminal cleavage, it may not be necessary to have a “rescue” channel. Knockout of AQP5 in mice resulted in greater susceptibility to hypoglycemic cataract.<sup>28</sup> Analysis of AQP5 is challenging, given its low abundance and that it has the same molecular weight as AQP0. Advances in sample preparation and mass spectrometry technology will facilitate analysis of

AQP5. Current efforts should focus on analyzing AQP5 post-translational modifications, since modifications like fatty acid acylation and phosphorylation are known to affect trafficking of other membrane proteins. Understanding the role of AQP5 in lens will shed light on the role of water channels for lens physiology.

#### *Where are Phosphorylated Forms of AQP0 Localized?*

I used *in situ* digestion to map site-specific and small PTMs of AQP0. These imaging studies revealed new information about the time course of AQP0 deamidation and truncation in human lens. Another important AQP0 PTM is phosphorylation, which has been detected on 13 residues of AQP0. The most abundant phosphorylation site, S-235, is important for AQP0 trafficking in cells and regulation of AQP0 permeability by reducing affinity for calmodulin.<sup>11</sup> The localization of some phosphorylated AQP0 forms has been elucidated by laser capture microdissection followed by LC-MS/MS analysis.<sup>29</sup> MALDI profiling data has also shown intact AQP0 with an addition of phosphorylation in rabbit and bovine lens, although this does not provide any information on the phosphorylation site.<sup>4</sup> A complete picture of the localization and timing of AQP0 phosphorylation at various sites has not been elucidated. In our *in situ* digestion imaging data, we looked for *m/z* signals of the expected AQP0 phosphorylated peptides with no success. This is not entirely unexpected, given that phosphorylated peptides are known to have lower ionizability and are typically present at lower stoichiometry compared to their unmodified counterparts. Furthermore, because AQP0 contains a number of phosphorylation sites, it is possible that low levels of phosphorylation at each site makes the individual peptides difficult to detect, even though a phosphorylated form can be detected at the intact protein level. Optimized sample preparation to enrich for phosphorylated peptides should be helpful for enhancing signal

to detect and map phospho-AQP0 peptides. Preliminary work from our lab showed promising results for enriching a phosphorylated  $\alpha$ -crystallin peptide from bovine lens using a titanium dioxide-coated slide and a stringent washing protocol (data not shown). Identification techniques, like microextraction and tissue hydrogels, will be critical for identifying specific sites of AQP0 phosphorylation detected in imaging experiments.

*What is the Function of the Primate Lens Remodeling Zone?*

Our remodeling zone study investigated the protein changes between the remodeling zone and surrounding tissue regions. TEM studies have also shown ball-and-socket joints originate in the remodeling zone, and cellular compaction begins to occur just beyond this region.<sup>7</sup> However, the function of the remodeling zone remains to be determined. Follow-up studies using confocal immunofluorescence microscopy will provide additional insight into protein changes quantified in the RZ using proteomics. Additional lipid characterization studies using MALDI IMS will be helpful for understanding whether the plasma membrane composition changes significantly in the remodeling zone.

The extreme morphological changes have only been detected in human and macaque monkey lens. Therefore, using a knockout model to study the remodeling zone is not feasible. Because filensin and phakinin increase dramatically in the remodeling zone, it would be interesting to search large biobanks for individuals with mutations in these proteins in order to determine whether they have any signs of lens abnormality, like opacity, increased light scattering, or accommodation issues.

## Perspectives

Our experiments used a combination of spatially-resolved proteomics methods to map modified AQP0 in aging human lenses and revealed cytoskeletal protein changes associated with the human lens remodeling zone. Moving forward, these results will advance the lens field in several ways. First, mapping deamidated AQP0 in human lens highlights the fact that deamidation occurs in very young fiber cells and precedes age-related truncation events that have been well characterized in human lens. These results support a mechanism of non-enzymatic truncation in human lens, whereas calpain-mediated cleavage dominates in mouse and rat lens. The fact that two distinct mechanisms for AQP0 cleavage exist across multiple species suggests that truncation is likely important for modulating AQP0 function over time. Additionally, the presence of fatty acid acylated AQP0 in very young lens indicates this modification is important during lens development. Future research should aim to understand how AQP0 truncation and fatty acid acylation affect permeability, protein-protein interactions, or expose the plasma membrane to binding by other proteins with age (potentially contributing to presbyopia or the lens permeability barrier at age 50). This information will aid our understanding of how AQP0 functions in different regions of the lens.

Furthermore, our proteomics results only begin to scratch the surface of the biochemical and functional mechanisms of the human lens remodeling zone. The switch from intermediate filaments to beaded filaments at the remodeling zone suggests an important role for lens-specific intermediate filaments. With this knowledge, we can design more tailored studies to determine the mechanisms responsible for membrane remodeling. Future studies should examine human lens sections using confocal immunofluorescence microscopy to visualize actin polymerization and protein subcellular localization changes in this unique region. Examining lenses of other

accommodating species (i.e. birds or fish) and primates will help determine the function of the remodeling zone.

Lastly, our sample preparation techniques and use of cutting-edge technology pave the way for studying other facets of lens aging and development. *In situ* digestion and MALDI peptide imaging at ultrahigh mass resolution can reveal where deamidated crystallins, which have been associated with cataract, are localized. This method will also be helpful for mapping the localization of other large and insoluble lens proteins that become modified over time. Ultimately, our results revealed protein changes related to normal lens development and aging, contributed to our understanding of lens physiology, and set the stage for studying protein modifications that contribute to cataract.

## References

1. Grey AC, Chaurand P, Caprioli RM, Schey KL. MALDI imaging mass spectrometry of integral membrane proteins from ocular lens and retinal tissue. *J Proteome Res* 2009;8:3278-3283.
2. Gutierrez DB, Garland D, Schey KL. Spatial analysis of human lens aquaporin-0 post-translational modifications by MALDI mass spectrometry tissue profiling. *Exp Eye Res* 2011;93:912-920.
3. Schey KL, Gutierrez DB, Wang Z, Wei J, Grey AC. Novel Fatty Acid Acylation of Lens Integral Membrane Protein Aquaporin-0. *Biochemistry* 2010;49:9858-9865.
4. Thibault DB, Gillam CJ, Grey AC, Han J, Schey KL. MALDI tissue profiling of integral membrane proteins from ocular tissues. *J Am Soc Mass Spectrom* 2008;19:814-822.
5. Korlimbinis A, Berry Y, Thibault D, Schey KL, Truscott RJ. Protein aging: truncation of aquaporin 0 in human lens regions is a continuous age-dependent process. *Exp Eye Res* 2009;88:966-973.
6. Lim JC, K.L. W, T. S, Schey KL, Donaldson PJ. Confocal microscopy reveals zones of membrane remodeling in the outer cortex of the human lens. *Invest Ophthalmol Vis Sci* 2009;50:4304-4310.
7. Costello MJ, A. M, Gilliland KO, Fowler WC, Johnsen S. Ultrastructural analysis of the human lens fiber cell remodeling zone and the initiation of cellular compaction. *Exp Eye Res* 2013;116:411-418.
8. Wang Z, Schey KL. Proteomic Analysis of Lipid Raft-like Detergent-Resistant Membranes of Lens Fiber Cells. *Invest Ophthalmol Vis Sci* 2015 (In press).
9. Tong J, Briggs Margaret M, McIntosh Thomas J. Water Permeability of Aquaporin-4 Channel Depends on Bilayer Composition, Thickness, and Elasticity. *Biophysical Journal* 2012;103:1899-1908.
10. Tong J, Cantly JT, Briggs MM, McIntosh TJ. The water permeability of lens aquaporin-0 depends on its lipid bilayer environment. *Experimental Eye Research* 2013;113:32-40.
11. Rose KM, Wang Z, Magrath GN, Hazard ES, Hildebrandt JD, Schey KL. Aquaporin 0-calmodulin interaction and the effect of aquaporin 0 phosphorylation. *Biochemistry* 2008;47:339-347.
12. Petrova RS, Schey KL, Donaldson PJ, Grey AC. Spatial distributions of AQP5 and AQP0 in embryonic and postnatal mouse lens development. *Exp Eye Res* 2015;132:124-135.

13. Ball LE, Garland DL, Crouch RK, Schey KL. Post-translational modifications of aquaporin 0 (AQP0) in the normal human lens: spatial and temporal occurrence. *Biochemistry* 2004;43:9856-9865.
14. David LL, Shearer TR. Purification of calpain II from rat lens and determination of endogenous substrates. *Exp Eye Res* 1986;42:227-238.
15. Ma H, Shih M, Hata I, Fukiage C, Azuma M, Shearer TR. Lp85 calpain is an enzymatically active rodent-specific isozyme of lens Lp82. *Curr Eye Res* 2000;20:183-189.
16. Robinson NE, Robinson AB. *Molecular Clocks*. Cave Junction, OR: Althouse Press; 2004.
17. Gonen T, Cheng Y, Kistler J, Walz T. Aquaporin-0 membrane junctions form upon proteolytic cleavage. *J Mol Biol* 2004;342:1337-1345.
18. Gonen T, Cheng Y, Sliz P, et al. Lipid-protein interactions in double-layered two-dimensional AQP0 crystals. *Nature* 2005;438:633-638.
19. Ball LE, Little M, Nowak MW, Garland DL, Crouch RK, Schey KL. Water Permeability of C-Terminally Truncated Aquaporin 0 (AQP0 1-243) Observed in the Aging Human Lens. *Invest Ophthalmol Vis Sci* 2003;44:4820-4828.
20. Kumari SS, Varadaraj K. Intact and N- or C-terminal end truncated AQP0 function as open water channels and cell-to-cell adhesion proteins: end truncation could be a prelude for adjusting the refractive index of the lens to prevent spherical aberration. *Biochim Biophys Acta* 2014;1840:2862-2877.
21. Kumari SS, Varadaraj K. Intact AQP0 performs cell-to-cell adhesion. *Biochem Biophys Res Commun* 2009;390:1034-1039.
22. Lindsey Rose KM, Gourdie RG, Prescott AR, Quinlan RA, Crouch RK, Schey KL. The C terminus of lens aquaporin 0 interacts with the cytoskeletal proteins filensin and CP49. *Invest Ophthalmol Vis Sci* 2006;47:1562-1570.
23. Wang Z, Schey KL. Aquaporin-0 interacts with the FERM domain of ERM proteins in the ocular lens. *Invest Ophthalmol Vis Sci* 2011;52:5079-5087.
24. Wang Z, Obidike JE, Schey KL. Posttranslational modifications of the bovine lens beaded filament proteins filensin and CP49. *Invest Ophthalmol Vis Sci* 2010;51:1565-1574.
25. Sandilands A, Prescott AR, Hutcheson AM, Quinlan RA, Casselman JT, FitzGerald PG. Filensin is proteolytically processed during lens fiber cell differentiation by multiple independent pathways. *Eur J Cell Biol* 1995;67:238-253.

26. Kumari SS, Varadaraj M, Yerramilli VS, Menon AG, Varadaraj K. Spatial expression of aquaporin 5 in mammalian cornea and lens, and regulation of its localization by phosphokinase A. *Mol Vis* 2012;18:957-967.
27. Grey AC, Walker KL, Petrova RS, et al. Verification and spatial localization of aquaporin-5 in the ocular lens. *Exp Eye Res* 2013;108:94-102.
28. Kumari SS, Varadaraj K. Aquaporin 5 knockout mouse lens develops hyperglycemic cataract. *Biochem Biophys Res Commun* 2013;441:333-338.
29. Wang Z, Han J, Schey KL. Spatial differences in an integral membrane proteome detected in laser capture microdissected samples. *J Proteome Res* 2008;7:2696-2702.

## Appendix A – ANOVA and Tukey test results for each peptide monitored by MRM

A total of 6 measurements were used to calculate the mean for each region. Mean values and significance were calculated based on ratios, where the region (DF, RZ, TZ, or IC) with the most intense signal is set to 1 and other regions are taken as a fraction of 1.

**A.) VIMENTIN<sub>51</sub>SLYASSPGGVYATR<sup>\*</sup><sub>64</sub>**

**Descriptives**

Ratio

	N	Mean	Std. Deviation	Std. Error	95% Confidence Interval for Mean		Minimum	Maximum
					Lower Bound	Upper Bound		
DF	6	1.0000	.00000	.00000	1.0000	1.0000	1.00	1.00
RZ	6	.1961	.04685	.01913	.1469	.2452	.14	.27
TZ	6	.0311	.01511	.00617	.0153	.0470	.01	.05
IC	6	.0237	.01773	.00724	.0051	.0423	.01	.05
Total	24	.3127	.41213	.08413	.1387	.4867	.01	1.00

**ANOVA**

Ratio

	Sum of Squares	df	Mean Square	F	Sig.
Between Groups	3.893	3	1.298	1895.591	.000
Within Groups	.014	20	.001		
Total	3.907	23			

**Multiple Comparisons**

Dependent Variable: Ratio

Tukey HSD

(I) Region	(J) Region	Mean Difference (I-J)	Std. Error	Sig.	95% Confidence Interval	
					Lower Bound	Upper Bound
DF	RZ	.80394*	.01511	.000	.7617	.8462
	TZ	.96888*	.01511	.000	.9266	1.0112
	IC	.97632*	.01511	.000	.9340	1.0186
RZ	DF	-.80394*	.01511	.000	-.8462	-.7617
	TZ	.16494*	.01511	.000	.1227	.2072
	IC	.17239*	.01511	.000	.1301	.2147
TZ	DF	-.96888*	.01511	.000	-1.0112	-.9266
	RZ	-.16494*	.01511	.000	-.2072	-.1227
	IC	.00745	.01511	.960	-.0348	.0497
IC	DF	-.97632*	.01511	.000	-1.0186	-.9340
	RZ	-.17239*	.01511	.000	-.2147	-.1301
	TZ	-.00745	.01511	.960	-.0497	.0348

\*. The mean difference is significant at the 0.05 level.

**B.) VIMENTIN** 295FADLSEAANR\*<sub>304</sub>

**Descriptives**

Ratio

	N	Mean	Std. Deviation	Std. Error	95% Confidence Interval for Mean		Minimum	Maximum
					Lower Bound	Upper Bound		
DF	6	1.0000	.00000	.00000	1.0000	1.0000	1.00	1.00
RZ	6	.1644	.07275	.02970	.0881	.2408	.07	.22
TZ	6	.0228	.00861	.00351	.0137	.0318	.01	.03
IC	6	.0030	.00278	.00113	.0001	.0059	.00	.01
Total	24	.2976	.42052	.08584	.1200	.4751	.00	1.00

**ANOVA**

Ratio

	Sum of Squares	df	Mean Square	F	Sig.
Between Groups	4.040	3	1.347	1002.501	.000
Within Groups	.027	20	.001		
Total	4.067	23			

**Multiple Comparisons**

Dependent Variable: Ratio

Tukey HSD

(I) Region	(J) Region	Mean Difference (I-J)	Std. Error	Sig.	95% Confidence Interval	
					Lower Bound	Upper Bound
DF	RZ	.83555*	.02116	.000	.7763	.8948
	TZ	.97723*	.02116	.000	.9180	1.0365
	IC	.99698*	.02116	.000	.9377	1.0562
RZ	DF	-.83555*	.02116	.000	-.8948	-.7763
	TZ	.14167*	.02116	.000	.0824	.2009
	IC	.16142*	.02116	.000	.1022	.2207
TZ	DF	-.97723*	.02116	.000	-1.0365	-.9180
	RZ	-.14167*	.02116	.000	-.2009	-.0824
	IC	.01975	.02116	.788	-.0395	.0790
IC	DF	-.99698*	.02116	.000	-1.0562	-.9377
	RZ	-.16142*	.02116	.000	-.2207	-.1022
	TZ	-.01975	.02116	.788	-.0790	.0395

\*. The mean difference is significant at the 0.05 level.

**C.) PERIAXIN 56SLSLQEGDQLLSAR\*<sub>69</sub>**

**Descriptives**

Ratio

	N	Mean	Std. Deviation	Std. Error	95% Confidence Interval for Mean		Minimum	Maximum
					Lower Bound	Upper Bound		
DF	6	1.0000	.00000	.00000	1.0000	1.0000	1.00	1.00
RZ	6	.6227	.14486	.05914	.4707	.7747	.48	.85
TZ	6	.2199	.14846	.06061	.0641	.3757	.04	.45
IC	6	.1973	.11477	.04686	.0768	.3177	.08	.34
Total	24	.5100	.35443	.07235	.3603	.6596	.04	1.00

**ANOVA**

Ratio

	Sum of Squares	df	Mean Square	F	Sig.
Between Groups	2.608	3	.869	61.886	.000
Within Groups	.281	20	.014		
Total	2.889	23			

**Multiple Comparisons**

Dependent Variable: Ratio

Tukey HSD

(I) Region	(J) Region	Mean Difference (I-J)	Std. Error	Sig.	95% Confidence Interval	
					Lower Bound	Upper Bound
DF	RZ	.37731*	.06843	.000	.1858	.5689
	TZ	.78007*	.06843	.000	.5885	.9716
	IC	.80271*	.06843	.000	.6112	.9942
RZ	DF	-.37731*	.06843	.000	-.5689	-.1858
	TZ	.40275*	.06843	.000	.2112	.5943
	IC	.42539*	.06843	.000	.2339	.6169
TZ	DF	-.78007*	.06843	.000	-.9716	-.5885
	RZ	-.40275*	.06843	.000	-.5943	-.2112
	IC	.02264	.06843	.987	-.1689	.2142
IC	DF	-.80271*	.06843	.000	-.9942	-.6112
	RZ	-.42539*	.06843	.000	-.6169	-.2339
	TZ	-.02264	.06843	.987	-.2142	.1689

\*. The mean difference is significant at the 0.05 level.

**D.) PERIPLAKIN**  $^{1427}\text{LAALEQEEAEAR}^*$   $^{1438}$

**Descriptives**

Ratio

	N	Mean	Std. Deviation	Std. Error	95% Confidence Interval for Mean		Minimum	Maximum
					Lower Bound	Upper Bound		
DF	6	1.0000	.00000	.00000	1.0000	1.0000	1.00	1.00
RZ	6	.6968	.19036	.07771	.4970	.8966	.47	.89
TZ	6	.1700	.05774	.02357	.1094	.2306	.08	.24
IC	6	.0851	.04746	.01938	.0353	.1349	.01	.14
Total	24	.4880	.39697	.08103	.3203	.6556	.01	1.00

**ANOVA**

Ratio

	Sum of Squares	df	Mean Square	F	Sig.
Between Groups	3.415	3	1.138	108.883	.000
Within Groups	.209	20	.010		
Total	3.624	23			

**Multiple Comparisons**

Dependent Variable: Ratio

Tukey HSD

(I) Region	(J) Region	Mean Difference (I-J)	Std. Error	Sig.	95% Confidence Interval	
					Lower Bound	Upper Bound
DF	RZ	.30320*	.05904	.000	.1380	.4684
	TZ	.82999*	.05904	.000	.6648	.9952
	IC	.91494*	.05904	.000	.7497	1.0802
RZ	DF	-.30320*	.05904	.000	-.4684	-.1380
	TZ	.52679*	.05904	.000	.3616	.6920
	IC	.61173*	.05904	.000	.4465	.7770
TZ	DF	-.82999*	.05904	.000	-.9952	-.6648
	RZ	-.52679*	.05904	.000	-.6920	-.3616
	IC	.08494	.05904	.491	-.0803	.2502
IC	DF	-.91494*	.05904	.000	-1.0802	-.7497
	RZ	-.61173*	.05904	.000	-.7770	-.4465
	TZ	-.08494	.05904	.491	-.2502	.0803

\*. The mean difference is significant at the 0.05 level.

**E.) PERIPLAKIN**  $^{1447}_{1447}$ VVLQQDPQQAR\* $^{1457}_{1457}$

**Descriptives**

Ratio

	N	Mean	Std. Deviation	Std. Error	95% Confidence Interval for Mean		Minimum	Maximum
					Lower Bound	Upper Bound		
DF	6	1.0000	.00000	.00000	1.0000	1.0000	1.00	1.00
RZ	6	.7197	.15449	.06307	.5575	.8818	.58	.97
TZ	6	.1489	.07554	.03084	.0696	.2282	.01	.22
IC	6	.0849	.05256	.02146	.0297	.1401	.02	.16
Total	24	.4884	.40224	.08211	.3185	.6582	.01	1.00

**ANOVA**

Ratio

	Sum of Squares	df	Mean Square	F	Sig.
Between Groups	3.560	3	1.187	146.781	.000
Within Groups	.162	20	.008		
Total	3.721	23			

**Multiple Comparisons**

Dependent Variable: Ratio

Tukey HSD

(I) Region	(J) Region	Mean Difference (I-J)	Std. Error	Sig.	95% Confidence Interval	
					Lower Bound	Upper Bound
DF	RZ	.28035*	.05191	.000	.1351	.4256
	TZ	.85109*	.05191	.000	.7058	.9964
	IC	.91510*	.05191	.000	.7698	1.0604
RZ	DF	-.28035*	.05191	.000	-.4256	-.1351
	TZ	.57074*	.05191	.000	.4254	.7160
	IC	.63475*	.05191	.000	.4895	.7800
TZ	DF	-.85109*	.05191	.000	-.9964	-.7058
	RZ	-.57074*	.05191	.000	-.7160	-.4254
	IC	.06401	.05191	.614	-.0813	.2093
IC	DF	-.91510*	.05191	.000	-1.0604	-.7698
	RZ	-.63475*	.05191	.000	-.7800	-.4895
	TZ	-.06401	.05191	.614	-.2093	.0813

\*. The mean difference is significant at the 0.05 level.

F.) **BASP1** <sub>39</sub>ESEPQAAAEPAEAK\*<sub>52</sub>

**Descriptives**

Ratio

	N	Mean	Std. Deviation	Std. Error	95% Confidence Interval for Mean		Minimum	Maximum
					Lower Bound	Upper Bound		
DF	6	.4344	.16029	.06544	.2661	.6026	.18	.65
RZ	6	1.0000	.00000	.00000	1.0000	1.0000	1.00	1.00
TZ	6	.7459	.17705	.07228	.5601	.9317	.56	1.05
IC	6	.6960	.22612	.09231	.4587	.9333	.48	1.06
Total	24	.7191	.25608	.05227	.6109	.8272	.18	1.06

**ANOVA**

Ratio

	Sum of Squares	df	Mean Square	F	Sig.
Between Groups	.967	3	.322	11.924	.000
Within Groups	.541	20	.027		
Total	1.508	23			

**Multiple Comparisons**

Dependent Variable: Ratio

Tukey HSD

(I) Region	(J) Region	Mean Difference (I-J)	Std. Error	Sig.	95% Confidence Interval	
					Lower Bound	Upper Bound
DF	RZ	-.56563*	.09494	.000	-.8314	-.2999
	TZ	-.31154*	.09494	.018	-.5773	-.0458
	IC	-.26160	.09494	.055	-.5273	.0041
RZ	DF	.56563*	.09494	.000	.2999	.8314
	TZ	.25409	.09494	.064	-.0116	.5198
	IC	.30403*	.09494	.021	.0383	.5698
TZ	DF	.31154*	.09494	.018	.0458	.5773
	RZ	-.25409	.09494	.064	-.5198	.0116
	IC	.04994	.09494	.952	-.2158	.3157
IC	DF	.26160	.09494	.055	-.0041	.5273
	RZ	-.30403*	.09494	.021	-.5698	-.0383
	TZ	-.04994	.09494	.952	-.3157	.2158

\*. The mean difference is significant at the 0.05 level.

**G.) BASP1**  $^{103}\text{APEQEQAAAPGPAAGGEAPK}^*$   $^{121}$

**Descriptives**

Ratio

	N	Mean	Std. Deviation	Std. Error	95% Confidence Interval for Mean		Minimum	Maximum
					Lower Bound	Upper Bound		
DF	6	.3834	.17567	.07172	.1991	.5678	.20	.70
RZ	6	1.0000	.00000	.00000	1.0000	1.0000	1.00	1.00
TZ	6	.5984	.21376	.08727	.3740	.8227	.42	.99
IC	6	.6028	.24186	.09874	.3490	.8566	.30	.96
Total	24	.6462	.28481	.05814	.5259	.7664	.20	1.00

**ANOVA**

Ratio

	Sum of Squares	df	Mean Square	F	Sig.
Between Groups	1.190	3	.397	11.753	.000
Within Groups	.675	20	.034		
Total	1.866	23			

**Multiple Comparisons**

Dependent Variable: Ratio

Tukey HSD

(I) Region	(J) Region	Mean Difference (I-J)	Std. Error	Sig.	95% Confidence Interval	
					Lower Bound	Upper Bound
DF	RZ	-.61659*	.10609	.000	-.9135	-.3197
	TZ	-.21496	.10609	.212	-.5119	.0820
	IC	-.21941	.10609	.197	-.5163	.0775
RZ	DF	.61659*	.10609	.000	.3197	.9135
	TZ	.40163*	.10609	.006	.1047	.6986
	IC	.39718*	.10609	.006	.1002	.6941
TZ	DF	.21496	.10609	.212	-.0820	.5119
	RZ	-.40163*	.10609	.006	-.6986	-.1047
	IC	-.00445	.10609	1.000	-.3014	.2925
IC	DF	.21941	.10609	.197	-.0775	.5163
	RZ	-.39718*	.10609	.006	-.6941	-.1002
	TZ	.00445	.10609	1.000	-.2925	.3014

\*. The mean difference is significant at the 0.05 level.

## H.) BASP1<sub>185</sub>ETPAATEAPSSTPK\*<sub>198</sub>

### Descriptives

Ratio

	N	Mean	Std. Deviation	Std. Error	95% Confidence Interval for Mean		Minimum	Maximum
					Lower Bound	Upper Bound		
DF	6	.5448	.17005	.06942	.3664	.7233	.32	.75
RZ	6	1.0000	.00000	.00000	1.0000	1.0000	1.00	1.00
TZ	6	.5323	.10797	.04408	.4190	.6456	.40	.69
IC	6	.2759	.04218	.01722	.2316	.3202	.20	.32
Total	24	.5883	.28319	.05780	.4687	.7078	.20	1.00

### ANOVA

Ratio

	Sum of Squares	df	Mean Square	F	Sig.
Between Groups	1.633	3	.544	51.398	.000
Within Groups	.212	20	.011		
Total	1.844	23			

### Multiple Comparisons

Dependent Variable: Ratio

Tukey HSD

(I) Region	(J) Region	Mean Difference (I-J)	Std. Error	Sig.	95% Confidence Interval	
					Lower Bound	Upper Bound
DF	RZ	-.45516*	.05941	.000	-.6214	-.2889
	TZ	.01254	.05941	.997	-.1537	.1788
	IC	.26893*	.05941	.001	.1026	.4352
RZ	DF	.45516*	.05941	.000	.2889	.6214
	TZ	.46771*	.05941	.000	.3014	.6340
	IC	.72410*	.05941	.000	.5578	.8904
TZ	DF	-.01254	.05941	.997	-.1788	.1537
	RZ	-.46771*	.05941	.000	-.6340	-.3014
	IC	.25639*	.05941	.002	.0901	.4227
IC	DF	-.26893*	.05941	.001	-.4352	-.1026
	RZ	-.72410*	.05941	.000	-.8904	-.5578
	TZ	-.25639*	.05941	.002	-.4227	-.0901

\*. The mean difference is significant at the 0.05 level.

## I.) FILENSIN <sub>78</sub>LGEAGPEDALAR\*<sub>90</sub>

### Descriptives

Ratio

	N	Mean	Std. Deviation	Std. Error	95% Confidence Interval for Mean		Minimum	Maximum
					Lower Bound	Upper Bound		
DF	6	.4003	.10802	.04410	.2869	.5136	.29	.55
RZ	6	1.0000	.00000	.00000	1.0000	1.0000	1.00	1.00
TZ	6	.6906	.05776	.02358	.6300	.7512	.59	.75
IC	6	.8566	.21467	.08764	.6313	1.0818	.65	1.13
Total	24	.7369	.25533	.05212	.6290	.8447	.29	1.13

### ANOVA

Ratio

	Sum of Squares	df	Mean Square	F	Sig.
Between Groups	1.194	3	.398	26.061	.000
Within Groups	.305	20	.015		
Total	1.499	23			

### Multiple Comparisons

Dependent Variable: Ratio

Tukey HSD

(I) Region	(J) Region	Mean Difference (I-J)	Std. Error	Sig.	95% Confidence Interval	
					Lower Bound	Upper Bound
DF	RZ	-.59971*	.07135	.000	-.7994	-.4000
	TZ	-.29028*	.07135	.003	-.4900	-.0906
	IC	-.45629*	.07135	.000	-.6560	-.2566
RZ	DF	.59971*	.07135	.000	.4000	.7994
	TZ	.30943*	.07135	.002	.1097	.5091
	IC	.14343	.07135	.217	-.0563	.3431
TZ	DF	.29028*	.07135	.003	.0906	.4900
	RZ	-.30943*	.07135	.002	-.5091	-.1097
	IC	-.16600	.07135	.125	-.3657	.0337
IC	DF	.45629*	.07135	.000	.2566	.6560
	RZ	-.14343	.07135	.217	-.3431	.0563
	TZ	.16600	.07135	.125	-.0337	.3657

\*. The mean difference is significant at the 0.05 level.

**J.) FILENSIN** <sub>240</sub>VELQAQTTLEQAIK\*<sub>254</sub>

**Descriptives**

Ratio

	N	Mean	Std. Deviation	Std. Error	95% Confidence Interval for Mean		Minimum	Maximum
					Lower Bound	Upper Bound		
DF	6	.4300	.13354	.05452	.2899	.5702	.34	.70
RZ	6	1.0000	.00000	.00000	1.0000	1.0000	1.00	1.00
TZ	6	.4910	.23093	.09428	.2486	.7333	.25	.78
IC	6	.7924	.31795	.12980	.4587	1.1260	.45	1.22
Total	24	.6783	.30508	.06227	.5495	.8072	.25	1.22

**ANOVA**

Ratio

	Sum of Squares	df	Mean Square	F	Sig.
Between Groups	1.279	3	.426	9.903	.000
Within Groups	.861	20	.043		
Total	2.141	23			

**Multiple Comparisons**

Dependent Variable: Ratio

Tukey HSD

(I) Region	(J) Region	Mean Difference (I-J)	Std. Error	Sig.	95% Confidence Interval	
					Lower Bound	Upper Bound
DF	RZ	-.56997*	.11981	.001	-.9053	-.2346
	TZ	-.06093	.11981	.956	-.3963	.2744
	IC	-.36233*	.11981	.031	-.6977	-.0270
RZ	DF	.56997*	.11981	.001	.2346	.9053
	TZ	.50904*	.11981	.002	.1737	.8444
	IC	.20764	.11981	.334	-.1277	.5430
TZ	DF	.06093	.11981	.956	-.2744	.3963
	RZ	-.50904*	.11981	.002	-.8444	-.1737
	IC	-.30140	.11981	.088	-.6367	.0339
IC	DF	.36233*	.11981	.031	.0270	.6977
	RZ	-.20764	.11981	.334	-.5430	.1277
	TZ	.30140	.11981	.088	-.0339	.6367

\*. The mean difference is significant at the 0.05 level.

## K.) PHAKININ 201AAEEEINSLYK\*<sub>211</sub>

### Descriptives

Ratio

	N	Mean	Std. Deviation	Std. Error	95% Confidence Interval for Mean		Minimum	Maximum
					Lower Bound	Upper Bound		
DF	6	.4036	.07967	.03253	.3200	.4872	.28	.46
RZ	6	1.0000	.00000	.00000	1.0000	1.0000	1.00	1.00
TZ	6	.6328	.12330	.05034	.5034	.7622	.51	.80
IC	6	.8138	.20386	.08323	.5998	1.0277	.60	1.13
Total	24	.7125	.25398	.05184	.6053	.8198	.28	1.13

### ANOVA

Ratio

	Sum of Squares	df	Mean Square	F	Sig.
Between Groups	1.168	3	.389	24.679	.000
Within Groups	.316	20	.016		
Total	1.484	23			

### Multiple Comparisons

Dependent Variable: Ratio

Tukey HSD

(I) Region	(J) Region	Mean Difference (I-J)	Std. Error	Sig.	95% Confidence Interval	
					Lower Bound	Upper Bound
DF	RZ	-.59639*	.07252	.000	-.7994	-.3934
	TZ	-.22916*	.07252	.023	-.4321	-.0262
	IC	-.41016*	.07252	.000	-.6131	-.2072
RZ	DF	.59639*	.07252	.000	.3934	.7994
	TZ	.36723*	.07252	.000	.1643	.5702
	IC	.18623	.07252	.079	-.0167	.3892
TZ	DF	.22916*	.07252	.023	.0262	.4321
	RZ	-.36723*	.07252	.000	-.5702	-.1643
	IC	-.18100	.07252	.091	-.3840	.0220
IC	DF	.41016*	.07252	.000	.2072	.6131
	RZ	-.18623	.07252	.079	-.3892	.0167
	TZ	.18100	.07252	.091	-.0220	.3840

\*. The mean difference is significant at the 0.05 level.

## L.) PHAKININ 288 VEAGALLQAK\*<sub>297</sub>

### Descriptives

Ratio

	N	Mean	Std. Deviation	Std. Error	95% Confidence Interval for Mean		Minimum	Maximum
					Lower Bound	Upper Bound		
DF	6	.4978	.10119	.04131	.3916	.6040	.37	.62
RZ	6	1.0000	.00000	.00000	1.0000	1.0000	1.00	1.00
TZ	6	.7114	.24088	.09834	.4586	.9642	.53	1.06
IC	6	.7340	.21095	.08612	.5126	.9554	.45	.99
Total	24	.7358	.24011	.04901	.6344	.8372	.37	1.06

### ANOVA

Ratio

	Sum of Squares	df	Mean Square	F	Sig.
Between Groups	.762	3	.254	9.012	.001
Within Groups	.564	20	.028		
Total	1.326	23			

### Multiple Comparisons

Dependent Variable: Ratio

Tukey HSD

(I) Region	(J) Region	Mean Difference (I-J)	Std. Error	Sig.	95% Confidence Interval	
					Lower Bound	Upper Bound
DF	RZ	-.50216*	.09694	.000	-.7735	-.2308
	TZ	-.21357	.09694	.157	-.4849	.0577
	IC	-.23614	.09694	.102	-.5075	.0352
RZ	DF	.50216*	.09694	.000	.2308	.7735
	TZ	.28858*	.09694	.035	.0173	.5599
	IC	.26602	.09694	.056	-.0053	.5373
TZ	DF	.21357	.09694	.157	-.0577	.4849
	RZ	-.28858*	.09694	.035	-.5599	-.0173
	IC	-.02256	.09694	.995	-.2939	.2488
IC	DF	.23614	.09694	.102	-.0352	.5075
	RZ	-.26602	.09694	.056	-.5373	.0053
	TZ	.02256	.09694	.995	-.2488	.2939

\*. The mean difference is significant at the 0.05 level.